HIGH RESOLUTION 3D DIFFUSION TENSOR IMAGING FOR DELINEATING NEURONAL ARCHITECTURES

BY

ANH TU VAN

DISSERTATION

Submitted in partial fulfillment of the requirements
for the degree of Doctor of Philosophy in Electrical and Computer Engineering
in the Graduate College of the
University of Illinois at Urbana-Champaign, 2010

Urbana, Illinois

Doctoral Committee:

Assistant Professor Bradley P. Sutton, Chair
Professor Yoram Bresler
Professor Zhi-Pei Liang
Associate Professor Minh N. Do
Assistant Professor Brian D. Gonsalves

ABSTRACT

Diffusion tensor imaging (DTI) has long been an important tool for early diagnosis and monitoring of neuronal diseases as well as for understanding the connectivity of neuronal networks. However, the intrinsic problem of DTI is the partial volume effect, which worsens when the structure of interest is complex with fine neuronal tracts. Although many techniques have been proposed to improve the resolution of DTI and hence reduce the partial volume effect, high isotropic resolution DTI remains a challenge. The key difficulties are: (a) severe reduction of signal-to-noise ratio (SNR), (b) sensitivity to numerous artifacts such as motion-induced phase error and/or magnetic susceptibility, (c) requirement of maintaining a reasonable scan time ($<$ 30 minutes). The analysis in this dissertation shows that 3D encoding is required for high isotropic resolution because of its superior performance in SNR efficiency (the achieved SNR over a unit of scan time) as compared to the 2D techniques. From the SNR analysis, the dissertation proposes a 3D multislab acquisition technique for achieving $1.88 \times 1.88 \times 2$ mm^3 resolution with full brain coverage within 14.4 minutes and a 3D fast spin echo acquisition for achieving $0.8 \times 0.8 \times 1$ mm^3 resolution with reduced field of view coverage within 22 minutes. Acquisition techniques and post processing algorithms have also been developed for correcting/minimizing common artifacts in DTI including motion-induced phase error, magnetic susceptibility and eddy currents. Simulation, phantom, and *in vivo* results are included to verify the performance of the proposed methods.

Con kính tặng Ba Mẹ

ACKNOWLEDGMENTS

First, I would like to thank my adviser, Professor Brad Sutton, who has given me tremendous support in various aspects of my work, from guiding the research directions to detailed implementation of the work to being a very patient subject for my experiments.

I would also like to thank Professor Minh Do for without his interview and then recommendation six years ago, I would not have been here at UIUC. I am also grateful to anh Minh for his advice and support when I had difficulties in choosing a research focus.

Professor Steven S. Lumetta was my first adviser at UIUC and I would like to thank him for his guidance during my very early stage of graduate school and research career. My programming experience, analytical skills, and English writing and speaking skills were greatly refined through working with Steve.

I am grateful to my doctoral committee members, Professors Yoram Bresler, Minh Do, Zhi-Pei Liang, and Brian Gonsalves, for their constructive comments that helped improve my work.

I would like to extend my thanks to Dimitris for his constant help and encouragement through the course of my PhD study. I really appreciate his assistance in data acquisition, help in early pulse sequence programming, and constructive comments on my work. Furthermore, without him, the disappointment of unsuccessful experiments, paper rejections, and unanswered job applications would be much tougher.

I would also like to thank my lab mates, Ouyang, Joy, Chas, Tom, and Joe, not only for their support in long night scans, late night rides, and research discussions, but also for all the fun we had together in and outside the lab.

I would like to thank my other colleagues, Diego, Curtis, Danchin, and Armen.

I would like to acknowledge the support from the Biomedical Imaging Center (BIC),

Beckman Institute and the Vietnam Education Foundation (VEF).

I am also very grateful to JP Peters and the ECE Publications Office for the careful edits to this dissertation.

Six years is a long time, especially when one is far away from her family and her country. I am very grateful that I have so many great friends here for this long journey. Anh Chinh, Phuong, Loc, Nam gia, Huyen U, Loan, anh Long (anh Bi), Khoi, chi Ly, anh Tung, Hieu, Duc Ngo, Hoang beo, Ngu, anh Kien: Thank you all for making UIUC a home away from home for me and for filling my rough PhD journey with tons of fun and exciting experiences.

Last but not least, I am deeply grateful to my family: my parents, my sister, my brother-in-law, and my little niece. Their constant love, encouragement, and support have helped me all the way and brought me to the destination of my PhD study. This thesis is dedicated to them.

TABLE OF CONTENTS

LIST OF TABLES

LIST OF FIGURES

LIST OF ABBREVIATIONS

ADC	apparent diffusion coefficient
CG	conjugate gradient
CNS	central nervous system
CSF	cerebrospinal fluid
DFT	discrete Fourier transform
DPS	direct phase subtraction
DTI	diffusion tensor imaging
DWI	diffusion-weighted imaging
DW-PGSE	diffusion-weighted pulse gradient spin echo
DW-SSFP	diffusion-weighted steady state free precession
EPI	echo planar imaging
FA	fractional anisotropy
FFT	fast Fourier transform
FOV	field of view
GRAPPA	generalized autocalibrating partially parallel acquisitions
IVI	inner volume imaging
KICT	k-space and image space combination
MRI	magnetic resonance imaging
NMR	nuclear magnetic resonance
NRMSE	normalized root mean squares error

OVS	outer volume suppression
PP	perforant pathway
PROPELLER	periodically rotated overlapping parallel lines with enhanced reconstruction
QPWLS	quadratically-penalized weighted least squares
RA	relative anisotropy
RF	radio frequency
RMS	root mean square
SAR	specific absorption rate
SD	standard deviation
SENSE	sensitivity encoding
SNR	signal-to-noise ratio
TE	echo time
TR	repetition time
VD	variable density
VR	volume ratio
ZOOM	zonal oblique multislice

CHAPTER 1

INTRODUCTION

1.1 Diffusion Imaging: Insight into Neuronal Architectures

Microstructural organization of the central nervous system (CNS) neuronal architectures is becoming increasingly interesting as a physiological indicator in a variety of diseases. For diagnosis and treatment purposes, it is highly desired to have tools for measuring the integrity and quantitatively characterizing the status of neuronal networks. Magnetic resonance imaging (MRI) with its multiple contrast mechanisms provides a noninvasive tool to create these measurements. Using a large static magnetic field and radio frequency (RF) pulses to align and excite spins in the imaged object and produce measurable magnetization signals, along with gradient fields for spatial encodings, MRI gives images of internal physical and chemical characteristics of the object. However, the current imaging techniques are limited by their ability to resolve the fine structures that compose critical neuronal pathways.

Based on diffusion measurement in nuclear magnetic resonance (NMR) [1], diffusion-weighted imaging was introduced in the mid-1980s [2–4]. Diffusion-weighted imaging is an MRI technique that encodes the diffusion or the random translational motion of molecules, usually water, in a medium. During their random, diffusion-driven displacements, water molecules probe a medium (tissue) structure at a microscopic scale well beyond the usual image resolution [5]. As diffusion is truly a three-dimensional process, molecular mobility in tissues may be anisotropic primarily due to the restriction of the tissue membranes or obstacles such as organelles. With diffusion tensor imaging (DTI), diffusion anisotropy effects can be fully extracted, characterized, and exploited, providing exquisite details of tissue microstructure.

DTI has proven itself as a powerful tool to noninvasively assess neuronal integrity and

connectivity in the central nervous system. DTI metrics such as apparent diffusion coefficient (ADC), relative anisotropy (RA), fractional anisotropy (FA), and volume ratio (VR) are quantitative measurements of the physical properties of the tissues. Changes in DTI metrics can be used to diagnose the physiological state of the structured tissues. DTI has already shown its potential in many types of diseases. ADC measurements have been used to diagnose diseases that relate to changes in the overall water content within the affected tissues such as in brain ischemia [6–8]. In brain white matter, anisotropy indices indicate myelin fiber integrity, and mylenation process [9–11], which finds its application in multiple scelrosis [12–15], leukoencephalopathy [16], Alzheimer's disease [17, 18], and aging [19].

Together with fiber tracking algorithms, diffusion anisotropy can provide anatomical measures of brain connectivity which are of great importance for interpreting functional MRI data and establishing how activated foci are linked together through networks. Even at its current stage, DTI is one of the few approaches available to track brain white matter noninvasively.

1.2 Challenges of DTI

Powerful and useful as it is, in order for DTI to reach its full potential of describing detailed neuronal structures, it still has to overcome many challenges such as partial volume effects, off-resonant artifacts, motion-induced phase errors, and eddy currents [5, 20–22]. In the following subsections, a basic review of these challenges is given. Each of the challenges will be addressed in the thesis as we develop a robust high-resolution diffusion tensor imaging platform. For successful DTI experiments, all of the challenges have to be taken into account in experiment setup, sequence design, image reconstruction algorithm, and post-processing algorithms.

1.2.1 Partial Volume Effects

Although the diffusion is a microscopic process, the information given by DTI is averaged over the imaging voxel, which leads to the well-known partial volume effect in MRI [23].

Because of this partial volume effect, both the accuracy of the derived anisotropy metrics and the performance of DTI tractography rely on the spatial resolution of the diffusion-weighted images in order to resolve fine-scale structures of interest. There have been many studies on modeling, evaluating, and suppressing partial volume effects in DTI [23–28]. The spatial distribution of partial volume effects can be categorized into regions containing nonparallel white matter tracts (crossing or merging fibers), white matter and gray matter, white matter and CSF, and gray matter and CSF. Partial volume effects in regions with nonparallel white matter tracts cause a decrease in the estimation of the FA values and errors in the estimation of the principle diffusion direction [29]. In regions containing both white matter and gray matter, partial volume effects result in overestimation of FA values in voxels that contain mostly gray matter and underestimation of FA values in voxels that contain mostly white matter. Since CSF has high diffusion coefficient and shows isotropic diffusion properties, partial volume effects in regions with white matter and CSF and gray matter and CSF cause a decrease in FA estimation and an increase in ADC estimation. To limit the partial volume effects, at the modeling level, more complicated models, such as higher order models of the diffusion process in tissue are needed [23]. At the imaging level, higher spatial resolution is required, especially in small and complicated neuronal structures such as the brain stem and the hippocampus where small neuronal fiber populations exist in varying orientations to form the complex structures [28, 30–32].

1.2.2 Off-Resonance

For DTI with whole brain coverage or DTI of structures that are surrounded by fat or close to the air/tissue interfaces, magnetic field inhomogeneity or off-resonance effect is a big challenge.

Essentially, off-resonance is the effect in which certain spins have a slightly different frequency than the resonance frequency due to the different chemical nature of the molecules that the spins belong to (such as fat vs. water) or the disruption in the magnetic field within the tissue (such as near air/tissue boundaries). If the off-resonance effect is microscopic, meaning that the frequency variation happens within an imaging voxel, signal loss

will occur. If the off-resonance effect is macroscopic, the resulting uncorrected image will suffer from geometric distortion and blurring due to the difference in the actual magnetic field that the spins experienced and the prescribed one.

The exact effect of off-resonance-induced distortion artifacts depends on the data acquisition (k-space) trajectory and timing. For a Cartesian acquisition (i.e. echo planar imaging (EPI)), susceptibility causes a significant geometric shift in image space along the slow-acquisition axis, i.e. the phase encode axis. For a spiral trajectory, the slow-acquisition axis is in the radial direction and blurring results in the radial direction.

Off-resonance effects can be reduced significantly by reducing the readout time. Readout time can be reduced by increasing the receiver bandwidth, using parallel imaging, or using multishot acquisition. Multishot acquisition is a technique in which the k-space data are divided into multiple parts, called shots, and only one part is acquired during a repetition of the sequence. As compared to single-shot acquisition, the readout time in a multishot acquisition and, therefore, image distortions, are reduced by a factor that is equal to the number of shots.

In addition to minimizing the effects of magnetic susceptibility as mentioned above, correction for off-resonance effects can be done at the sequence design level (fat saturation, shimming) and/or during the post-acquisition (field inhomogeneity correction using accompanied field maps).

1.2.3 Motion-Induced Phase Errors

In DTI acquisitions, the imaging sequence is made to be sensitive to the diffusion process within the structures of interest. That sequence, therefore, is also sensitive to other types of motion, including patient motions and pulsations of tissues induced by the cardiac cycle [20, 21].

During a diffusion-weighted acquisition, coherent motion within an imaging voxel results in an additional phase term applied to the image value representing that voxel. Incoherent motion within an imaging voxel results in a change in the magnitude of the image value representing that voxel. While incoherent motion degrades the quality of diffusion-weighted

images in all acquisition strategies, coherent motion only affects multishot acquisitions.

In multishot DTI, patient motion is likely to be different in different applications of the diffusion gradient pulses during different shots. Therefore, each shot in a multishot acquisition is perturbed differently, which leads to shot-dependent phase errors and undesired signal cancellations when data from different shots are combined. The reconstructed images suffer from severe artifacts if these phase errors are not accounted for.

Because of their immunity to coherent motion, single-shot imaging techniques, especially single-shot echo planar imaging (EPI), are commonly used in clinical applications. Although multishot acquisitions in DWI suffer from motion-induced phase errors, they are sometimes preferred to their single-shot counterparts because of their reduced sensitivity to magnetic susceptibility off-resonance effects and T2* decay as discussed earlier.

Many studies have been done to compensate for motion artifacts in multishot DTI [33–47]. All methods require navigator data for error estimation. The correction then is done in k-space [33, 36, 42, 45], in image-space [38, 41], or during diffusion-weighted image reconstruction [43, 44].

1.2.4 Eddy Currents

Another artifact that presents a challenge for DTI acquisitions is eddy currents. Eddy currents affect both single- and multishot diffusion-weighted acquisition. In DTI sequences, diffusion encoding is realized by gradient pulses with near-maximum allowable amplitude. When these strong gradient pulses are switched on and off, the time-varying magnetic field of the gradients results in current induction (eddy currents) in the various conducting surfaces of the MRI scanner [20]. These eddy currents set up magnetic field gradients that may persist after the primary gradients are switched off.

If the imaging gradients are placed such that the eddy-current-induced gradients are still significant, the actual gradients experienced by spins in the imaging object will be different from the prescribed gradients. Image reconstruction algorithms that do not take into account the changes in these encoding gradients will result in distorted images. The distortion patterns include contraction or dilation of the image, and overall shift and shear [20,48]. For

DTI, the diffusion indices are extracted from diffusion-weighted images with different diffusion encoding directions and therefore different eddy-current-induced distortions. Image-to-image distortion variation leads to blurred and inaccurate maps of diffusion metrics.

Another source of inaccuracy in diffusion metric estimation due to eddy currents is the difference between the actual b value and the programmed b value. This artifact would result in errors in estimation of the diffusion metrics.

Compensation for eddy currents has been done in hardware [49] (self-shielded gradient coils, birdcage RF coils, preemphasis), pulse sequence [50–52], and post processing [48,53,54].

1.3 Objectives and Contribution

The objective of this thesis is to obtain high-resolution diffusion-weighted images and high quality diffusion metric maps both for whole brain coverage and localized neuronal structures. Specifically, the thesis addresses three problems:

- developing a robust algorithm to compensate for motion-induced phase errors in 2D and 3D multishot diffusion-weighted imaging (DWI).
- developing a 3D DTI acquisition strategy that can give high resolution diffusion-weighted image with reasonable SNR, limited motion-induced phase errors, limited eddy current effects, limited susceptibility and off-resonant effects within reasonable scan time.
- obtaining sub-millimeter resolution by combining a 3D DTI acquisition with reduced field-of-view (FOV) strategy and applying the developed technique to image important localized neuronal structures of the pons and the hippocampus.

3D DTI is highly desired because of its ability to deliver high isotropic resolution images and hence more precise estimation of the diffusion properties of biological tissues at a finer spatial scale. However, there have been only a few studies of 3D DTI, all of which are 3D steady-state free precession diffusion-weighted techniques. To the best of our knowledge, this thesis is the first to introduce 3D pulsed gradient spin echo DTI with six directions,

$2 \times 2 \times 2$ mm isotropic whole brain coverage with a subject-tolerable scan time of approximately 20 minutes. Unlike DTI using steady state free precession acquisition, DTI using pulsed gradient spin echo allows straightforward modeling of the diffusion-weighted signals, which gives easier estimation of the diffusion metrics. Furthermore, the resulting high resolution 3D DTI data will greatly improve the performance of DTI tractography, giving a more accurate and complete brain connectivity map.

For imaging localized neuronal structures, we push the image resolution to the sub-millimeter level. The achieved sub-millimeter resolution DTI ($0.8 \times 0.8 \times 1$ mm^3) of localized neuronal structures makes it possible to delineate and detect any subtle changes in neuronal architecture of fine white matter structures that are implicated in a variety of pathology.

1.4 Organization of the Dissertation

The remainder of the dissertation is organized as follows.

Chapter 2 starts with a brief introduction of the principles of diffusion-weighted imaging (DWI). Common artifacts together with their existing compensation methods are reviewed. Additionally, this chapter also discusses existing acquisition strategies for high resolution full brain and localized anatomies.

Chapter 3 describes the proposed k-space and image-space correction technique (KICT) for robust motion-induced phase error (MiP) correction in 2D DWI. The distinct feature of KICT lies in its ability to perform the correction in k-space, which eliminates residual phase errors that persist in some of the previously proposed correction strategies regardless of the choice of multishot k-space trajectory. The performance of the proposed algorithm is tested with both simulated data and *in vivo* data. Comparison with existing algorithms is also presented.

Chapter 4 introduces a novel acquisition strategy for 3D high-resolution full brain diffusion-weighted imaging. The key feature of the proposed strategy is the multislab acquisition, which enables significantly reduced total scan time for an otherwise impractical conventional 3D spin echo diffusion-weighted acquisition. Techniques and algorithms for mitigating eddy current artifacts and motion-induced phase errors are also provided.

Chapter 5 describes the necessity of and the algorithm for correcting magnetic susceptibility artifacts in 3D. This ability to correct for the magnetic susceptibility artifact enables further reductions in total scan time or higher spatial resolution.

Chapter 6 deals with submillimeter resolution DTI of localized anatomies. With reduced field-of-view imaging and fast spin echo acquisition, DTI resolution of $0.8 \times 0.8 \times 1$ mm^3 is realized.

Chapter 7 concludes the thesis by giving a summary of all the projects, discussing the remaining challenges, and proposing future developments.

CHAPTER 2

DIFFUSION-WEIGHTED IMAGING

2.1 Introduction to Diffusion-Weighted Imaging

Diffusion-weighted imaging (DWI) is a magnetic resonance imaging (MRI) technique that encodes displacement of diffused water using magnetic gradients and interrogates tissue microstructure. Essentially, diffusion is a random motion (Brownian motion) of molecules, and hence spins, in a medium. With 1D unrestricted diffusion, the root mean square (RMS) displacement in a period of time t is [55]

$$r = \sqrt{2Dt} \tag{2.1}$$

where D is a diffusion coefficient that depends on the mobility of the molecules and the temperature of the medium. D is measured in distance squared per unit time (e.g. mm^2/s).

In biological tissues, diffusion of water is restricted by macromolecules and tissue structure. At each spatial location, the 3D diffusion boundary is ellipsoidal with three RMS displacements r_1, r_2, r_3 satisfying

$$\begin{aligned} r_1 &= \sqrt{2D_1t} \\ r_2 &= \sqrt{2D_2t} \\ r_3 &= \sqrt{2D_3t} \end{aligned} \tag{2.2}$$

where D_1, D_2, and D_3 are the apparent diffusion coefficients along the axes of the diffusion ellipsoid shown in Figure 2.1.

To enhance the sensitivity to water diffusion in the imaging object, diffusion weighted gradients are added to standard imaging sequences. Basic diffusion weighted gradients are composed of two pulses with equal area. The pulses are of opposite polarity so as to not

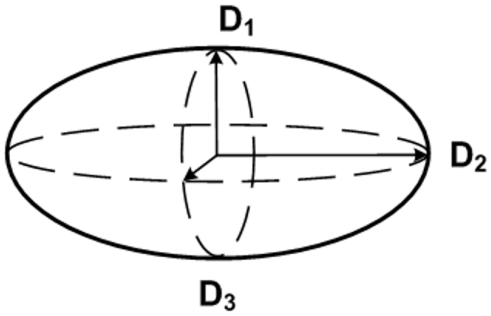

Figure 2.1: Restricted diffusion ellipsoid.

result in any net spatial encoding.

An example of diffusion weighted gradient used in spin-echo pulse sequence is shown in Figure 2.2.

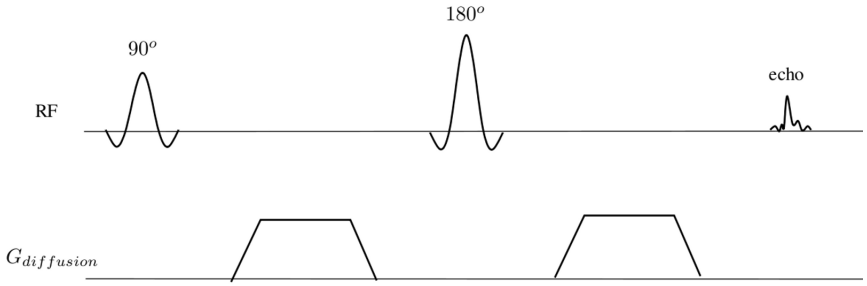

Figure 2.2: Diffusion weighted gradient in spin-echo pulse sequence.

The purpose of the gradient pulses is to magnetically label spins carried by molecules. Let the gradient strength, the gradient duration, and the interval between the onsets of the gradient pulses be G, δ, and Δ, respectively. Without loss of generalization, let us assume that the gradient pulses are applied on the z-direction and the pulse duration δ is small enough so that spin position is constant during δ; then the first gradient pulse induces on spin at location z_1 a phase shift

$$\phi_1 = \gamma \int_0^{\delta} G z_1 \mathrm{d}t = \gamma G \delta z_1 \tag{2.3}$$

Similarly, the second gradient pulse will produce a phase shift ϕ_2 to spin at location z_2

$$\phi_2 = \gamma \int_{\Delta}^{\Delta+\delta} G z_2 \mathrm{d}t = \gamma G \delta z_2 \tag{2.4}$$

Taking into account the effect of the 180^o refocusing pulse, the net dephasing is

$$\delta(\phi) = \phi_2 - \phi_1 = \gamma G \delta (z_2 - z_1) \tag{2.5}$$

Clearly, for static spins ($z_1 = z_2$), the bipolar gradient pair produces no net dephasing. For diffusing spins, however, there is a net dephasing that depends on the spin positions at the end of the first pulse and at the beginning of the second pulse. Let M_0 be the total transverse magnetization when no gradient pulses are applied (no additional dephasing of the spins). Let M be the total transverse magnetization when gradient pulses are applied. For impermeable boundaries, we have

$$\frac{M}{M_0} = E_{z_1}\Big[E_{z_2}\big[\exp(j\delta(\phi))|z_1, \Delta\big]\Big] \tag{2.6}$$

where E_x is the expectation taken on the x variable.

Free diffusion in one dimension is a Brownian motion with parameter $2D$ (Equation (2.1)) where D is the diffusion coefficient that depends on the mobility of the molecules, the concentration, and the temperature of the medium. Therefore, we have $(z_2 - z_1) \sim \mathcal{N}(0, 2D\Delta)$ where z_2 is the position of the spin initially at z_1 after a time interval Δ. The distribution of the spins initially at z_1 after a time interval Δ then is

$$f(z_2|z_1, \Delta) = \frac{1}{\sqrt{4\pi D\Delta}} \exp\left(\frac{-(z_2 - z_1)^2}{4D\Delta}\right) \tag{2.7}$$

Let $p(z_1)$ be the distribution of spin location at a certain point in time. Then from

Equations (2.5), (2.6), and (2.7) we obtain

$$\begin{aligned}
\frac{M}{M_0} &= \int_{-\infty}^{\infty}\int_{-\infty}^{\infty} \exp\Big(j\delta(\phi)\Big) f(z_2|z_1,\Delta)p(z_1)\mathrm{d}z_1\mathrm{d}z_2 \\
&= \int_{-\infty}^{\infty}\int_{-\infty}^{\infty} \exp\Big(j\gamma G\delta(z_2-z_1)\Big)\frac{1}{\sqrt{4\pi D\Delta}}\exp\Big(\frac{-(z_2-z_1)^2}{4D\Delta}\Big)p(z_1)\mathrm{d}z_1\mathrm{d}z_2 \\
&= \frac{1}{\sqrt{4\pi D\Delta}}\int_{-\infty}^{\infty}\int_{-\infty}^{\infty} \cos\Big(\gamma G\delta u\Big)\exp\Big(\frac{-u^2}{4D\Delta}\Big)p(z_1)\mathrm{d}u\mathrm{d}z_1 \\
&= \exp\Big(-(\gamma G\delta)^2 D\Delta\Big)
\end{aligned} \tag{2.8}$$

In conclusion, with the presence of magnetic field gradients, diffusion causes exponential attenuation of the transverse magnetization.

In order to simply illustrate the effect of diffusion encoding, the result in Equation (2.8) was obtained with the following assumptions:

- $\delta << \Delta$.
- There is no other gradients than the diffusion encoded ones.
- Diffusion in the interested object is free and isotropic.

In reality, none of the above assumptions are valid. To relax these assumptions, one must solve the Bloch equation with diffusion, or the Bloch-Torrey equation [56]. In the laboratory frame of reference, the Bloch-Torrey equation takes the form [56, 57]

$$\frac{\partial \mathbf{M}}{\partial t} = \gamma \mathbf{M}\times\mathbf{B} - \begin{pmatrix} \frac{1}{T_2} & 0 & 0 \\ 0 & \frac{1}{T_2} & 0 \\ 0 & 0 & \frac{1}{T_1} \end{pmatrix}\mathbf{M} + \mathbf{M_0}\begin{pmatrix} 0 \\ 0 \\ 1/T_1 \end{pmatrix} + \nabla \cdot (\underline{\mathbf{D}}\nabla\mathbf{M}) \tag{2.9}$$

where $\mathbf{B} = (B_x, B_y, B_z)$ is the applied magnetic field vector, which is the superposition of the static magnetic field and the gradient field $\mathbf{G}(t) = (G_x(t), G_y(t), G_z(t))$ (if any) applied in the z direction

$$\mathbf{B}(\mathbf{r},t) = (0, 0, \mathbf{r}\cdot\mathbf{G}(t) + B_0) \tag{2.10}$$

$\underline{\mathbf{D}}$ is the diffusion tensor describing the diffusion anisotropy at each spatial location and has the form

$$\underline{\mathbf{D}} = \begin{bmatrix} D_{xx} & D_{xy} & D_{xz} \\ D_{yx} & D_{yy} & D_{yz} \\ D_{zx} & D_{zy} & D_{zz} \end{bmatrix} \tag{2.11}$$

$\mathbf{M} = (M_x, M_y, M_z)$ is the net magnetization vector, γ is the gyromagnetic ratio, T_1 and T_2 are the longitudinal and transverse relaxation times, and $\mathbf{M_0}$ is the equilibrium magnetization in the direction of the static magnetic field $\mathbf{B_0}$.

Let $m(\mathbf{r}, t)$ be the complex-valued representation of the transverse magnetization, meaning

$$m(\mathbf{r}, t) = M_x(\mathbf{r}, t) + jM_y(\mathbf{r}, t) \tag{2.12}$$

The Bloch equation for $m(\mathbf{r}, t)$ can be expressed as

$$\frac{\partial m}{\partial t} = -j\omega_0 m - \frac{m}{T_2} - j\gamma \mathbf{r} \cdot \mathbf{G}(t)m + \nabla \cdot (\underline{D}\nabla m) \tag{2.13}$$

where the Larmor frequency $\omega_0 = \gamma B_0$. Noticing that m is a vector in the complex $x - y$ plane that precesses about the z axis at the frequency $-\omega_0$ and without diffusion, m is exponentially decayed with relaxation time T_2. Therefore, m has the form

$$m(\mathbf{r}, t) = \psi(\mathbf{r}, t) \exp\Big(- \big(j\omega_0 + \frac{1}{T_2}\big)t\Big) \tag{2.14}$$

and

$$\frac{\partial \psi}{\partial t} = -j\gamma \mathbf{r} \cdot \mathbf{G}(t)\psi + \nabla \cdot (\underline{D}\nabla \psi) \tag{2.15}$$

$\psi(\mathbf{r}, t)$ can further be simplified into a part corresponding to the solution of Equation (2.15) without diffusion, and a part corresponding to diffusion effect only

$$\begin{aligned} \psi(\mathbf{r}, t) &= M(t) \exp\Big(- j\gamma \int_0^t \mathbf{r} \cdot \mathbf{G}(t')\mathrm{d}t'\Big) \\ &= M(t) \exp\Big(- j\mathbf{r} \cdot \mathbf{k}(t)\Big) \end{aligned} \tag{2.16}$$

where

$$\mathbf{k}(t) = \gamma \int_0^t \mathbf{G}(t')\mathrm{d}t' \tag{2.17}$$

From Equations (2.15) and 2.16, the equation for $M(t)$ is

$$\frac{\mathrm{d}M}{\mathrm{d}t} \exp\Big(- j\mathbf{r} \cdot \mathbf{k}(t)\Big) = M(t)\nabla \cdot \Big(\underline{D}\nabla \exp(-j\mathbf{r} \cdot \mathbf{k}(t))\Big) \tag{2.18}$$

or

$$\frac{\mathrm{d}M}{\mathrm{d}t} = -M(t)\mathbf{k}(t)^T \underline{D}\mathbf{k}(t) \tag{2.19}$$

A solution for Equation (2.19) is

$$M(t) = M(0) \exp\left(- \int_0^t \mathbf{k}(u)^T \underline{D}\mathbf{k}(u)\mathrm{d}u\right) \tag{2.20}$$

where $M(0)$ is the amplitude of the transverse magnetization right after the excitation pulse.

For spin echo sequence, at TE, the effect of diffusion on the transverse magnetization is

$$\frac{M(TE)}{M(0)} = \exp\left(- \int_0^{TE} \mathbf{k}(u)^T \underline{D}\mathbf{k}(u)\mathrm{d}u\right) \tag{2.21}$$

Define b matrix as

$$b_{ij} = \int_0^{Te} \Big(\mathbf{k}(u) \otimes \mathbf{k}(u)\Big)_{ij} \mathrm{d}u \tag{2.22}$$

where $(\mathbf{k}(u) \otimes \mathbf{k}(u))_{ij}$ is taking the ij^{th} entry of the result of the outer product of the vector $\mathbf{k}(u)$ with itself. Equation (2.21) is simplified to

$$\frac{M(TE)}{M(0)} = \exp\Big(- \sum_{i=1}^{3}\sum_{j=1}^{3} b_{ij}D_{ij}\Big) \tag{2.23}$$

where D_{ij}'s are the entries of the tensor matrix $\underline{D}$.

2.2 Acquisition Strategies for High Resolution DTI

Diffusion tensor imaging (DTI) [5, 58] accompanied with fiber tracking algorithm [59] has emerged as an important tool for assessing white matter connectivity and integrity in the central nervous system, especially in the cerebral cortex. Both the accuracy of the derived anisotropy metrics [29] and the performance of DTI tractography [60–62] improve as the resolution of the acquisition increases. The spatial resolution, however, is upper-bounded by the desired signal-to-noise-ratio (SNR) of the diffusion-weighted images [55].

With careful positioning of the imaging slices to take advantage of known structure in localized anatomies, current 2D DTI acquisition techniques sacrifice through-plane resolution to obtain high isotropic in-plane resolution with adequate SNR. Examples of the resolution reported in recent whole brain 2D DTI studies are 0.86 x 0.86 x 6.5 mm^3 and 0.47 x 0.47 x 8 mm^3 [41, 43]. Examples of the resolution achieved for targeted DTI acquisitions of localized anatomical structures are 0.62 x 0.62 x 5 mm^3 at the spinal cord [63], 0.8 x 0.8 x 3.0 mm^3 [28], and 1.0 x 1.0 x 1.5 mm^3 [64] at the brain stem.

In regions of complex neural fiber architectures, or when full brain coverage is needed, high in-plane resolution only is not adequate because of increased partial volume effects in the slice selective direction. Two-dimensional acquisition with reduced slice thickness is challenging and limited by the requirement for high slice selection gradient and narrow radio frequency (RF) pulse bandwidth, as well as the resulting low SNR images. A common solution to overcome the challenges for thin slice 2D acquisitions is the implementation of 3D acquisitions.

In 3D imaging, spatial information in the third dimension (corresponding to the slice-selective dimension in the 2D cases) is achieved using Fourier encoding. Therefore, higher spatial resolution in the third dimension than that in 2D imaging can be realized without reaching the gradient and RF hardware limitations. Furthermore, for a similar repetition time (TR), 3D acquisitions gives an SNR gain of approximately $\sqrt{N_z}$ compared to 2D acquisitions, where N_z denotes the ratio between the total readout time for a 3D volume and the total readout time for a 2D slice [55].

In the following subsections several strategies for high resolution 3D full brain DTI and

2D/3D localized anatomy DTI are reviewed together, highlighting their advantages and disadvantages. Our own work is included in the review to add perspective of recent developments in this area. Details of our proposed acquisition to optimized 3D PGSE for whole brain and reduced field of view coverage is described later in Chapter 4 and Chapter 6, respectively.

2.2.1 Full Brain Acquisition

Although 3D DTI is a must for achieving high isotropic resolution, the implementation of 3D full brain DTI acquisitions is complicated by multiple challenges that have prevented its development until recently. Challenges for 3D DTI with full brain coverage include but are not limited to: developing a simple, time-efficient combination of diffusion preparation and 3D acquisition, robust 3D artifact estimation and correction, and fast 3D image reconstruction.

To the best of our knowledge, the first attempt at high resolution 3D full brain DTI was by Zhang et al. in [65]. The diffusion preparation was diffusion-weighted spoiled gradient-recalled echo with a small b-value of 400 s/mm^2. The trajectory used was the radialized variable density spiral. The whole 3D k-space is fully sampled by a set of radial 2D planes each of which is composed of multiple shots of variable density spiral. 3D self-navigating for motion-induced phase error correction (discuss in Section 2.3) was enabled by adding a continuous oscillating through-plane gradient for a short duration at the beginning of each spiral shot. Although reasonable diffusion-weighted images with isotropic resolution of 1.88 mm^3 were reported, no successful diffusion metrics maps were reported [65].

The later attempts at 3D full brain DTI acquisition can be divided into two directions: diffusion-weighted pulsed gradient spin echo (DW-PGSE, including fast spin echo) [66, 67], and diffusion-weighted steady state free precession (DW-SSFP) [65, 68–70].

For most of diffusion-weighted acquisition, DW-PGSE is usually used because of its simple implementation, straightforward diffusion-weighted signal model, and high SNR. For 3D full brain DTI, however, the biggest disadvantage of the DW-PGSE is its long total acquisition time resulting from a significant unavoidable time for signal T1 recovery.

Fast spin echo acquisitions and multislab approaches have been proposed for speeding up

the 3D DW-PGSE by maximizing the data acquisition during the T1 recovery time. Fast spin echo acquisition for 3D DTI was first proposed by Frank et al. in [71] to reduce the total scan time of 3D DW-PGSE acquisition. The main challenge in the implementation of the fast spin echo approach is the requirement to maintain the CPMG condition in the presence of phase instability due to eddy currents and motion during the diffusion encoding [71]. The trajectory used was a stack of multishot variable density spirals. Two-dimensional self-navigating capacity of the variable density spirals was used for phase error estimation. Therefore, phase error correction was restricted to 2D, leading to incomplete phase error cancellation. Nevertheless, reasonable diffusion-weighted images and diffusion metric maps at 1.8 mm^3 resolution were reported for an axial slab of 28.8 mm thickness around the level of corpus callosum [71] in 14 minutes [71].

Three-dimensional multislab acquisitions speed up the 3D DW-PGSE acquisition by utilizing the recovery time after the excitation of one slab to acquire data for other slabs [66,67]. A challenge for multislab acquisition is the occurrence of slab boundary artifacts resulting from imperfect slab selection profile. Slab oversampling, slab overlapping, and sliding window acquisition can be used to mitigate the boundary effects [66, 67]. Three-dimensional multislab acquisition for full brain DTI was reported in [66, 67]. However, reasonable diffusion-metric maps were achieved only in our own work reported in [66].

Unlike DW-PGSE, faster DTI acquisition can be achieved with DW-SSFP without the need to consider special acquisition strategies to reduce the total scan time [65, 68–70]. However, the signal in DW-SSFP originates from a combination of spin echoes and stimulated echoes, which results in a more complicated diffusion weighting than in DW-PGSE [72, 73]. Furthermore, because of short repetition time (TR), the signal of DW-SSFP sequences is also weighted by both T1 and T2, and it is necessary to measure these relaxation times separately in order to estimate the diffusion metrics. Besides the difficulty in interpreting image contrast, the capability to do either self-navigating or separate navigating for motion-induced phase error correction in DW-SSFP is limited due to the required short TR for maintaining the steady-state condition.

Jung et al. reported a 3D *in vivo* full brain DTI study using cardiac-gated DW-SSFP with 3D radial trajectory [68]. Four radial k-space lines were collected per TR for increasing ac-

quisition efficiency. Self-navigating capability of the 3D radial was used for motion-induced phase error estimation. Since only four radial lines were collected per TR, the k-space coverage in the radial direction was very limited, which suffers from insufficient phase error estimation. Diffusion metric maps were achieved at the resolution of 1.88 mm^3 in 18 minutes [68].

Another attempt in 3D full brain DW-SSFP was reported in [65] using radialized variable density spiral trajectory. However, the achieved diffusion metric maps were significantly corrupted by motion-induced artifacts.

Ignoring the difficulty in estimating the b-value used in the experiment, when motion is not a concern, such as in *ex vivo* or *in vitro* (phantom) experiments, DW-SSFP is an excellent acquisition method for 3D full brain DTI, as demonstrated by McNab et al. in [70]. However for quantitative metrics in normal subjects or patients, DW-PGSE is required.

2.2.2 Localized Anatomies

As stated earlier, the first consideration of any acquisition strategy when moving to higher resolution is SNR. However, another major concern is the increased sensitivity to various artifacts including but not limited to susceptibility, eddy currents, and motion. Most of these artifacts, at least susceptibility, eddy currents, and motion, can be reduced by decreasing the readout duration and/or decreasing the total acquisition time. For localized anatomy imaging, decreasing the readout duration while maintaining the total acquisition time (and vice versa) as compared to a lower resolution acquisition is achievable by using a reduced-field-of-view (rFOV) acquisition at a cost of a reduction in SNR. In rFOV acquisition, the actual FOV imaged is just the anatomy of interest. Signals from other regions are suppressed so that no aliasing occurs.

Reduced-FOV acquisitions to reduce the readout duration and/or total acquisition time and achieve higher spatial resolution in localized regions have been reported in the 2D DTI literature. Four main approaches have been proposed: inner volume imaging (IVI), zonal oblique multislice (ZOOM) imaging [74], outer volume suppression (OVS) imaging [75], and inner volume excitation (IVE) [32, 63]. IVI plays the slice-selective gradient of the

RF refocusing pulse on the phase-encoding axis in order to isolate the anatomical region of interest. The major disadvantage of IVI is that it is limited to single-slice acquisitions. ZOOM is a refinement of IVI designed to allow interleaved multislice acquisitions. Since it employs tilted refocusing pulses, ZOOM suffers from the need to acquire a large number of slices in order to cover the region of interest. OVS is based on imposing spatially selective pulses in the outer volume regions followed by spoiling gradients. Other than the potentially poor performance of the saturation pulses, the main disadvantage of OVS is in limiting the number of slices per TR to a maximum number imposed by specific absorption rate (SAR) constraints. Inner volume excitation employs a two-dimensional excitation pulse with independent control over the in-plane and the slice-selective axes. The disadvantages of inner volume excitation lie in the complexity of the 2D pulse design and long excitation duration. Inherent long acquisition time and higher through-plane resolution present difficult challenges for achieving adequate SNR in reduced-field-of-view acquisitions, which will be discussed in Chapter 6

One of the most important challenges of 2D reduced-FOV imaging is the resulting decrease in SNR. Current 2D reduced-FOV techniques compensate for this decrease in SNR by acquiring data with relatively thick slices, resulting in high anisotropic voxels. Table 2.1 lists the resolutions obtained in some of the studies in the literature.

2.3 Motion-Induced Phase Errors in Diffusion-Weighted Imaging

2.3.1 Motion Effects on Diffusion Encoding

In DWI, diffusion gradient pulses are added to imaging pulse sequences to enhance sensitivity to water molecule random motion. Unfortunately, these gradients are also sensitive to any other types of motion such as patient motion or cardiac-induced brain pulsation. When these unwanted, nonrandom motions are such that motions of spins within an imaging voxel are incoherent, permanent signal loss occurs. When patient motion or pulsation gives rise to coherent motion of spins within an imaging voxel, a constant phase-offset is added to the net magnetization in that voxel.

Table 2.1: 2D reduced-FOV previously achieved resolutions. Time is the average scan time per diffusion-encoded direction and is computed as the total scan time divided by the number of diffusion-encoded directions and the number of averages. ss-EPI stands for single-shot EPI, PF stands for partial Fourier encoding. Notice that all the 2D rFOV acquisitions were applied on regions that have small fiber orientation variation in one direction and thick slices were used.

Study	Resolution (mm^3)	rFOV	Encoding	Time
Optical nerve [74]	1.25 x 1.25 x 4	ZOOM	?-channel, ss-EPI	3.44 s
Spinal cord [63]	0.62 x 0.62 x 5	IVE	8-channel, ss-EPI, 62.5% PF	1 s
Spinal cord [32]	0.50 x 0.50 x 5	IVE	12-channel, ss-EPI, 6/8 PF	1.1 s
Spinal cord [75]	0.90 x 1.05 x 5	OVS	1-channel, ss-EPI, 60% PF	6.85 s
Brain stem [32]	0.90 x 0.90 x 5	IVE	12-channel, ss-EPI	1.1 s
Brain stem [28]	0.80 x 0.80 x 3	OVS	1-channel, ms-VD spiral	3.48 s

Figure 2.3 shows an example of phase-offset resulting from coherent motion of spins during diffusion encoding. Consider two spins at locations x_1 and x_2. Let time start at the start of the first diffusion gradient lobe and assume that at $t = 0$, phases of spins at x_1 and x_2 are 0. After the first gradient lobe (at $t = \delta$) phases accumulated by spins at x_1 and x_2 are ϕ_1 and ϕ_2, respectively:

$$\begin{aligned} \phi_1(\delta) &= Gx_1\delta \\ \phi_2(\delta) &= Gx_2\delta \end{aligned} \tag{2.24}$$

During the interval from the end of the first diffusion gradient lobe to the beginning of the second gradient lobe, both spins move coherently by α. Phases of spins originally at x_1

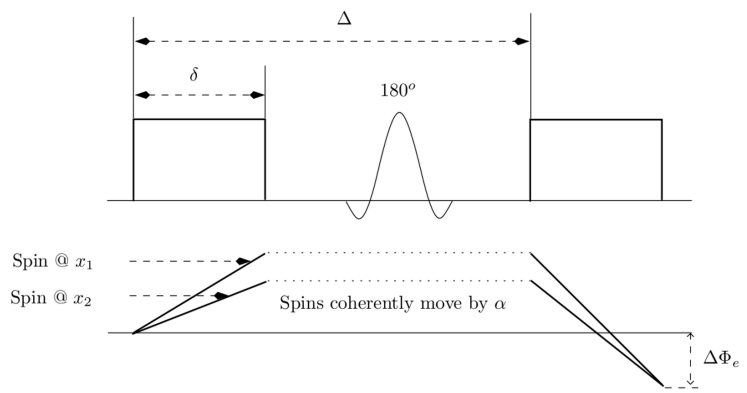

Figure 2.3: Motion-induced phase error in DWI.

and x_2 at the end of the second gradient lobe are

$$\begin{aligned} \phi_1(\Delta+\delta) &= Gx_1\delta - G(x_1+\alpha)\delta = -G\alpha\delta \\ \phi_2(\Delta+\delta) &= Gx_2\delta - G(x_2+\alpha)\delta = -G\alpha\delta \end{aligned} \tag{2.25}$$

Notice that for this simple example we assume spins are static during the intervals that the gradients are on. However, as long as the motion is coherent within a voxel, the resulting effect is still a constant phase-offset to the net magnetization of that voxel even if spins move when the gradients are on (as will be shown in the following analysis, which follows the work of Anderson and Gore [36]).

2.3.2 Rigid Body Motion-Induced Phase Errors: Analysis

To compensate for the above motion-induced phase errors (if any) in diffusion-weighted data, we first summarize the analysis done by Anderson and Gore [36] on the effects of these phase errors on the obtained k-space data and the reconstructed images.

The key assumption of the following analysis is that the diffusion-weighted data only suffer from rigid body motion, meaning any types of motion that can be decomposed into a translation and a rotation, without shearing or compressing the object. With this assumption, motions due to pulsation (CSF, blood), which usually lead to tissue deformation, are excluded and have to be handled separately.

For ease of quantifying the motion of an imaging object and its resulting effects on the acquired signal, two image space coordinate systems and two k-space coordinate systems are introduced [36]:

- (X, Y, Z): gradient coordinate system (G frame). X is the readout direction, Y is the phase encode direction, and Z is the slice select direction. The origin of this coordinate system is the point at which all encoding gradients are zero. The coordinate unit vectors are $\hat{X}, \hat{Y}, \hat{Z}$.

- (x, y, z): body center coordinate system (B frame). For an axial slice, x direction is the object's posterior/anterior axis, y direction is the right/left axis, and z direction is the inferior/superior axis. This coordinate system is attached to the imaging object and moves with the imaging object. The coordinate unit vectors are $\hat{x}, \hat{y}, \hat{z}$.

- (K_x, K_y, K_z): corresponding k-space coordinate system of the gradient coordinate system.

- (k_x, k_y, k_z): corresponding k-space coordinate system of the body center coordinate system.

Initially, G frame and B frame coincide. However, because of the object's motion during the application of diffusion gradient pulses, at readout, the B frame is detached from the G frame. For small motion, any change in position of the object, and hence the B frame, can be described as a translation followed by a rotation. At readout, consider an arbitrary point $\vec{r}$ in B frame; its corresponding position in G frame is

$$\vec{R}(t) = \vec{R_0}(t) + \vec{\theta}(t) \times \vec{r} \tag{2.26}$$

where $\vec{R_0}(t)$ and $\vec{\theta}$(t) represent the changes in B frame's origin and orientation as compared to G frame and

$$\begin{aligned} \vec{R_0}(t) &= X_0(t)\hat{X} + Y_0(t)\hat{Y} + Z_0(t)\hat{Z} \\ \vec{\theta}(t) &= \theta_x(t)\hat{x} + \theta_y(t)\hat{y} + \theta_z(t)\hat{z} \end{aligned} \tag{2.27}$$

where $X_0(t), Y_0(t), Z_0(t)$ are translations in $\hat{X}$, $\hat{Y}$, $\hat{Z}$ directions, respectively, and $\theta_x(t)$, $\theta_y(t)$, $\theta_z(t)$ are rotations around $\hat{X}$, $\hat{Y}$, $\hat{Z}$ axes, respectively.

Equation (2.26) is valid only if the rotations involved in the motion are small, which means [76]

$$\begin{aligned} \theta_x(t) &<< 1 \\ \theta_y(t) &<< 1 \\ \theta_z(t) &<< 1 \end{aligned} \tag{2.28}$$

for all t. In practice, this assumption is usually reasonable [36].

Because G frame and B frame are detached, transverse magnetization will have different spatial frequency representation in the two coordinate frames. Let $S(K_x, K_y, K_z)$ and $s(k_x, k_y, k_z)$ be the acquired signal in the (K_x, K_y, K_z) and (k_x, k_y, k_z) coordinates, respectively. Because the B frame moves with the object, the signal in the body frame is unaffected by motion and correctly represents the object. Meanwhile, the actual acquired signal, lying in the G frame, is affected by both translations and rotations. Translations and rotations result in a phase error in the acquired signal in the reciprocal coordinate of G frame. The corrupted signal has the form

$$S(K_x, K_y) = \int \rho(x, y) e^{j\varphi(x,y,z)} e^{j2\pi[K_x x + K_y y]} \mathrm{d}x\mathrm{d}y\mathrm{d}z \tag{2.29}$$

The phase error caused motion $\varphi(x, y, z)$ is

$$\varphi(x, y, z) = \gamma \int \vec{G}(t).\vec{R}(t) \tag{2.30}$$

where $\vec{G}(t) = G_x(t)\hat{X} + G_y(t)\hat{Y} + G_z(t)\hat{Z}$ is the diffusion gradient. Using Equations (2.26) and (2.27), the phase error in (2.30) can be rewritten as

$$\begin{aligned} \varphi(x, y, z) &= \gamma \int \vec{G}(t)\Big(\vec{R}_0(t) + \vec{\theta}(t) \times \vec{r}\Big)\mathrm{d}t \\ &= \gamma \int \vec{G}(t)\vec{R}_0(t)\mathrm{d}t + \left[\gamma \int \vec{G}(t) \times \vec{\theta}(t)\mathrm{d}t\right].\vec{r} \\ &= \Delta\varphi_x + \Delta\varphi_y + \Delta\varphi_z + \Delta\vec{k}.\vec{r} \end{aligned} \tag{2.31}$$

where

$$\begin{aligned}\Delta\varphi_x &= \gamma\int G_x(t)X_0(t)\mathrm{d}t\\ \Delta\varphi_y &= \gamma\int G_y(t)Y_0(t)\mathrm{d}t\\ \Delta\varphi_z &= \gamma\int G_z(t)Z_0(t)\mathrm{d}t\end{aligned} \tag{2.32}$$

$$\Delta\vec{k} = \gamma\int \vec{G}(t)\times\vec{\theta}(t)\mathrm{d}t \tag{2.33}$$

which means

$$\begin{aligned}\Delta k_x &= \gamma\int\Big[G_y(t)\theta_z(t) - G_z(t)\theta_y(t)\Big]\mathrm{d}t\\ \Delta k_y &= \gamma\int\Big[G_z(t)\theta_x(t) - G_x(t)\theta_z(t)\Big]\mathrm{d}t\\ \Delta k_z &= \gamma\int\Big[G_x(t)\theta_y(t) - G_y(t)\theta_x(t)\Big]\mathrm{d}t\end{aligned} \tag{2.34}$$

From Equations (2.32) and (2.34), the ϕ_x, ϕ_y, ϕ_z errors are due to translation while the $\Delta k_x, \Delta k_y, \Delta k_z$ errors are due to rotation.

The corrupted signal now can be written as

$$\begin{aligned}S(K_x, K_y) &= e^{j(\Delta\varphi_x+\Delta\varphi_y+\Delta\varphi_z)}\Big[\int e^{j2\pi\Delta k_z z}\mathrm{d}z\Big].\\ &\quad .\int\rho(x,y)e^{j2\pi[(K_x+\Delta k_x)x+(K_y+\Delta k_y)y]}\mathrm{d}x\mathrm{d}y\end{aligned}$$

The effect of through-plane k-space shift in a 2D acquisition is

$$\begin{aligned}A(\Delta k_z, \Delta z) &= \int_{-\Delta z/2}^{\Delta z/2} e^{j\Delta k_z z}\mathrm{d}z\\ &= \Delta z\mathrm{sinc}\Big(\tfrac{1}{2}\Delta k_z\Delta z\Big)\end{aligned} \tag{2.35}$$

where Δz is the slice thickness. So through-plane k-space shift leads to signal attenuation. The overall effect of rigid body motion on diffusion-weighted k-space data then is

$$\begin{aligned}S(K_x, K_y) &= A(\Delta k_z, \Delta z)e^{j(\Delta\varphi_x+\Delta\varphi_y+\Delta\varphi_z)}\int\rho(x,y)e^{j2\pi[(K_x+\Delta k_x)x+(K_y+\Delta k_y)y]}\mathrm{d}x\mathrm{d}y\\ &= A(\Delta k_z, \Delta z)e^{j(\Delta\varphi_x+\Delta\varphi_y+\Delta\varphi_z)}s(K_x+\Delta k_x, K_y+\Delta k_y)\end{aligned} \tag{2.36}$$

where $s(K_x, K_y)$ is the uncorrupted k-space data.

In conclusion, with small motions, a translation of the imaging object during diffusion encoding will lead to a phase-offset in k-space, and a rotation of the imaging object during diffusion encoding will lead to a k-space shift.

In image space, for a single-shot acquisition

$$\begin{aligned} \tilde{I}(x,y) &= \mathscr{F}\Big\{A(\Delta k_z,\Delta z)e^{j\Delta\varphi}s(K_x+\Delta k_x,K_y+\Delta k_y)\Big\} \\ &= A(\Delta k_z,\Delta z)e^{j[\Delta\varphi-2\pi(\Delta k_x x+\Delta k_y y)]}I(x,y) \end{aligned} \tag{2.37}$$

where $\tilde{I}(x,y)$ is the image affected by motion-induced phase errors, $I(x,y)$ is the true image, and $\Delta\varphi=\Delta\varphi_x+\Delta\varphi_y+\Delta\varphi_z$. Therefore, a translation leads to a phase offset in image space and a rotation leads to a phase ramp in image space.

Motion-Induced Phase Errors and Single-Shot DWI

Single-shot DWI is the acquisition technique in which the whole k-space data is obtained with only one application of the diffusion encoding gradients. A motion-affected diffusion-weighted image from single-shot DWI takes the form of Equation (2.37). In practice, only the magnitude of the diffusion-weighted images is used for deriving the interested DTI metrics. Therefore, from Equation (2.37), single-shot DWI will only suffer from signal attenuation due to through-plane k-space shift, $A(\Delta k_z,\Delta z)$.

Motion-Induced Phase Errors and Multishot DWI

When reduced readout duration is necessary such as in the case of severe magnetic susceptibility or eddy currents, multishot acquisition is used. For multishot DWI, different shots (parts) of k-space data are acquired after separate application of diffusion encodings during which patient motions may change. Therefore, each shot of k-space data suffers from distinct motion-induced phase errors. Let $k_x^{(l)},k_y^{(l)}$ be the k-space trajectory of shot l in an N_l-shot DWI. The corrupted k-space data of shot l is

$$S(k_x^{(l)},k_y^{(l)})=A(\Delta k_z^{(l)},\Delta z)e^{j\Delta\varphi^{(l)}}s(k_x^{(l)}+\Delta k_x^{(l)},k_y^{(l)}+\Delta k_y^{(l)}) \tag{2.38}$$

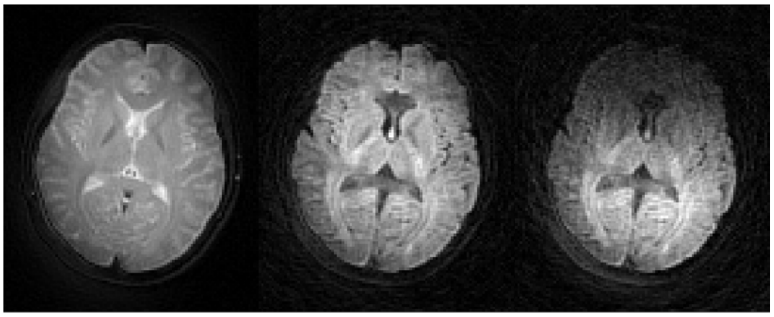

Figure 2.4: Motion-induced phase errors in single-shot and multishot DW images: The left image is the $b = 0$ image, the center image is the single-shot DW image, the right image is the multishot DW image. Multishot DW image is heavily corrupted by motion-induced phase errors while single-shot DW image is of low resolution and distorted by the long readout duration.

The reconstructed image from the received signal of shot l with motion errors then is

$$\begin{aligned}
\tilde{I}^{(l)}(x,y) &= \mathscr{F}\left\{ A(\Delta k_z^l, \Delta z) e^{j\Delta\varphi^{(l)}} s\left(k_x^{(l)} - \Delta k_x^{(l)}, k_y^{(l)} - \Delta k_y^{(l)}\right) \right\} \\
&= A(\Delta k_z^{(l)}, \Delta z) e^{j\left[\Delta\varphi^{(l)} + 2\pi\left(\Delta k_x^{(l)} x + \Delta k_y^{(l)} y\right)\right]} \mathscr{F}\left\{ s(k_x^{(l)}, k_y^{(l)}) \right\} \\
&= A(\Delta k_z^{(l)}, \Delta z) e^{j\left[\Delta\varphi^{(l)} + 2\pi\left(\Delta k_x^{(l)} x + \Delta k_y^{(l)} y\right)\right]} I^{(l)}(x,y)
\end{aligned} \tag{2.39}$$

$\mathscr{F}\{.\}$ is the Fourier transform operator, and $\tilde{I}^{(l)}(x,y)$ and $I^{(l)}(x,y)$ are the corrupted and ideal uncorrupted reconstructed images from shot l, respectively. The corrupted image reconstructed from data of all shots is the complex summation of corrupted images reconstructed from data of individual shots

$$\tilde{I}(x,y) = \sum_{l=1}^{N_l} A(\Delta k_z^{(l)}, \Delta z) e^{j\left[\Delta\varphi^{(l)} + 2\pi\left(\Delta k_x^{(l)} x + \Delta k_y^{(l)} y\right)\right]} I^{(l)}(x,y) \tag{2.40}$$

From Equation (2.40), we can see that even the magnitudes of diffusion-weighted images of multishot DWI are corrupted by both motion-induced phase errors and signal attenuation.

Figure 2.4 shows the effect of motion-induced phase error on single-shot and multishot DW images. Motion-induced phase error renders the multishot image useless. However, the single-shot image is of low resolution and distorted due to strong T2 blurring, and heavy magnetic susceptibility resulting from prolonged readout shows the effect of motion-induced

phase error on single-shot and multishot DW images. Motion-induced phase error renders the multishot image useless. However, the single-shot image is of low resolution and distorted due to strong T2 blurring and heavy magnetic susceptibility resulting from prolonged readout duration.

2.3.3 Existing Methods for Motion-Induced Phase Error Correction

Two-Dimensional Algorithms

Several methods exist in the literature to correct for 2D motion-induced phase artifacts in DWI. These methods can be grouped into three categories: correction in image-space, correction in k-space, and correction combined with image reconstruction.

The procedure for correction of motion artifacts includes estimation of the errors and application of the corresponding error compensation. Estimation of motion errors can be done using the low-resolution image, which is either acquired separately prior to the diffusion-weighted image or reconstructed from the center part of a variable density readout trajectory. Having estimated the phase errors for each shot, the correction then is carried out in image-space, k-space (only in the case of rigid body motion), or during image reconstruction. In the following three sections, three of the most common methods of motion-induced phase error correction are discussed.

Image-based method: direct phase subtraction. Direct phase subtraction methods perform phase error compensation in image-space. With the assumption that phase errors are smooth, the estimated low-resolution phase error of each shot is removed from the high-resolution aliased image reconstructed from undersampled k-space data of that same shot. This correction process can be iterated for a better result. If the phase error correction is complete, the final image created by adding together all high-resolution aliased images from all shots will be the desired, artifact-free image [41].

The direct phase subtraction method is commonly used because of its simplicity [37, 38, 41]. However, with multishot k-space trajectories, each shot usually undersamples k-space. Therefore, high-resolution images of individual shots are aliased and contain aliased phase

errors. The assumption that phase errors are smooth—or equivalently, the assumption that there are no significant differences between errors experienced by the low-resolution and high-resolution images—is invalid. Hence, motion artifacts cannot be completely corrected using direct phase subtraction [43]. The failure of the direct phase subtraction method results from the fact that residual aliased high-resolution phases from individual shots are not addressed. This observation implies that to avoid the incomplete motion correction due to aliased errors, errors should be removed before (in k-space) or during the image reconstruction process [43].

K-*space based methods*. Atkinson et al. introduced a very simple k-space-based motion-induced phase error correction method in [42]. In their method, the errors including k-space shifts $(\Delta k_x^{(l)}, \Delta k_y^{(l)})$ and constant phase-offsets $(\Delta\varphi^{(l)})$ in Equation (2.38) are estimated from the shifts and phases of the peak magnitude k-space data point. The precision of this estimation, however, depends on the resolution of the k-space data. With careful post-processing, a precision of up to a half of the k-space sampling distance can be achieved [42]. Motion-induced phase errors due to pulsation were not taken care of in [42] and the resulting images still had significant artifacts.

Another k-space based motion artifact correction method was introduced by Li et al. in [45]. The common assumption in MRI is that magnetization signals in each imaging voxel are constant; the magnetization signal at each location in the imaging slice $M(x, y)$ is

$$M(x,y) = \sum_{u=-\frac{N}{2}}^{\frac{N}{2}} \sum_{v=-\frac{N}{2}}^{\frac{N}{2}} m_{uv} p\left(\frac{x-u\Delta x}{\Delta x}, \frac{y-v\Delta y}{\Delta y}\right) \tag{2.41}$$

where $N \times N$ is the in-plane imaging voxel matrix size, m_{uv} is the magnetization signal at voxel (u, v), $(\Delta x, \Delta y)$ is the voxel size, and $p(\alpha, \beta)$ is the 2D rectangular function

$$p(\alpha,\beta) = \begin{cases} 1 & \text{if } -\frac{1}{2} \le \alpha, \beta \le \frac{1}{2} \\ 0 & \text{else.} \end{cases} \tag{2.42}$$

The relationship between magnetization signal and acquired k-space data $S(k_x, k_y)$ is

$$\begin{aligned} S(k_x, k_y) &= \mathscr{F}^{-1}\Big\{ M(x,y) \Big\} \\ &= \Delta x \Delta y \text{sinc}\Big(k_x \Delta x, k_y \Delta y\Big) \sum_{u=-\frac{N}{2}}^{\frac{N}{2}} \sum_{v=-\frac{N}{2}}^{\frac{N}{2}} m_{uv} e^{-j2\pi(uk_x\Delta x + vk_y \Delta y)} \end{aligned} \tag{2.43}$$

The k-space based method proposed by Li et al. assumes that acquired k-space data can be approximated by a 2-D sinc [45]. From Equation (2.43), this assumption means

$$\sum_{u=-\frac{N}{2}}^{\frac{N}{2}} \sum_{v=-\frac{N}{2}}^{\frac{N}{2}} m_{uv} e^{-j2\pi(uk_x\Delta x + vk_y \Delta y)} = A(k_x \Delta x, k_y \Delta y)$$

where $A(k_x\Delta x, k_y \Delta y)$ is the discrete time Fourier transform (DTFT) of m_{uv} and has to be a constant, which implies $m_{uv} = \delta(u, v)$. This is not a reasonable model for the spatial frequency information of the object.

Li et al. also assumed that the motion-induced artifacts result only from rigid-body motion. With rigid body motion during diffusion encoding, the resulting errors are k-space shifts and phase-offsets in acquired data. Using a self-navigated k-space trajectory, the oversampled portions of k-space data for individual shots are extracted and least-square fitted to a 2-D shifted sinc. The displacements from the origin of the resulting best fitted sinc give the estimations of k-space shifts. Phase offsets are estimated as the phases of the peak signal in acquired k-space data.

Although the k-space method introduced by Li et al. overcomes the problem of aliased phase errors, its performance is not good. The reason is that the assumption of approximately constant magnetization signals in the whole imaging slice is usually invalid.

Integrated motion-induced phase error and SENSE reconstruction. Recently, a phase correction algorithm was introduced that combined correction with sensitivity encoding (SENSE) reconstruction for multicoil, multishot diffusion weighted imaging [43]. The method performs motion correction during image reconstruction by incorporating the phase errors into the image encoding function. In matrix form, with the incorporated phase errors, the

k-space data acquired with a single-coil multishot sequence are

$$d = Em \tag{2.44}$$

where d is a column vector of k-space data, E is the encoding matrix which combines Fourier encoding and motion-induced phase error encoding, and m is a column vector of the reconstructed artifact-free image. Specifically, d, m, and E can be expressed as [43]

$$d = \begin{bmatrix} d(k_{1,1})\ d(k_{2,1})\ \ldots\ d(k_{n_k,1})\ \ldots\ d(k_{k,s})\ \ldots\ d(k_{n_k,n_s}) \end{bmatrix}^T \tag{2.45}$$

$$m = \begin{bmatrix} m(r_1)\ m(r_2)\ \ldots\ m(r_{N^2}) \end{bmatrix}^T \tag{2.46}$$

$$E = \begin{bmatrix} (F_1P_1)^T \mid (F_2P_2)^T \mid \ldots \mid (F_{n_s}P_{n_s})^T \end{bmatrix}^T \tag{2.47}$$

where F_s is the Fourier encoding matrix of shot s with the form

$$F_s = \begin{bmatrix} e^{-j2\pi k_{1,s}r_1} & e^{-j2\pi k_{1,s}r_2} & \ldots & e^{-j2\pi k_{1,s}r_{N^2}} \\ e^{-j2\pi k_{2,s}r_1} & e^{-j2\pi k_{2,s}r_2} & \ldots & e^{-j2\pi k_{2,s}r_{N^2}} \\ \vdots & \vdots & e^{-j2\pi k_{k,s}r_\rho} & \vdots \\ e^{-j2\pi k_{n_k,s}r_1} & e^{-j2\pi k_{n_k,s}r_2} & \ldots & e^{-j2\pi k_{n_k,s}r_{N^2}} \end{bmatrix} \tag{2.48}$$

and P_s is a diagonal matrix of motion-induced phase errors caused by shot s:

$$P_s = \begin{bmatrix} e^{j\varphi_s(r_1)} & 0 & \ldots & 0 \\ 0 & e^{j\varphi_s(r_2)} & 0 & 0 \\ \vdots & \vdots & e^{j\varphi_s(r_\rho)} & \vdots \\ 0 & 0 & \ldots & e^{j\varphi_s(r_{N^2})} \end{bmatrix} \tag{2.49}$$

In all of the above equations, $k_{k,s}$ is the k^{th} sampling point of the s^{th} shot, r_ρ is the location of the ρ^{th} pixel of the reconstructed image, and $\varphi_s(r_\rho)$ is the phase error caused by motion during the acquisition of shot s to pixel at location r_ρ.

If the phase errors caused by individual shots, P_s's, are known, the encoding matrix E is

known and the least squares estimation of m gives

$$E^H E m = E^H d \tag{2.50}$$

Because of the large size of E, the conjugate-gradient method is used to solve Equation (2.50). A fast version of the conjugate-gradient method is also implemented in [43]. In the case of parallel imaging, SENSE reconstruction can be easily incorporated into the current problem by properly redefining E. Let c_γ be the coil sensitivity profile of the γ^{th} coil, $\varphi_{s,\gamma}(r_\rho)$ be the phase error suffered by data from coil γ during shot s at location ρ in the image, and define the complex coil sensitivity matrix of coil γ, shot s, $S_{s,\gamma}$, as

$$S_{s,\gamma} = \begin{bmatrix} c_\gamma(r_1)e^{j\varphi_{s,\gamma}(r_1)} & 0 & \dots & 0 \\ 0 & c_\gamma(r_2)e^{j\varphi_{s,\gamma}(r_2)} & 0 & 0 \\ \vdots & \vdots & c_\gamma(r_\rho)e^{j\varphi_{s,\gamma}(r_\rho)} & \vdots \\ 0 & 0 & \dots & c_\gamma(r_{N^2})e^{j\varphi_{s,\gamma}(r_{N^2})} \end{bmatrix} \tag{2.51}$$

The necessary redefinition of E for both SENSE reconstruction and phase error correction is

$$E = \left[(F_1 S_{1,1})^T \mid (F_1 S_{2,1})^T \mid \dots \mid (F_{n_s} S_{n_s,1})^T \mid \dots \mid (F_{n_s} S_{n_s,n_c})^T \right]^T \tag{2.52}$$

And again, the conjugate gradient method is used to reconstruct the image m.

If the phase errors at each location in the image are known, simultaneous phase correction and SENSE reconstruction can be used to correct for any type of phase error, linear or nonlinear. However, because of the iterative algorithm and the large size of the E matrix, the computational requirement is an issue.

Three-Dimensional Algorithms

In contrast to the 2D case, few algorithms exist for 3D motion-induced phase error correction. The first algorithm for correction of 3D motion-induced phase errors was proposed in [65] as the extensions of 2D SNAILS and 2D conjugate phase methods. Phase errors in image space were estimated from the navigators and either subtracted from the phase of

the reconstructed images [65] or used as an additional term in the encoding matrix of the iterative reconstruction [65]. Similar to the 2D case, shot-by-shot direct subtraction of the phase errors in image space is fast but the corrected image can suffer from residual phase errors when images reconstructed from individual shots are aliased. Incorporating the phase error correction with iterative reconstruction can give complete error compensation but at the cost of long reconstruction time from prohibitively large matrix sizes, especially for high resolution 3D acquisitions. A simpler method was used in [68] combined with cardiac-gating to correct for motion-induced phase errors. The method utilized the k-space data point with maximum magnitude for estimating the shift and the phase of the 3D k-space center used in correcting the motion-induced phase error caused by rigid body motion. The performance of this method depends on the k-space resolution and 3D k-space coverage during each diffusion encoding. In another study, Frank et al. proposed to use 2D direct phase subtraction for each z-encoding line (k_z) and each shot individually [71]. Since the correction is in the (x, y, k_z) domain, it is necessary to preserve the phase information that related to z-encoding to transform the corrected data back to the image domain (x, y, z). Therefore, reference to the phase of $b = 0$ images was used. Besides the problem of aliased phase errors that are common to any direct phase subtraction methods [41], the motion-induced phase errors in z-encoding direction may cause shifts in k_z that lead to incorrect alignment between the actual k_z of diffusion-weighted data and the nominal k_z of non-diffusion-weighted data and therefore in correct phase reference.

2.4 Magnetic Susceptibility in DTI

It can be said that magnetic susceptibility artifacts and motion-induced phase errors are two competing problems in DTI in the sense that minimizing one source of artifact would lead to increases of the other artifact. In this section, an introduction to magnetic susceptibility artifacts in DTI and in MRI in general is given. Existing methods for suppressing magnetic susceptibility artifacts are also reviewed.

Magnetic susceptibility artifacts refers to the degradation of image quality as a result of the disruption of the B0 field homogeneity when the imaging object possesses spatially de-

pendent magnetic susceptibility. The change in B0 field leads to the change in the resonance frequencies of the imaging spins

$$\tilde{\omega}(\vec{r}) = \omega_0 + \gamma \vec{G}(\vec{r}) \cdot \vec{r} + \omega_s(\vec{r}) \tag{2.53}$$

where ω_0 is the Lamor frequency, $\vec{G}(\vec{r})$ is the spatial encoding gradient, and $\omega_s(\vec{r})$ is the frequency offset due to the B0 field change induced by magnetic susceptibility.

After demodulation, the received signal corrupted by magnetic susceptibility is

$$\begin{gathered} y(t_m) = \int f(\vec{r}) \exp\left(j\omega_s(\vec{r})t_m - j2\pi\vec{k}(t_m) \cdot \vec{r}\right) \mathrm{d}\vec{r} \\ m = 0, 1, \cdots, M-1 \end{gathered} \tag{2.54}$$

where $f(\vec{r})$ is the imaging object, and $\vec{k}(t)$ is the k-space trajectory defined as

$$\vec{k}(t) = \frac{\gamma}{2\pi} \int_0^t \vec{G}(\vec{r}, t')\mathrm{d}t'$$

From Equation (2.54), attempts to reconstruct the imaging object by performing inverse Fourier transform of the received signal would lead to incorrect results. Notice also that the longer the acquisition time (the longer the t_m), the worse impact of susceptibility.

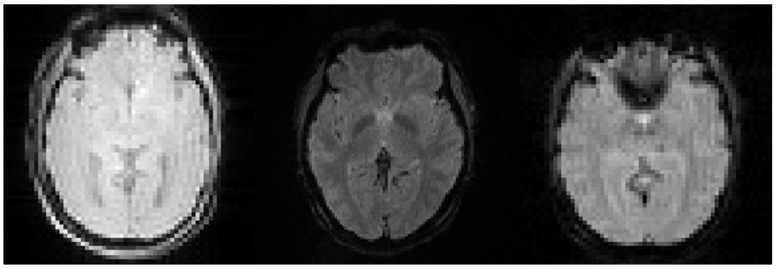

Figure 2.5: Undistorted, reference image (left). Magnetic susceptibility leads to geometric distortion in EPI (center) and blurring and signal loss in spiral imaging (right).

Depending on the type of k-space trajectory used, magnetic susceptibility artifacts manifest themselves differently in the uncorrected images. Figure 2.5 shows the magnetic susceptibility artifacts in images acquired with echo planar imaging (EPI) trajectory and spiral trajectory. The EPI image shows geometric distortion while the spiral image shows blurriness

and signal loss.

Many algorithms have been proposed to correct for magnetic susceptibility artifacts. If Cartesian trajectories are used, a common and effective way to correct for the geometric distortions is the pixel-shift method [77]. In this method, a map of field inhomogeneity-induced pixel shift is derived from a map of off-resonance frequencies and then applied to the distorted image.

When non-Cartesian trajectories are used, all the existing correction methods utilize the signal equation in (2.54) together with a field map measurement to compensate for the effects. In the following section the commonly used methods for non-Cartesian field inhomogeneity correction are reviewed.

2.4.1 Conjugate Phase Reconstruction

Conjugate phase reconstruction (CP) method for field inhomogeneity correction was first introduced by Maeda et al. [78]. Under linear and shift invariant assumption, an estimate of the field corrected image in Equation (2.54) can be expressed as

$$\hat{f}(\vec{r}) = \sum y(t_m) \exp\Big(j2\pi\vec{k}(t_m)\cdot\vec{r} - \omega_s(\vec{r})\Big) w_m \tag{2.55}$$

where w_m is a real-valued weighting factor. From Equation (2.55), the CP method seeks to compensate for the phase accrual at each time point due to the off-resonance. The computational time for the above reconstruction is $O(n_d N^2)$, where n_d is the number of k-space data points, and N is the image size.

Noll et al. in [79, 80] relaxed the spatial shift invariant assumption in [78] and proposed a computational efficient realization of the CP method. With a general reconstruction algorithm, the field corrected reconstructed image of signal equation (2.54) can be expressed as

$$\hat{f}(\vec{r}) = \sum_m y(t_m) \exp\Big(j\omega_s(\vec{r}t_m)\Big) C(m,\vec{r}) \tag{2.56}$$

where $C(m,\vec{r})$ is some complex weighting factor depending on the reconstruction algorithm of choice.

With the assumption that the field inhomogeneity is smooth, an efficient field corrected reconstruction algorithm was proposed by segmenting the acquisition window into $L+1$ intervals of length τ over which the phase accumulation due to off-resonance can be regarded as constant. The reconstruction equation then becomes

$$\hat{f}(\vec{r}) = \sum_{l=0}^{L} \exp(j\omega_s(r)l\tau)\left[\sum_m y(t_m)a(t_m - l\tau)C(m,\vec{r})\right] \tag{2.57}$$

where $a(t)$ is a bounded windowing function.

From Equation (2.57), any fast reconstruction algorithm that is available to reconstruct data without field inhomogeneity effects can be used to reconstruct individual segments; therefore, this CP algorithm can be sped up significantly as compared to the method in [78].

Another similar idea was proposed by Noll et al. in [80], but instead of segmenting in time domain, segmenting in frequency was performed. The off-resonance frequencies are divided into a number of bins with one frequency representing each bin. K-space data are then modulated to the bin frequencies and separately reconstructed. The final field-corrected image is constructed pixel by pixel by noting the bin that each pixel belongs to from the frequency off-set map and assigning the value of that pixel to the value of the corresponding pixel in the image reconstructed from k-space data modulated with the bin frequency.

2.4.2 Iterative Reconstruction with Field Inhomogeneity Correction

The key assumption for the efficient CP algorithm is that the field inhomogeneity has to be sufficiently smooth, meaning

$$\left(\omega_s(\vec{r}) - \omega_s(\vec{r'})\right)t_m << \frac{\pi}{2} \tag{2.58}$$

However, regions of the brain near air/tissue interfaces, such as those above the frontal sinuses, have field distributions that violate this assumption. Sutton et al. overcome this limitation by posing the problem as a statistical estimation inverse problem and solving it iteratively [81]. Speeding up of the algorithm is achieved by combining nonuniform fast Fourier transform (NUFFT) and the time-segmentation method. However, unlike the time-

segmentation method introduced in [79], the method in [81] proposed to use a temporal interpolation method that is optimal in the min-max sense of minimizing worst-case interpolation error and hence can capture the oscillatory nature of phase modulation caused by off-resonance effects.

Integrating the field inhomogeneity correction into iterative reconstruction procedures allows the consideration/trade-off of field-inhomogeneity correction, data fitting, noise, and *a priori* information together.

2.5 Eddy Currents

Eddy currents are the electric currents induced in the gradient coils when there are changes in the magnetic field. These eddy currents give rise to undesired time-varying magnetic field that can cause image degradation, especially when this field persists through the image encoding period.

Even though each on and off field gradient transition produces eddy currents to some degree, the magnitude of the eddy-current-induced field is proportional to the magnitude of the rate of changes in gradient amplitude (slew rate). Therefore, diffusion-weighted imaging is highly sensitive to eddy current effect due to the switching on/off of high amplitude diffusion gradients.

During the preparation period, eddy-current-induced gradients can cause additional phase accumulation. If the phase gradient per pixel is small so that no signal loss occurs, the effect of eddy currents during the sequence preparation period is just a shot-independent and spatially dependent phase across the acquired image and can be ignored since magnitude images will be used for measuring diffusion metrics. During the spatial encoding period, eddy-current-induced field behaves like an additional encoding gradient and, therefore, causes k-space trajectory distortion that leads to image distortion or image blurriness. Examples of eddy current effects are shown in Figure 2.6.

There have been many methods for compensating or mitigating eddy currents including

- hardware: shielded gradient coils

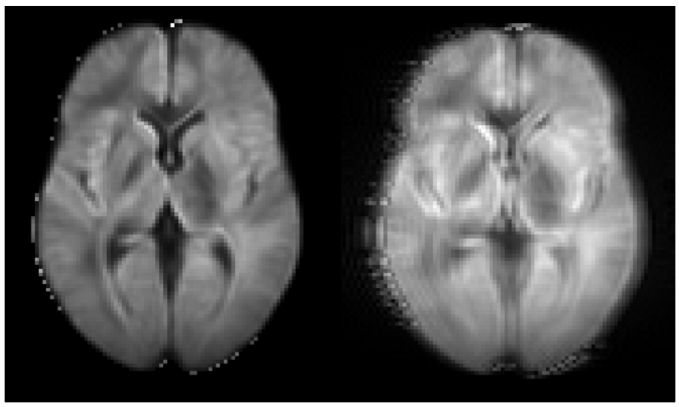

Figure 2.6: Eddy current leads to blurring and image distortion (right) as compared to the reference image (left).

- pulse sequence design: waveform pre-emphasis, splitting long gradient pulses into shorter duration bipolar gradients (DWI), reducing gradient amplitudes
- post-processing: use reference scans for estimation of k-space shifts and phase errors and perform the corresponding correction

In this thesis we only review a specific acquisition-based eddy-current compensation method by splitting long gradient pulses into shorter duration gradients with application to DWI [50, 82, 83]. The motivation for this class of eddy-current compensation method comes from the fact that on/off and off/on gradient transitions produce equal and opposite eddy currents. Therefore, the shorter the distance between on/off and off/on transitions, the less the residual eddy-current-induced magnetic field [50].

When bipolar diffusion preparation is used, the splitting can be on both gradients, which leads to twice refocus spin echo (TRSE) [50] or modified TRSE [83]. The splitting can be only on the last gradient, which leads to eddy-current compensation with single refocused RF pulse [82].

The original TRSE proposed by Reese et al. chose the splitting points to completely cancel eddy currents with a given time constant. Figure 2.7 shows the basic of a TRSE sequence

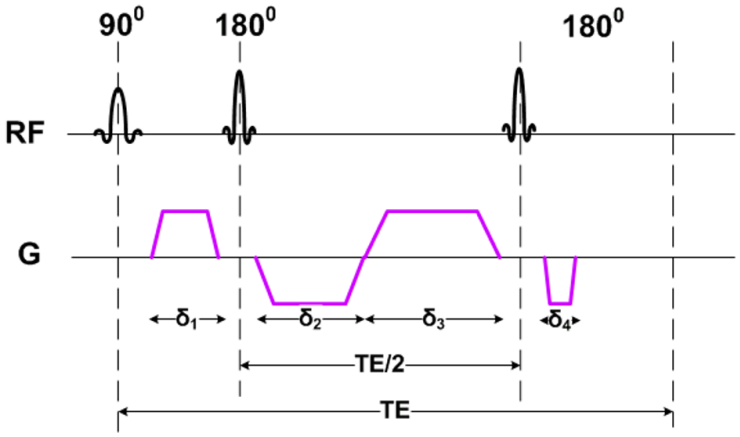

Figure 2.7: Twice refocused spin echo sequence for eddy current compensation.

proposed in [50]. From Figure 2.7, the conditions on the gradient durations are

$$\begin{aligned} \delta_1 + \delta_2 &= \delta_3 + \delta_4 \\ \delta_2 + \delta_3 &= \frac{TE}{2} - d_{180} \\ \delta_1 + \delta_4 &= \frac{TE}{2} - d_{180} - t_{prep} \end{aligned} \tag{2.59}$$

where t_{prep} is the preparation time after the excitation pulse, and d_{180} is the duration of the refocusing pulse and accompanied crushers. From Equation (2.59),

$$\begin{aligned} \delta_2 &= \frac{TE}{2} - d_{180} - \frac{t_{prep}}{2} - \delta_1 \\ \delta_3 &= \frac{t_{prep}}{2} - \delta_1 \\ \delta_4 &= \frac{TE}{2} - d_{180} - t_{prep} - \delta_1 \end{aligned} \tag{2.60}$$

Neglecting gradient ramp times and assuming exponentially decayed eddy currents with a known time constant of $\tau = 1/\lambda$, the condition for complete cancellation of the cumulative eddy currents after the last gradient pulse has been played out is

$$\begin{aligned} 1 - e^{\lambda\delta_1} - e^{\lambda(\delta_1+d_{180})} + 2e^{\lambda(\delta_1+\delta_2)+d_{180}} - e^{\lambda(\delta_1+\delta_2+\delta_3)+d_{180}} \\ - e^{\lambda(\delta_1+\delta_2+\delta_3)+2d_{180})} + e^{\lambda(\delta_1+\delta_2+\delta_3)+\delta_4+2d_{180})} = 0 \end{aligned} \tag{2.61}$$

Replacing Equation (2.60) into Equation (2.61), with some manipulation, we have

$$\delta_1 = \frac{1}{\lambda} \ln \left[\frac{1 + 2e^{\lambda(\frac{TE}{2} - \frac{t_{prep}}{2})} + e^{\lambda(TE - t_{prep})}}{1 + e^{\lambda d_{180}} + e^{\lambda \frac{TE}{2}} + e^{\lambda(\frac{TE}{2} + d_{180})}} \right] \tag{2.62}$$

Assume that all RF pulses and preparation gradients have negligible duration, the resulting δ_1 is valid only if $\delta_1 < \frac{TE}{2}$. From Equation (2.62), this condition means

$$TE > \frac{2}{\lambda} \ln(1 + \sqrt{5}) \tag{2.63}$$

Furthermore, to maintain the same b-value as that of the noncompensated sequence, the split gradients must satisfy $\delta_1 + \delta_2 = \delta_3 + \delta_4 = \delta$, and the minimum echo time must satisfy $TE > 2\delta + 2d_{180} + t_{prep}$. The condition on TE then becomes

$$TE > \max \left\{ \frac{2}{\lambda} \ln(1 + \sqrt{5}), 2\delta + 2d_{180} + t_{prep} \right\} \tag{2.64}$$

Therefore, even with the assumption of single-time-constant eddy currents, the method proposed by Reese et al. cannot cancel eddy currents with long time constants (> 100 ms) due to the long TE required.

Aiming at reducing the echo time for EPI acquisition with long preparation time (including long excitation for reduced FOV imaging and long readout time for high resolution), Finsterbusch proposed an eddy current compensation method using only one refocusing pulse as shown in Figure 2.8 [82]. Instead of splitting both diffusion gradients, only the last diffusion gradient was split in [82]. Since only one refocusing pulse is used, the proposed scheme not only is less sensitive to B1 field inhomogeneity and flip angle imperfection, but also deposits less RF energy (less SAR) than the TRSE, which is important especially at high field. From [82], the splitting for cancellation of a time constant λ is

$$\delta_2 = \frac{1}{\lambda} \ln \frac{e^{\lambda(\Delta + \delta)}(1 + e^{\lambda d_1 80})}{e^{\lambda\delta} + e^{\lambda\Delta} + e^{\lambda(\Delta + \delta + d_{180})} - 1} \tag{2.65}$$

with $0 < \delta_2 < \delta$ for $0 < \lambda < \infty$.

Regarding the increase in TE for spiral acquisition, the amount of increase in TE for this

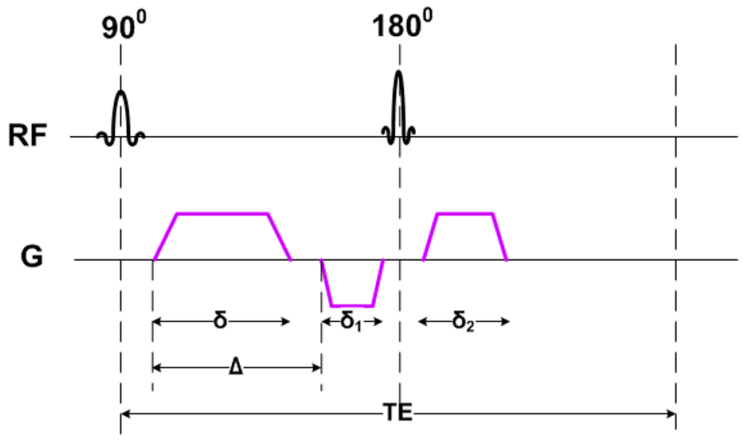

Figure 2.8: Single refocused spin echo sequence for eddy current compensation.

method is $2\delta_1$ regardless of the preparation duration.

Recently, Finsterbusch modified the TRSE sequence proposed by Reese et al. to allow the compensation of eddy currents with two known time constants [83]. Since the distances between the two diffusion pulses to the beginning of the readout are different, it is reasonable that the readout is affected differently by eddy currents generated by the two diffusion pulses. More precisely, the readout is affected more by the long time constant (cancelled by the first splitting) of the first diffusion pulse and by the short time constant (cancelled by the second splitting) of the second diffusion pulse. To cancel the eddy-current effects with a given time constant, the second gradient pulse of each group (meaning either δ_2 or δ_4), denoted collectively as δ_{last}, is chosen according to [83]

$$\delta_{last} = \frac{1}{\lambda} \ln \frac{e^{\lambda\delta}(1 + e^{\lambda d_{180}})}{1 + e^{\lambda(\delta + d_{180})}} \tag{2.66}$$

The modified TRSE suffers from an increase in the minimum TE by $\delta - (\delta_2 + \delta_3)$ which is always positive for effective cancellation of eddy currents.

2.6 Conclusion

We have so far reviewed the basics of DWI, existing acquisition strategies for high resolution DTI as well as common artifacts in DWI and corresponding correction algorithms. The rest of the thesis focuses on the proposed methods for achieving high-resolution, limited artifact diffusion tensor imaging, starting with introducing a time-efficient algorithm for correcting rigid-body-motion-induced phase error in DTI.

CHAPTER 3

MOTION-INDUCED PHASE ERROR CORRECTION FOR 2D DIFFUSION IMAGING

3.1 K-Space and Image Space Correction Technique for Motion-Induced Phase Error

In the following section, we introduce a new algorithm for motion-induced phase error correction in multishot DWI named k-space and image space correction technique (KICT) for motion-induced phase errors. This work is summarized from our published work in [47]. KICT is a noniterative time-efficient method for correction of rigid body motion artifacts. In combination with a cardiac-gated data acquisition, KICT is expected to perform comparably to or or better than any nonlinear correction method, with much reduced computational requirements. Because of the ability to preserve phases of imaging object and receiver coils, KICT can be used along with any parallel reconstruction algorithm.

Using Equation (2.38) KICT performs motion-induced phase error correction by shifting the k-space trajectory of each shot $(k_x^{(l)}, k_y^{(l)})$ by the corresponding shifts $(\Delta k_x^{(l)}, \Delta k_y^{(l)})$ and multiplying the received signal with a global phase factor. The global phase factor is the offset of the linear phase in Equation (2.40) while the shifts in k-space are proportional to the slopes of the linear phase in Equation (2.40). Therefore, if the linear phase errors in the image space are known, their offset and slopes can be estimated and used to correct for the errors in k-space data. As will be shown shortly, this additional phase information is derived from low-resolution self-navigated data. The correction procedure in KICT involves shifting of the k-space trajectory. Therefore, it is possible that the resulting k-space is locally undersampled. However, if there is flexibility in data acquisition time, an improvement of image quality can be obtained for large k-space shifts by acquiring the same set of data multiple times [42].

In our method, k-space data is acquired using a multishot variable density (VD) spiral readout trajectory that oversamples the center of k-space. For each shot, nonaliased low-resolution images are reconstructed from the center part of k-space data. Phases of these low-resolution images contain the low-resolution phase of the imaging object, the receiver coil, and low-resolution phase errors due to motion during diffusion encoding. For now we will consider the single-coil case and lump the object and coil phases. Let Φ_0 be the low-resolution phase of the imaging object and $\Delta\phi_e^{(l)}$ be the low-resolution phase error of the l^{th} shot. The phase of the l^{th} reconstructed low-resolution image is

$$\Phi^{(l)} = \Phi_0 + \Delta\phi_e^{(l)} \tag{3.1}$$

and the phase errors experienced by each shot can be estimated by

$$\Delta\phi_e^{(l)} = \Phi^{(l)} - \Phi_0 \tag{3.2}$$

In DWI studies, a reference image with $b = 0$ (without diffusion encoding) is acquired along with diffusion-encoded images. With the assumption that phase errors due to imaging gradients are much smaller than those due to diffusion gradients and, therefore, can be ignored, phases of $b = 0$ images reconstructed from individual shots do not contain motion-induced phase errors. In addition, the spatial phase distribution due to coil effects is consistent between $b = 0$ images and $b \neq 0$ images. Therefore, the phase error experienced by each shot can be determined by subtracting the phase of the $b \neq 0$ image of a shot from the phase of the $b = 0$ image of the same shot.

Figure 3.1 describes this phase error estimation procedure. Since the phase, not the magnitude, of the $b = 0$ image is referenced, as long as there is no spatial distribution of diffusion anisotropy within a voxel, meaning diffusion properties within a voxel are homogeneous, then there will be no net phase difference between the images without diffusion encoding and with diffusion encoding. Homogeneity of diffusion properties within a voxel is a standard and fundamental assumption used in many diffusion imaging methods.

From Equation (2.40), phase errors experienced by reconstructed images from each shot

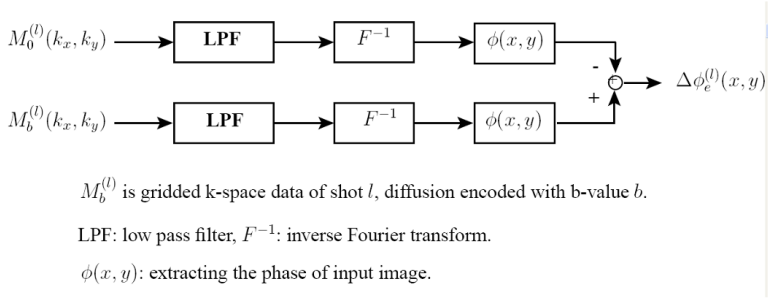

Figure 3.1: Phase error estimation for shot l.

$\Delta\phi_e^{(l)}$ are linear under the assumption of rigid body motion

$$\Delta\phi_e^{(l)} = \Delta\varphi^{(l)} + 2\pi(\Delta k_x^{(l)} x + \Delta k_y^{(l)} y) \tag{3.3}$$

To estimate $\Delta\varphi^{(l)}, \Delta k_x^{(l)}, \Delta k_y^{(l)}$, we can perform a least squares fit of the phase errors, $\Delta\phi_e^{(l)}$, to 2D planes. However, because all the phases contain 2π-wraps, $\Delta\phi_e^{(l)}$'s have to be unwrapped before inputting to least squares fitting routine. Although 2D phase unwrapping is possible, the procedure is ambiguous and error-prone. Therefore, in our method we reduce the 2D plane unwrapping and 2D least squares fitting problems to multiple 1D phase unwrapping and 1D least squares fitting problems. Consider a fixed unwrapped row ($y = y_i$) across the low-resolution phase error $\Delta\phi_e^{(l)}$

$$\begin{aligned} \Delta\phi_e^{(l)}(x, y_i) &= 2\pi(\Delta k_x^{(l)} x + \Delta k_y^{(l)} y) + \Delta\varphi^{(l)} + m2\pi \\ &= 2\pi\Delta k_x^{(l)} x + \Big[2\pi\Delta k_y^{(l)} y_i + \Delta\varphi^{(l)} \\ &\qquad + m2\pi\Big] \end{aligned} \tag{3.4}$$

where m is an integer. Note that the term $\left[2\pi\Delta k_y^{(l)} y_i + \Delta\varphi^{(l)} + m2\pi\right]$ is a constant along the considered row and $\Delta\phi_e^{(l)}(x, y_i)$ is a line with the slope $2\pi\Delta k_x^{(l)}$. The slope $2\pi\Delta k_x^{(l)}$ in Equations (3.3) and (3.4) can be estimated by the slope of the line given by the 1D least squares fitting of row $y = y_i$ to Equation (3.4). In principle, all rows of $\Delta\phi_e^{(l)}$ give the same estimation of $\Delta k_x^{(l)}$ and therefore only one row is needed. However, due to possible noise and nonlinearity in the phase errors, the estimated value of $\Delta k_x^{(l)}$ given by each row can deviate from one another. Hence, all possible rows of $\Delta\phi_e^{(l)}$ that do not correspond to

background-only areas in the image are used and $\Delta k_x^{(l)}$ is estimated by the average of all the resulting slopes. $\Delta k_y^{(l)}$ is determined in the same manner as $\Delta k_x^{(l)}$ by using all the relevant columns of $\Delta \phi_e^{(l)}$.

Because of the 2π-ambiguity in phase unwrapping, the estimation of $\Delta \varphi^{(l)}$, which represents the global phase offset, cannot be incorporated into the process of estimating $\Delta k_x^{(l)}$ and $\Delta k_y^{(l)}$. Note that at the center of k-space ($k_x = 0, k_y = 0$), the phase of the received signal without motion-induced phase errors should be the average phase of the imaging object and the coil phase (ϕ_c), which is the same for all shots. Therefore, the phase of the corrupted received signal at the center of k-space gives an estimation of the global phase offset shifted by ϕ_c, which is $\Delta \varphi^{(l)} + \phi_c$. Correcting k-space data with $\Delta \varphi^{(l)} + \phi_c$ instead of $\Delta \varphi^{(l)}$ will result in k-space data with a consistent phase offset of ϕ_c across all interleaves. This consistent phase offset will only lead to a phase offset in the reconstructed complex image while leaving the magnitude image the same as if k-space data have been corrected with $\Delta \varphi^{(l)}$. Therefore, the phases of the received signal from each shot at the estimated k-space center can be used to undo the global phase offsets. There are two approaches to estimate the k-space center. In the first approach, k-space center can be estimated as the point in the corrected k-space trajectory that is closest to the origin (closest to 0). Because this estimation approach uses the corrected k-space trajectory, its precision depends on not only the k-space resolution but also the precision of the k-space shift estimation. In the second approach, similar to [42,45], the k-space center of each shot is estimated as the point where the k-space data of that shot reaches its maximum magnitude value. The precision of the k-space center estimation depends on the k-space resolution and not on the precision of the k-space shift estimation. Because the variable density spiral trajectory that oversamples the center of k-space is used, it is possible to obtain reasonably precise estimation of the constant phase offsets with small enough k-space shifts. In this work, we choose the second approach for the estimation of the k-space center.

Following is the summary of the KICT algorithm. For each shot:

- Phase error estimation.
  - Reconstruct low-resolution, no diffusion encoded ($b = 0$) image, I_L^0.

  - Reconstruct low-resolution, diffusion encoded ($b \neq 0$) image, I_L^b.
  - Extract and unwrap the phase of I_L^0 (Φ_0) and I_L^b ($\Phi^{(l)}$).
  - Compute the phase error: $\Delta\phi_e^{(l)} = \Phi^{(l)} - \Phi_0$.

- Estimation of K-space trajectory shifts.
  - Estimate $\Delta k_x^{(l)}$ by least squares fitting each row of $\Delta\phi_e^{(l)}$ to $2\pi\Delta k_x^{(l)}x + C$ and compute the average.
  - Estimate $\Delta k_y^{(l)}$ by least squares fitting each column of $\Delta\phi_e^{(l)}$ to $2\pi\Delta k_y^{(l)}y + C$ and compute the average.

- K-space trajectory correction and K-space phase offset estimation.
  - $k_x^{(l)} = k_x^{(l)} + \Delta k_x^{(l)}$.
  - $k_y^{(l)} = k_y^{(l)} + \Delta k_y^{(l)}$.
  - Estimate k-space phase offset, $\Delta\varphi$, as the phase of k-space data at the center of k-space.

- K-space phase offset correction.
  - Multiply k-space data with $e^{-j\Delta\varphi}$.

After correction of the k-space data with the KICT algorithm, a record of the new k-space coordinates is kept and used in subsequent reconstruction. Any image reconstruction scheme that takes into account the new k-space locations can be used to reconstruct the corrected diffusion-weighted image. *For a direct reconstruction method, such as gridding, the density compensation function must be recomputed based on the new sample locations.* In summary, the output of the KICT method is an updated set of k-space trajectories for each shot and the data for each shot has been corrected by a shot-specific phase offset.

3.2 KICT in Parallel DWI

The application of parallel imaging in multishot DWI is highly desirable because of its ability to reduce scanning time, T_2^* blurring and image distortions [39, 40, 43, 47, 84]. Reduction of scanning time is important, especially in the case of acquisition of multiple diffusion encoding directions as in fiber tracking and high angular resolution diffusion imaging schemes, where a high-resolution whole-brain study needs on the order of 1000 images. However, a major difficulty of parallel multishot DWI is the modulation of image phases by receiver coils' phases, which complicates the phase error correction. This is problematic as parallel reconstruction algorithms use receiver coils' phases in order to accurately reconstruct unaliased images. Therefore, motion correction algorithms used in parallel multishot DWI must preserve the phase of the imaging object and receiver coils. Note that for a GRAPPA-like reconstruction, preservation of the coil's relative phase may not be necessary. For a method like DPS which is imaged-based, using GRAPPA, which is a k-space-based method, for parallel reconstruction would require reconstructing corrected k-space data from the corrected images. Unlike DPS, KICT preserves the imaging object phase and receiver coils' phases and yields corrected k-space data. Therefore, it is possible to combine KICT and any existing parallel reconstruction method for parallel multishot DWI.

As previously discussed, DPS performs phase correction in image space. The results of DPS then are corrected images. Before DPS could be applied to any non-Cartesian parallel reconstruction algorithms, it is required that the corrected k-space data be computed from the corrected image space data. This computation propagates and potentially amplifies any residual errors that DPS fails to correct. Therefore, DPS is not a good match to non-Cartesian trajectories and parallel imaging reconstruction. We will compare KICT with the parallel imaging method of Liu et al. [43] which used the reconstruction approach to phase-correct for non-Cartesian, multicoil acquisitions.

For parallel multishot DWI, KICT corrects k-space data from individual shots and individual coils independently following the same procedure in single-coil DWI: shifting the k-space trajectory and applying the global phase offset to k-space data. Phase error ($\Delta\phi_e^{(l)}$) estimation, however, differs a little from the single-coil case in order to preserve individual

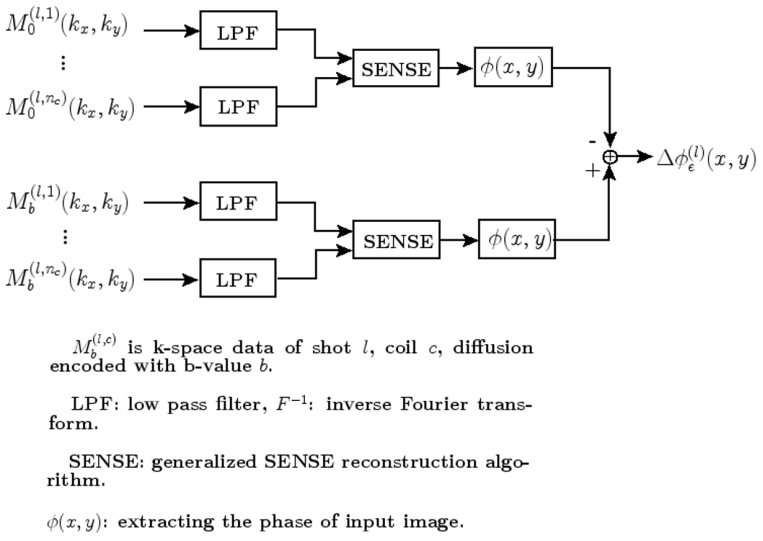

Figure 3.2: Phase error estimation for shot l in the case of multicoil.

coil phases. Low-resolution images (both $b = 0$ and $b \neq 0$) of individual shots are parallel-reconstructed from data acquired in the same shot at all receiver coils. Again, phase errors are estimated as the phase differences between $b = 0$ and $b \neq 0$ images. Figure 3.2 presents KICT correction procedure in the case of multicoil, multishot DWI.

Recall that in the single-coil case, KICT estimates the phase offset as the phase of k-space data at $k_x^{(l)} = 0, k_y^{(l)} = 0$. For the multicoil case, the phase of the k-space data of each coil at $k_x^{(l)} = 0, k_y^{(l)} = 0$ is the sum of the imaging object's phase and the corresponding receiver coils' phase. Because the receiver coils' phases are different, the phases of k-space data of different coils at $k_x^{(l)} = 0, k_y^{(l)} = 0$ are different. To compensate for this difference, average receiver coils' phases are estimated from $b = 0$ images of individual coils and applied back to the **corrected** k-space data of the corresponding coils for $b \neq 0$ shots.

For parallel reconstruction, the coil sensitivity is estimated as the ratio between the $b = 0$ (without diffusion encoding) low resolution, full FOV, single-shot, single-coil images and the sum of squares of $b = 0$ low resolution, full FOV, single-shot images of all coils. Although the estimated sensitivity maps may not be the true sensitivity of the coils, the reference is consistent among coils, shots, and diffusion directions. Therefore, the SENSE reconstruction result is not affected [85].

3.3 KICT Implementation

3.3.1 Simulation of KICT Motion-Induced Phase Correction

To give a quantitative analysis of its performance, the KICT algorithm is first tested with simulations. K-space data are simulated by multiplying an artifact-free non-diffusion-weighted image with a discrete Fourier transform (DFT) matrix computed on a desired trajectory–in this case, the variable density spiral trajectory. The simulated image has a matrix size of 128×128. A 16-shot variable density spiral trajectory is designed using the analytical formula proposed by Kim et al. with the oversampling factor $\alpha = 4$ [86]. Motion artifacts were simulated by applying random shifts with Gaussian distribution $\mathscr{N}(0, \sigma_k)$ to k-space trajectories and random phase offsets with uniform distribution $\mathscr{U}(-\pi, \pi)$ to k-space data of individual shots. Different levels of motion artifacts were considered by simulating with different variance of k-space shifts chosen from a set of 10 equidistant values in the range $(0, 5/FOV)$. For each value of shift variance, the simulation is repeated 20 times and the average normalized root mean square error (NRMSE) of the reconstructed image is then computed and used to assess the performance of the correction method.

For comparison, we also implemented the simulations with the same set of parameters with the image-based DPS method [41] and the reconstruction-based conjugate gradient (CG) [43] methods. While only the estimated phase errors are used in both KICT and DPS, we simulate the conjugate gradient method with both estimated phase errors and the exact phase errors that we apply. The reason is that according to our simulation results, the performance of the conjugate gradient method highly depends on the precision of the estimated phase errors.

3.3.2 *In Vivo* Experiments

All data sets were acquired on a head-only Siemens Allegra 3 T system using both a single-channel and a four-channel head coil in accordance with the institutional review board. A variable density (VD) spiral readout trajectory that oversamples the center of k-space was used to acquire data [86]. We used a variable density factor (α) of 4, matrix size of

128×128, 16 shots, and a field of view of 24 cm. A diffusion-weighted spin-echo sequence was implemented and used with KICT.

Four sets of experiments were carried out to test the performance of KICT *in vivo*. In the first set of experiments, six slices in the level of corpus callosum are acquired. A peripherally gated (using a finger nail pulse oximeter) diffusion sequence is used with three slices per R-R interval, slice thickness of 5.0 mm, TE of 57 ms and TR of 100 ms per slice. Diffusion encoding is applied in 1 direction [1 0 0] with diffusion-weighting parameters: $\delta = 22$ ms, $\Delta = 32$ ms and $g_{max} = 30$ mT/m corresponding to $b = 770$ s/mm^2. To assess stability of the method, we acquire 30 repetitions of the same b-value with a single diffusion encoding direction. The experiment is repeated on three different subjects.

The second set of experiments is acquired using the same diffusion-weighted spin-echo sequence as before but with 30 diffusion encoding directions. The experiment is also repeated on three subjects.

Performance of KICT in the case of parallel imaging (multicoil acquisitions) is evaluated through the third and fourth sets of experiments. Pulse sequence parameters are not changed as compared to the case of single-coil imaging; however, a four-channel head coil (USA Instruments) is used. Stability of the KICT algorithm is again tested using 30 repetitions of the same b-value and diffusion encoding direction in the third set of experiments. Similar to the second set of experiments, the fourth one gives data with 30 different diffusion encoding directions.

In addition to the above experiments, for the single-coil acquisition, a higher b-value with near isotropic imaging voxels was also examined. More specifically, the acquisition parameters for this experiment were: FOV = 24 cm, matrix size = 128 (in-plane resolution of 1.88×1.88 mm^2), $b = 1000$ s/mm^2 ($\delta = 25$ ms, $\Delta = 35$ ms, and $g_{max} = 30$ mT/m), 30 diffusion encoding directions. Six slices with 2 mm thickness in the level of brain stem are acquired.

In both multishot and single-shot DWI, cardiac gating has been shown to be necessary for diminishing phase errors and signal loss due to cardiac-induced brain pulsation and results in more accurate quantitative diffusion parameter maps [46, 87]. When cardiac gating is used, data are acquired during the quiescence duration of the cardiac cycle. We used peripheral

gating in all of our acquisitions. Data were acquired right after the trigger. Three slices per R-R interval were used with a TR of 100 ms, which results in data acquisition window of 300 ms after the pulse triggers. Previous work showed that a trigger delay of up to 500 ms is still acceptable [46]. All of our subjects had an R-R period of 700-1100 ms.

The acquired single-coil data were phase-corrected using DPS, CG, and KICT. All multicoil data were phase-corrected using CG and KICT. Phase errors used in DPS and CG correction are the nonlinear phase errors estimated from the center portions of k-space data. CG correction and reconstruction is iterated until no significant improvement is observed between two consecutive iterations.

3.4 Experimental Results

3.4.1 Results: Simulation

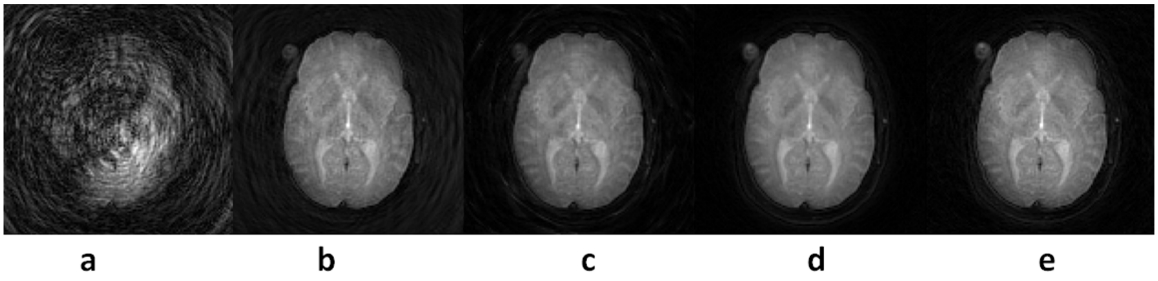

Figure 3.3: Simulation results. (a) uncorrected, (b) DPS, (c) conjugate gradient with estimated phase errors, (d) conjugate gradient with exact phase errors, (e) KICT.

Figure 3.3 compares the corrected image using DPS, conjugate gradient (CG) with estimated phase errors, CG with exact phase errors from the simulation study, and the proposed KICT method. Most of the signal loss and artifact in the uncorrected image are compensated in the DPS-corrected image. However, the KICT-corrected image shows improved overall image quality, especially in suppression of the background signal. CG with estimated phase errors gives comparable image quality to KICT, and CG with exact phase errors gives the best reconstructed image. Without attention to efficient coding, the correction and reconstruction times of a 128×128 image using DPS, KICT, and CG are 4 s, 5 s and 10 s,

respectively. The correction and reconstruction algorithms are implemented in MATLAB and executed on a 2.66 GHz Intel Core 2 CPU.

To have a more precise evaluation of the performance of the algorithms, we computed the normalized root mean square error of each reconstructed image. The normalized root mean square error (NRMSE) is computed as

$$\text{NRMSE} = \frac{\| \mathrm{I}_r - \mathrm{I}_0 \|_F}{\| \mathrm{I}_0 \|_F} \tag{3.5}$$

where I_r is the masked reconstructed magnitude image corrected using either DPS, CG, or KICT, I_0 is the masked simulated magnitude image, and $\| \, . \|_F$ is the Frobenius norm of a matrix (square root of sum of square of all elements). Masking of both reconstructed image and simulated image over the region of interest–the brain region only–gives a more accurate measurement of the performance of all algorithms.

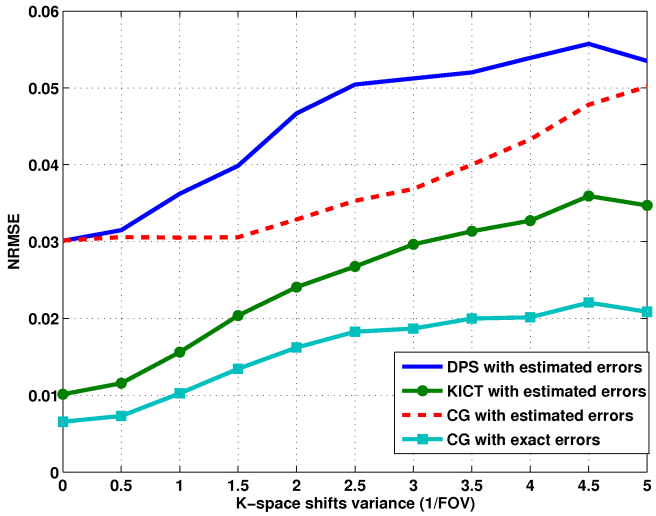

Figure 3.4: NRMSE of DPS, KICT, CG with estimated phase errors, and CG with exact phase errors.

Figure 3.4 shows the normalized root mean square error (NRMSE) of reconstructed images with DPS, KICT, CG using estimated phase errors, and CG using exact phase errors. For all methods, NRMSEs of reconstructed images increase as the variance increases, which is reasonable because higher k-space shifts lead to more severe undersampling of k-space. NRMSEs of reconstructed images using DPS are higher than NRMSEs of images recon-

structed by KICT at all given values of the shift variance. Because the defined NRMSE measures the discrepancy between the reconstructed images and the ground truth, lower values in the NRMSE of KICT mean that KICT gives more accurate reconstruction images than DPS does over the simulated levels of motion. KICT gives better performance than CG when CG also uses the estimated phase errors from the center of k-space. However, KICT is worse than CG when the exact phase errors are used. In practice, only the estimated phase errors would be available.

3.4.2 Results: *In Vivo* Experiments

Single-Channel KICT

Representative reconstruction images with and without motion-induced phase error correction for single-coil multishot DWI data sets are shown in Figure 3.5. Most of the signal loss in the uncorrected image (Figure 3.5(a)) is recovered when DPS is applied (Figure 3.5(b)) and further improvement is observed with KICT (Figure 3.5(c)). For example, in the regions pointed to by the arrows, fine structures are more visible with KICT correction than with DPS. Images corrected with KICT also appear to have higher resolution than DPS.

The higher resolution may result from regridding and recomputing of density compensation function after the phase error correction, which is not possible with DPS. Furthermore, without masking, DPS results show much higher background noise. From Figure 3.5(c) and Figure 3.5(d), KICT performs as well as, if not better than, CG. The reason is that with cardiac gating and the high position of the slices in the brain, nonrigid motion is highly suppressed. Therefore, the linear phase error assumption is adequate. Furthermore, as the simulation results suggest, CG needs a more accurate estimation of the phase errors to result in a good correction.

An important performance criterion of any correction algorithm is the resulting signal to noise ratio (SNR) of the corrected images. SNR in MR images can be measured in many different ways [88]. Here, we choose to measure SNR through the repeated acquisition of diffusion-weighted images with the same set of scan parameters. This method of computing

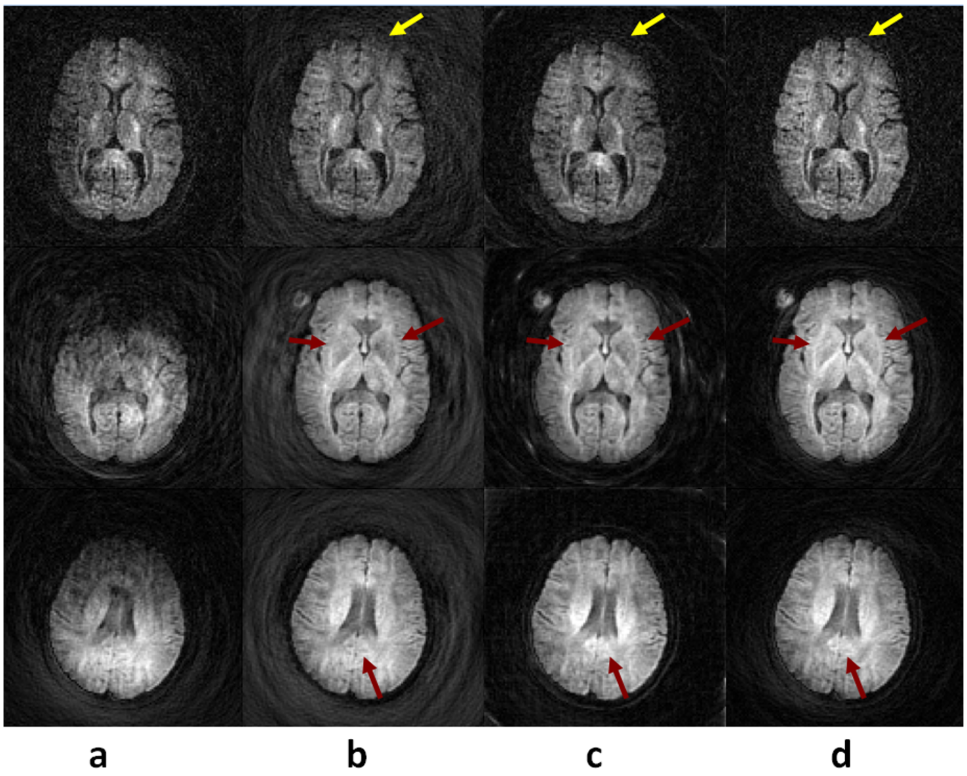

Figure 3.5: Reconstructed images from three subjects: (a) uncorrected, (b) corrected using DPS, (c) corrected using CG, (d) corrected using KICT. The first row has $b = 1000$ s/mm^2 and voxel size $= 1.88 \times 1.88 \times 2$ mm^3. The two last rows have $b = 770$ s/mm^2 and voxel size $= 1.88 \times 1.88 \times 5$ mm^3.

SNR allows accurate measurement of SNR in local regions regardless of the spatial variation in image noise [88]. SNR in this case is defined as the ratio between the mean and the standard deviation (SD) of the images reconstructed from repeatedly acquired data.

$$\mathrm{SNR}(x,y) = \frac{\sqrt{n}\bar{\mathrm{I}}(x,y)}{\sqrt{\sum_{r=1}^{n}\left[\mathrm{I}_r(x,y) - \bar{\mathrm{I}}(x,y)\right]^2}} \tag{3.6}$$

where $\mathrm{SNR}(x,y)$ is a pixel-by-pixel map of SNR, I_r is the magnitude of the reconstructed image from the r^{th} repetition, $\bar{\mathrm{I}}$ is the mean of the magnitudes of the reconstructed images from all repetitions, and n is the total number of repetitions available.

Figure 3.6 compares the SNR of the images corrected with DPS, CG, and KICT. Higher SNR is obtained in KICT as compared to DPS and CG. DPS suffers from residual aliased phase errors that are inconsistent across different acquisitions, corrections, and reconstruc-

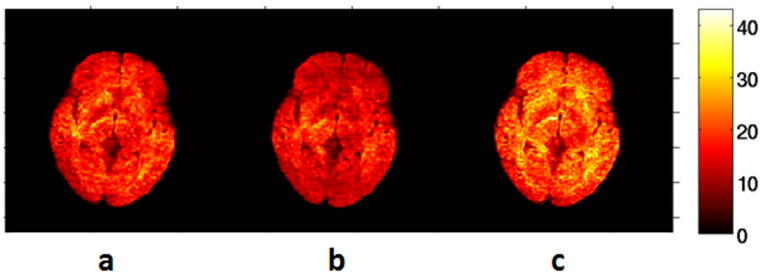

Figure 3.6: SNR of reconstructed images from 30 repetitions for a typical slice: (a) DPS, (b) CG, (c) KICT. $b = 770$ s/mm^2, diffusion encoding direction [1 0 0], voxel size $= 1.88 \times 1.88 \times 5$ mm^3.

tions. Therefore, DPS-corrected images have higher variance, which leads to a low SNR. Because the images are reconstructed from the same set of data, the higher SNR of KICT as compared to DPS shows that residual nonlinear phase errors in KICT are smaller than the residual aliased phase errors in DPS. Lower SNR in CG as compared to both DPS and KICT shows again that CG indeed needs a sophisticated phase error estimation to perform well.

Figure 3.7 compares the fractional anisotropy (FA) maps of images corrected with DPS and KICT from the 30-direction DTI data (the second set of experiments). For color coded FA maps (Figure 3.7(b)), red encodes the left-right diffusion direction, green encodes the anterior-posterior direction, and blue encodes the superior-inferior direction. The FA maps were computed using the FMRIB Software Library (FSL) [89–92]. In slices at higher levels in the brain (the first two rows in Figure 3.7), FA maps of images corrected with KICT reveal fibers that are barely visible in those corrected with DPS (pointed by arrows). KICT also gives better localized fiber tracts and higher FA values. Compared to CG, KICT gives similar FA maps in these high level slices. When moving to lower slices which may have higher contributions of nonlinear phase errors, to the level of the brain stem (the last row in Figure 3.7), KICT is still comparable to CG.

Multichannel KICT

As previously discussed, a major difficulty of parallel multishot DWI is the modulation of phase errors by receiver coils' phases, which complicates the phase error correction. Unlike

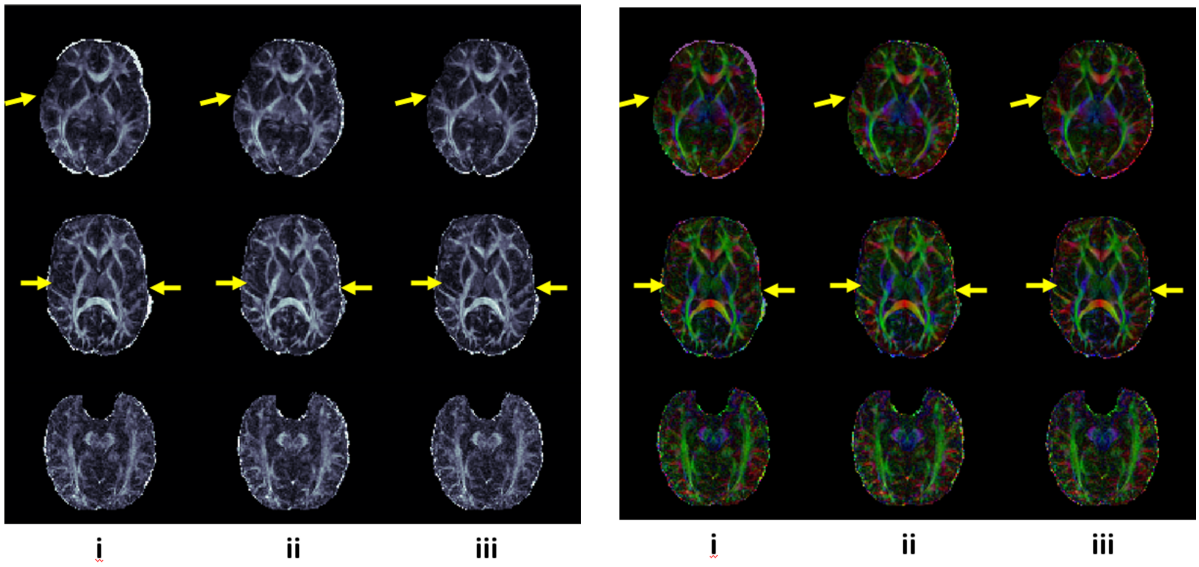

(a) FA maps

(b) Color-coded FA maps

Figure 3.7: (a) FA maps, (b) color-coded FA maps. Within each subfigure, (i) DPS, (ii) CG, (iii) KICT. Three rows correspond to slices from three different subjects. The first two rows have $b = 770$ s/mm^2 and voxel size $= 1.88 \times 1.88 \times 5$ mm^3. The last row has $b = 1000$ s/mm^2 and voxel size $= 1.88 \times 1.88 \times 2$ mm^3.

DPS, KICT preserves the imaging object phase and receiver coils' phases. Therefore, it is possible to combine KICT and any existing parallel reconstruction method for parallel multishot DWI.

The third and fourth sets of data are experiments of parallel DWI. Figure 3.8 shows the reconstruction images of multicoil, multishot diffusion-weighted data with phase correction and SENSE reconstruction with reduction factor of 1, 2, and 2.7. Eight shots taken from a 16-shot acquisition by skipping every other shot are used to obtain the reduction factor of 2. Six shots taken from a 16-shot acquisition by skipping every two shots are used to obtain the reduction factor of 2.7. For KICT, since the k-space trajectory is shifted spirals, a combination of an iterative reconstruction algorithm, quadratically-penalized weighted least squares (QPWLS), and the generalized SENSE [81, 85, 93, 94] is used to get both the low resolution images for phase error information and the final phase-corrected image. The sensitivity maps are determined from the low-resolution $b = 0$ images and the phase errors are, as in the single-coil case, the phase difference between $b \neq 0$ images and $b = 0$ images of

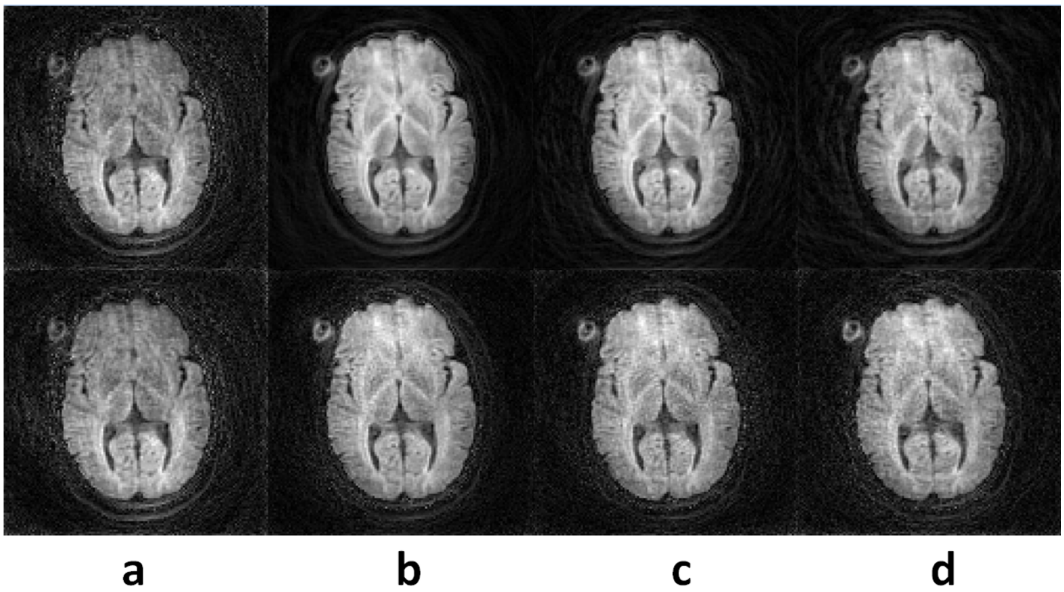

Figure 3.8: Parallel DWI reconstructed images. (a) Uncorrected SENSE reduction factor of 1 vs. phase correction and SENSE reconstruction of four-channel diffusion-weighted data with (b) reduction factor of 1, (c) reduction factor of 2 , and (d) reduction factor of 2.7. The first and second rows correspond to CG correction and KICT correction, respectively.

individual shots. For the reconstruction-based CG method, the composite sensitivity maps, which include the coils' sensitivity and phase errors [43], are estimated from the center part of the k-space data from individual shots. As can be observed from Figure 3.8, the image quality is restored significantly when phase correction is applied. KICT gives image quality comparable to that of CG when no reduction in data is used (reduction factor of 1). With higher reduction factors, KICT results in noisier corrected images than CG.

To get a quantitative evaluation of the two phase correction methods, we repeated the SNR analysis of the single-coil acquisition for the case of multicoil acquisitions. SNR is evaluated using the SNR map defined in Equation (3.6).

Figure 3.9 shows the computed SNR maps from a typical slice. As expected from the results in Figure 3.8, CG results in better SNRs than KICT for reduced data sets. However, KICT provides comparable motion-induced phase correction for the multicoil acquisition. Additionally, KICT could be combined with other parallel reconstruction algorithms that can use the corrected k-space data. Furthermore, the phase error estimation and correction and reconstruction times (with 20 iterations) of a 128×128 image using the CG method

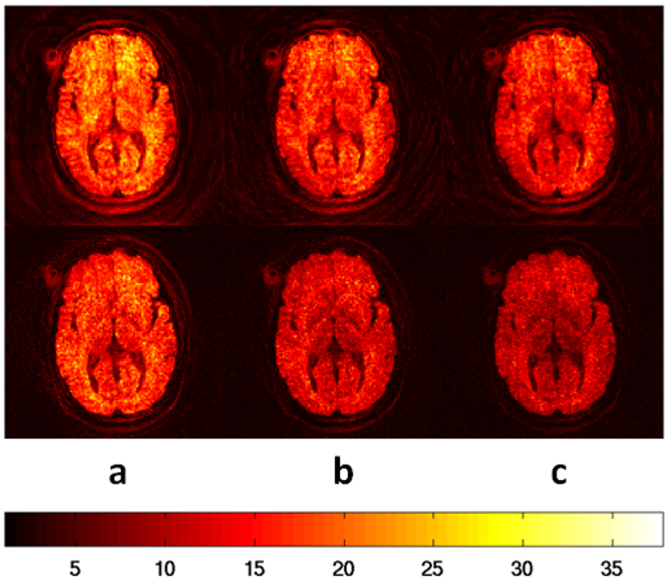

Figure 3.9: SNR of reconstructed images from 30 repetitions for a typical slice: (a) reduction factor of 1, (b) reduction factor of 2, and (c) reduction factor of 2.7. The first and second rows correspond to CG correction and KICT correction, respectively.

and KICT in combination with SENSE are 49 s and 20 s on a 2.66 GHz Intel Core 2 CPU, respectively.

FA maps and color-coded FA maps of parallel DWI with reduction factor of 1, 2, and 2.7 are presented in Figure 3.10. High quality FA maps are achieved, even with a reduction factor of 2.7.

3.5 Discussion and Conclusion

Motion-induced phase error in multishot DWI has been extensively studied and recent works have developed algorithms to correct for arbitrary phase errors in DWI [43, 44]. These algorithms, however, are rather complex, time-consuming, and as our results suggest, require quite accurate phase error maps. When cardiac gating is used, solving a simpler problem than those in [43, 44], i.e. correcting for linear phase errors only, still gives reasonably good images with much shorter correction times, sometimes even exceeding the quality of the more costly reconstructions. In addition, as will be shown in the next chapter, KICT is flexible and easily extended to 3D data sets. The work presented here is an effort to develop

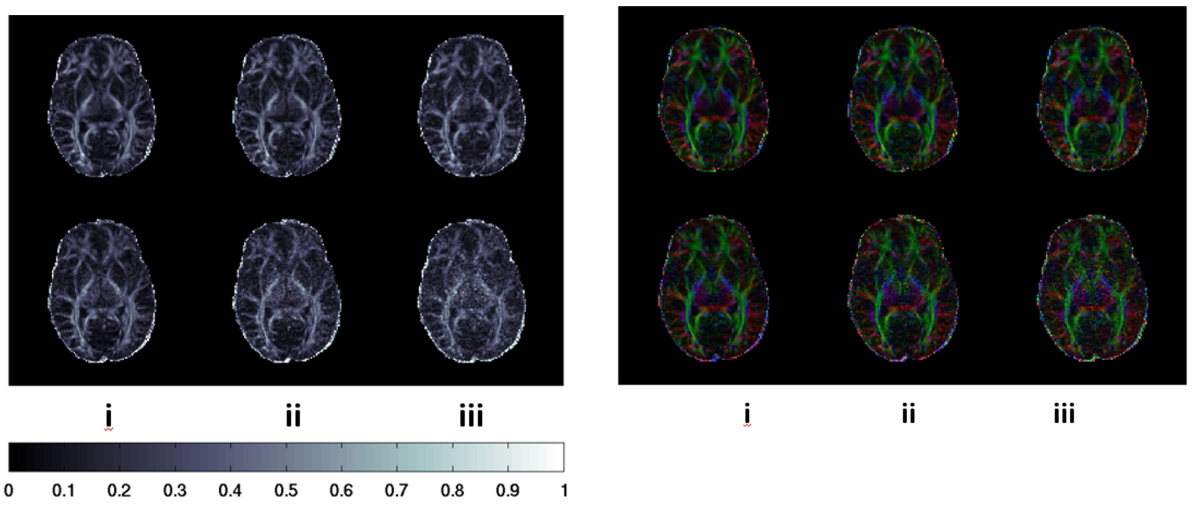

(a) FA maps

(b) Color-coded FA maps

Figure 3.10: (a) FA maps, (b) color-coded FA maps. Within each subfigure, (i) reduction factor of 1, (ii) reduction factor of 2, and (iii) reduction factor of 2.7. The first and second rows correspond to CG correction and KICT correction, respectively.

a simple and fast algorithm for linear phase error correction in DWI.

The interpretation of linear phase errors in image space as k-space trajectory shifts and constant phase offset in k-space data has been exploited previously [42, 45]. In those works, k-space trajectory shifts were estimated as the shifts of the peak magnitude k-space data points. The accuracy of this shift estimation, therefore, depends on the sampling resolution in k-space. With elaborate post-processing of the navigator data, the highest precision achieved in shift estimation is limited at half a k-space sampling distance [42], which still leads to residual phase errors. KICT overcomes this limitation by estimating the k-space trajectory shifts from the slopes of the phase errors instead.

We have shown the motion-induced phase error correction performance of KICT for both single-coil and multicoil imaging. Together with a pulse triggered acquisition, KICT gives better performance than the nonlinear phase correction methods including DPS and our implementation of CG in the upper part of the brain and comparable performance in the lower part of the brain where pulsation is more severe. By estimating low-resolution motion-induced phase errors in image space and removing the errors in k-space, KICT can eliminate the concern about residual aliasing of phase errors along with improper sampling density

compensation, which are the major drawbacks of DPS. As compared to CG, KICT provides a simpler and faster correction method with acceptable image quality trade-off. Phase errors experienced by individual shots are estimated using oversampled regions of the variable density spiral of $b = 0$ images and $b \neq 0$ images. Therefore, no additional data needs to be collected.

The output of KICT is the corrected k-space data. Furthermore, KICT makes no changes to the relative phases of imaging object and receiver coils. Therefore, it is possible to apply KICT to multicoil DWI and then reconstruct images with any type of parallel reconstruction method. Previously, phase-corrected multicoil DWI was performed by treating phase errors in combination with sensitivity profiles as an encoding matrix [43]. The reconstruction and phase correction are done simultaneously using sensitivity encoding (SENSE). The size of the SENSE problem is proportional to the product of the number of coils used, the number of shots in the k-space trajectory and the number of k-space locations. Therefore, even with efficient algorithms, computation time is an issue, especially when a large number of images are involved. The output of KICT, as discussed earlier, is corrected k-space data. Therefore, no phase correction is needed during the parallel reconstruction, which gives a reduction factor in the size of the problem equal to the number of shots. For single-coil problem, the correction and reconstruction times of a 128×128 image using CG and KICT are 10 s and 5 s, respectively. For multicoil problem, the correction and reconstruction times of a 128×128 image using CG and KICT in combination with SENSE are 49 s and 20 s, respectively. After KICT correction, any parallel reconstruction algorithm for non-Cartesian trajectory can be used to reconstruct the images. Since there are no assumptions in KICT about the type of k-space trajectory used, KICT can correct for diffusion-weighted data acquired with a variety of k-space trajectories.

A drawback of KICT is the inability to correct for nonlinear phase errors. As discussed earlier, nonlinear phase errors are the results of nonrigid motion during diffusion encoding. A major source of this nonrigid motion is cardiac-induced pulsations. It has been previously shown that the acquired diffusion-weighted signal corrupted by nonrigid motion has phase and amplitude that are highly correlated with the cardiac cycle [37]. Therefore, in the current acquisition, peripheral gating is used to eliminate brain pulsation so that the rigid-

body motion assumption is enhanced. Furthermore, in reduced-FOV acquisitions, which is currently a research focus [28, 75], even when nonlinear phase errors are present, we expect that the linear phase error assumption may become adequate across smaller spatial scale. However, when reconstruction time is not a concern, peripheral gating is not available and whole brain coverage is required, nonlinear phase error compensation algorithms like the ones presented in [43] for non-Cartesian trajectories and [44] for Cartesian trajectory may be the preferred choices.

A potential challenge of multishot diffusion imaging that is highlighted by the KICT method is that the correction involves random shifting of individual shots in the k-space trajectories, which possibly leads to locally undersampled k-space data. Regridding and recomputation of density compensation function after k-space correction significantly suppress artifacts in the reconstructed images. In the case of much higher motion, repeated collections of the same set of data are probably required to adequately sample k-space and correctly reconstruct the images [42]. When KICT is applied to multicoil DWI, the accompanied parallel reconstruction method can further reduce the effect of locally undersampled k-space after correction.

In conclusion, a new method for correction of motion-induced phase errors in diffusion-weighted imaging is presented and tested with simulated and real single-coil, multishot and multicoil, multishot DWI data. Using KICT, we obtain better reconstructed images than DPS over the experimented range of motion. Because linear phase estimation is done in k_x and k_y separately through 1D line fitting, the correction is fast. KICT also allows the preservation of imaging object phase and receiver coils' phase for parallel imaging.

CHAPTER 4

3D DIFFUSION TENSOR IMAGING

As reviewed in Chapter 2, although 3D DTI is a must for high isotropic resolution, the realization of 3D DTI faces many challenges, most difficult of which is the lack of a robust, time-efficient 3D motion-induced phase error estimation and correction algorithm.

Our previously presented KICT method in Chapter 3 is a 2D time-efficient rigid-body-motion-induced phase error correction algorithm that is extendible to 3D cases. If a 3D navigator is available, our extension will be a time-efficient and truly 3D correction method that, similar to its 2D version, does not suffer residual phase errors, and does not have performance dependence on k-space resolution. The availability of a 3D motion-induced phase error correction algorithm enables us to realize *in vivo* 3D DTI.

The objective of the present chapter is the development of a technique for whole brain coverage, high spatial resolution DTI using pulsed gradient spin echo diffusion preparation while maintaining reasonable acquisition time. To achieve this objective, an interleaved multislab acquisition strategy is proposed and is optimized for achieving a tolerable total scan time and reasonable SNR, based on a thorough analysis of SNR and total scan time tradeoffs. Eddy-current effects are limited by employing a well-designed, twice refocused diffusion preparation. Multishot acquisition is used for reducing magnetic susceptibility artifacts. The multishot acquisition is accompanied by cardiac gating and the extension of 2D KICT for true 3D motion-induced phase error correction, yielding ghost-free diffusion-weighted images. Simulations and *in vivo* data show the ability to achieve 1.88 x 1.88 x 2 mm^3 resolution, cardiac-gated, six-direction DTI with whole brain coverage within 30 minutes.

In the following sections, we will sequentially go through the challenges of implementing 3D multislab DTI including the sampling strategy, SNR consideration, slab boundary arti-

facts, eddy currents, 3D motion-induced phase errors, efficient cardiac-gating, and 3D image reconstruction.

4.1 DW-PGSE with Navigator and Sampling Strategy

A diffusion-weighted spin echo sequence is implemented in the present study because of its simple implementation, straightforward diffusion-weighted signal model, and high SNR. The timing diagram of the sequence is shown in Figure 4.1. To traverse the 3D k-space, the stack of multishot constant density spiral trajectory is used [95]. For each repetition of the pulse sequence, a shot in one plane of the stack is acquired. A second refocusing RF pulse is added after data acquisition for acquiring 3D navigators, which are low resolution stacks of single-shot spirals in the center of the 3D k-space.

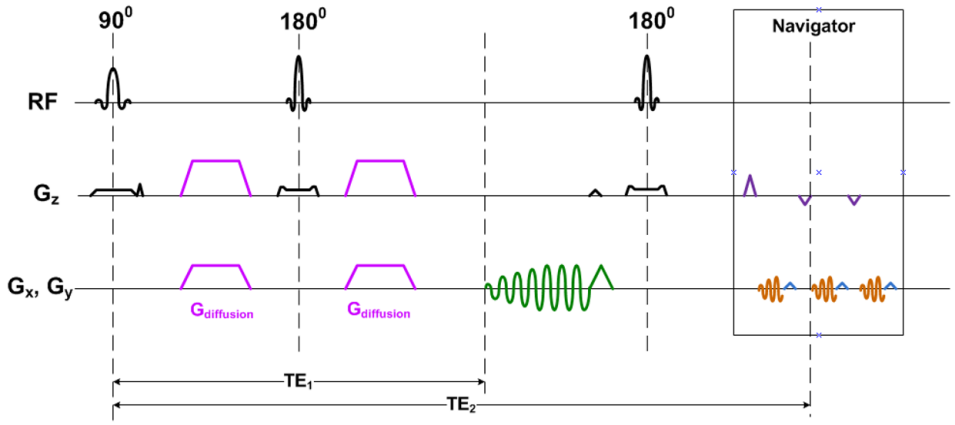

Figure 4.1: Pulse sequence time diagram.

Conventional 3D diffusion-weighted spin echo acquisitions are prohibitively time consuming. The reason is that the whole 3D volume is excited every TR and only one shot (trajectory in (k_x, k_y, k_z)) in the 3D volume can be acquired per TR. To speed up the acquisition and recover some of the time benefits of a 2D acquisition, we propose to use an interleaved 3D multislab acquisition. In a 3D multislab acquisition, the whole 3D imaging volume is divided into multiple smaller volumes called slabs. Each slab will then be imaged independently using a standard 3D acquisition. Data acquired from each slab is then reconstructed

independently and concatenated to get a single 3D image of the whole 3D volume. Because each slab is excited and imaged independently, all the slabs can be interleaved in a similar fashion as 2D interleaved slice acquisition to speed up the acquisition and increase the effective TR.

As compared to a conventional 3D acquisition, the multislab 3D acquisition suffers from reduced SNR because a smaller 3D volume (slab) is excited in each TR. However, the slabs can be interleaved, which leads to an increased effective TR for the same total imaging time. This increase in TR increases the time for T1 recovery, and therefore results in an increase in SNR. To optimize the acquisition strategy for our study, we performed a quantitative SNR comparison between the 2D, the single-slab 3D, and the multislab 3D approaches.

The SNR of any MR acquisition is given by the following scaling relationship [55]:

$$\text{SNR} \propto \Delta x \Delta y \Delta z \sqrt{T_{RO(total)}} \sqrt{\text{NEX}} \tag{4.1}$$

where $\Delta x, \Delta y$, and Δz define the imaging voxel volume, NEX is the number of repetitions, and $T_{RO(total)}$ is defined as the total readout duration per one excited volume (including all k-space points and all shots). For 2D acquisitions, $T_{RO(total)}$ represents the total readout time for a single slice. For 3D acquisitions, $T_{RO(total)}$ represents the total readout time for the whole 3D volumes. For 3D multislab acquisition, $T_{RO(total)}$ represents the total readout time for a single slab.

Besides resolution, number of repetitions, and the total readout time, SNR also depends on the employed pulse sequence and the corresponding parameters used (TR, TE), and properties of the imaging tissue (T1, T2). Since a spin echo diffusion sequence is used, the following SNR analysis is based on the signal formula of a spin echo sequence with a 90^o excitation pulse and a 180^o refocusing pulse [55]

$$S \propto M_0 \left[1 - 2 \exp\Big(- \frac{TR - TE/2}{T1} \Big) + \exp\Big(- \frac{TR}{T1} \Big) \right] \exp\Big(- \frac{TE}{T2} \Big) \tag{4.2}$$

For ease of presentation as well as giving an SNR analysis of the actual acquisition technique used in the present study, the subsequent analysis is specifically performed for a stack

of multishot constant density spiral acquisition. For other types of acquisition, the same analysis can still be applied with minor modifications in computation of the total readout time per an excited volume and the repetition time TR.

Let n_l be the number of spiral shots, T_{RO} be the duration of each shot of the spiral, and N_z be the number of the third dimension encoding lines. Define T_{seq} as the time duration of a single repetition of the sequence, i.e., the encoding and acquisition time of a single-shot, single-slice/single-third-dimension encoding line of data. Notice that T_{seq} is in general different from the effective TR since TR is the time between two consecutive excitations of the same imaged volume. Let N_z also be the number of 2D slices required in an equivalent 2D acquisition to cover the same volume as 3D acquisition at the same resolution.

4.1.1 SNR Analysis of Interleaved Multislab Acquisition without Cardiac-Gating

Consider the cases where no cardiac-gating is used and the total scan time per 3D imaged volume T_{tot} is the same for all acquisition schemes ($T_{tot} = N_z T_{seq}$). Because of the possibility of interleaving, 2D acquisition can have $TR = N_z T_{seq}$. Similarly, 3D multislab acquisition can have $TR = N_{slab} T_{seq}$ where N_{slab} is the total number of slabs that make up the imaging 3D volume. Meanwhile, for 3D acquisition, $TR = T_{seq}$, as the entire volume is excited with every repetition. The signal of a spin echo sequence with 2D encoding (S_{2D}), 3D single-slab encoding (S_{3Ds}), and 3D multislab encoding (S_{3Dm}) can be expressed in terms of T_{seq}, respectively, as

$$\begin{aligned} S_{2D} &\propto \left[1 - 2\exp\Big(-\tfrac{N_z T_{seq} - TE/2}{T1}\Big) + \exp\Big(-\tfrac{N_z T_{seq}}{T1}\Big)\right] \exp\Big(-\tfrac{TE}{T2}\Big) \\ S_{3Ds} &\propto \left[1 - 2\exp\Big(-\tfrac{T_{seq} - TE/2}{T1}\Big) + \exp\Big(-\tfrac{T_{seq}}{T1}\Big)\right] \exp\Big(-\tfrac{TE}{T2}\Big) \\ S_{3Dm} &\propto \left[1 - 2\exp\Big(-\tfrac{N_{slab} T_{seq} - TE/2}{T1}\Big) + \exp\Big(-\tfrac{N_{slab} T_{seq}}{T1}\Big)\right] \exp\Big(-\tfrac{TE}{T2}\Big) \end{aligned} \tag{4.3}$$

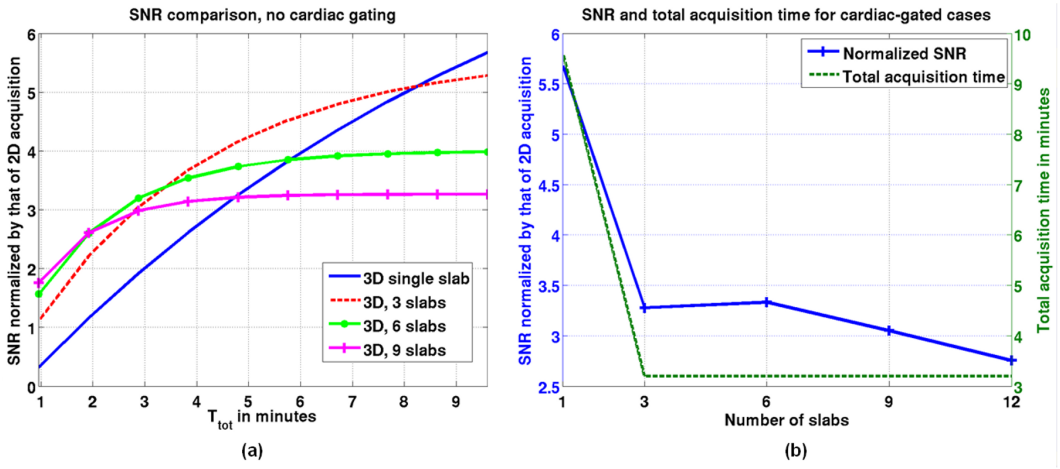

Figure 4.2: SNR comparison between 2D, single-slab 3D, and multislab 3D acquisitions.

Fixing the resolution and the trajectory used, and letting SNR_{2D}, SNR_{3Ds}, and SNR_{3Dm} be the SNRs for 2D, single-slab 3D, and multislab 3D cases, respectively, from Equations (4.1) and (4.3) we have

$$\begin{aligned} \frac{SNR_{3Ds}}{SNR_{2D}} &= \frac{1-2\exp\left(-\frac{T_{seq}-TE/2}{T1}\right)+\exp\left(-\frac{T_{seq}}{T2}\right)}{1-2\exp\left(-\frac{N_zT_{seq}-TE/2}{T1}\right)+\exp\left(-\frac{N_zT_{seq}}{T1}\right)}\sqrt{N_z} \\ \frac{SNR_{3Dm}}{SNR_{2D}} &= \frac{1-2\exp\left(-\frac{N_{slab}T_{seq}-TE/2}{T1}\right)+\exp\left(-\frac{N_{slab}T_{seq}}{T2}\right)}{1-2\exp\left(-\frac{N_z\times T_{seq}-TE/2}{T1}\right)+\exp\left(-\frac{N_zT_{seq}}{T1}\right)}\sqrt{\frac{N_z}{N_{slab}}} \end{aligned} \tag{4.4}$$

Notice that

$$\begin{aligned} T_{RO(total)}(3Ds) &= N_zT_{RO(total)}(2D) \\ T_{RO(total)}(3Dm) &= \frac{N_z}{N_{slab}}T_{RO(total)}(2D) \end{aligned} \tag{4.5}$$

Figure 4.2(a) shows the results of SNR calculation for 2D, 3D, and 3D multislab cases for different total acquisition time using Equation (4.4). In this figure, we use parameters that will be similar to those used in the *in vivo* experiments. The total number of slices simulated (N_z) is 96, TE = 65 ms, T1 = 1084 ms, T2 = 69 ms [96]. Averaging of multiple repetitions for a 2D acquisition is not considered.

According to Figure 4.2(a), 3D single-slab is superior to both 2D and 3D multislab when the total scan time per 3D imaged volume T_{tot} is long enough ($>$ 8 minutes) so that the

effect of T1 relaxation on the received signal is small. When T_{tot} is moderate, 3D multislab gains from both interleaving and partial 3D acquisition and therefore performs better than 2D and single-slab 3D acquisitions. The SNR of the 3D multislab strategy changes with the number of slabs used. The higher the number of slabs, the more SNR gain from interleaving (increasing effective TR). The smaller the number of slabs (the higher the number of slices per slab), the more SNR gain from partial 3D acquisition.

4.1.2 SNR Analysis of Interleaved Multislab Acquisition with Cardiac-Gating

Consider the cases where cardiac-gating is used. It has been shown that to reduce the effect of pulsation in DTI, data should be acquired during the quiescent period of the cardiac cycle (32-34). The duration of this quiescent period has been reported to be approximately 500 ms. The sequence time in the present experiments is approximately 150 ms. Therefore, we can have at most three repetitions of the sequence in one RR interval. If more than one sequence repetition is performed per RR for 3D single-slab case, the resulting TR will be 150 ms which leads to low SNR (Figure 4.2(a)). Furthermore, the TR can be uneven due to the waiting period from the end of all acquisitions to the next R peak, leading to artifacts. Equation (4.4) can still be used for SNR comparison with the notice that effectively $TR(2D) = \frac{N_z}{3}RR$, $TR(3Dm) = \frac{N_{slab}}{3}RR$, and $TR(3Ds) = RR$. Total acquisition times per volume in this case are $T_{tot}(2D) = T_{tot}(3Dm) = \frac{N_z n_l}{3}$, and $T_{tot}(3Ds) = N_z n_l RR$.

Figure 4.2(b) shows the SNR and total scan time comparison between 2D, 3D single-slab, and 3D multislab acquisitions when RR = 1 s. 3D single-slab acquisition has a higher SNR than both 2D and 3D multislab acquisition at a cost of unreasonable total scan time per volume ($>$ 9 minutes). Figure 4.2(b) shows that the 3D multislab acquisition with 6 slabs results in adequate SNR within reasonable total scan time per 3D volume ($\approx$ 3.2 minutes). To quantitatively characterize the tradeoffs between SNR and total acquisition, define SNR efficiency η_{SNR} as

$$\eta_{SNR} = \frac{SNR}{\sqrt{T_{tot}}} \tag{4.6}$$

Multislab acquisition with six slabs results in an SNR efficiency gain of 1.86 compared to

2D acquisition.

4.2 Multislab Acquisition and the "Venetian Blind" Artifact

One limitation of the multislab acquisition is the potential for the Venetian blind artifact after the concatenation of the slabs as a result of imperfect slab selection profile, slab cross-talk, and field inhomogeneity [97]. An imperfect slab selective profile can lead to the broadening of the actual selected slab as compared to the prescribed one and aliasing occurs unless some oversampling is done in the slice direction. The imperfect slab profile can also make spins at the slab boundaries experience irregular TR as they are excited during the acquisition of multiple slabs. This irregular TR may lead to signal loss and hence increase the Venetian blind in the reconstructed images. To minimize these boundary artifacts we interleave odd and even slabs, overlap adjacent slabs, and discard overlapped slices at the boundary when reformatting the 3D volume. An example of acquisition strategy to minimize the boundary artifact for the case of six slabs is illustrated in Figure 4.3. Examples of reconstructed images with (b) and without (a) minimized boundary artifact acquisition are shown in Figure 4.4.

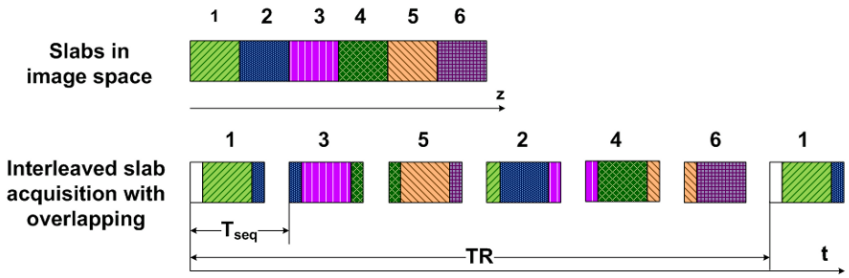

Figure 4.3: Interleaved slab acquisition for reducing slab boundary artifacts.

4.3 Diffusion Preparation and Eddy Current Effects

Long-duration and high-amplitude gradients used in diffusion preparation can induce eddy currents that lead to variable geometric distortions and blurring across different diffusion en-

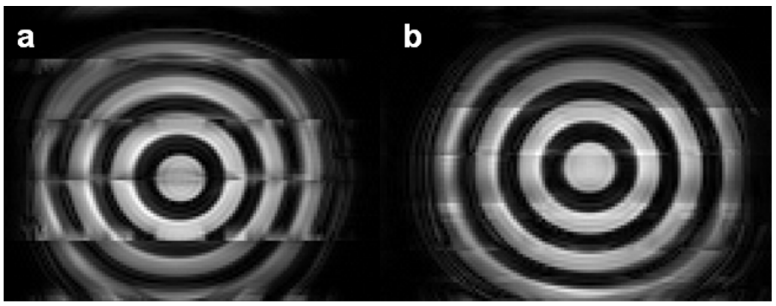

Figure 4.4: Slab boundary effects: (a) without minimized boundary artifact acquisition, (b) with minimized boundary artifact acquisition.

coding directions. To reduce these potential eddy-current effects, a TRSE diffusion-prepared sequence (Figure 2.7 or Figure 2.8) is investigated besides the conventional bipolar diffusion-prepared sequence (Figure 4.1). The choice of the eddy-current-compensated sequence depends on the residual eddy current, and the required percentage increase in TE. The residual eddy current of each reviewed strategy in Section 2.5 is computed as the ratio between the eddy current right after all gradient pulses have been played out (I_t) and eddy-current amplitude of a single gradient ramp (I_0). For comparison, the residual eddy current (I_t/I_0) for a sequence without eddy current compensation is shown in Figure 4.5.

Figure 4.6 shows contour plots of the residual eddy current of each considered method when the compensated time constant is different from the actual time constant of the scanner (misadjustment) for a diffusion encoding scheme with b-value of 1040 s/mm^2, diffusion duration of $\delta = 26$ ms, and diffusion time of $\Delta = 32.6$ ms. Eddy-current compensation with a single refocusing pulse (Figure 4.6(c)) gives the smallest residual eddy-current compensation ($< 10\%$) in most cases of misadjustment. The original twice refocused strategy (Figure 4.6(a)) gives the highest sensitivity to misadjustment for medium to long time constant (> 20 ms). For short time constant (< 10 ms), all three strategies give similar performance.

Regarding the required increase in minimum TE as compared to the non-compensated sequence, Figure 4.7 shows the ratios of the increase in minimum TEs of eddy-current-compensated sequences to the minimum TE of noncompensated sequences, again, for the diffusion encoding scheme with b-value of 1040 s/mm^2, diffusion duration of $\delta = 26$ ms, and diffusion time of $\Delta = 32.6$ ms. TRSE sequence gives the smallest increase in TE when

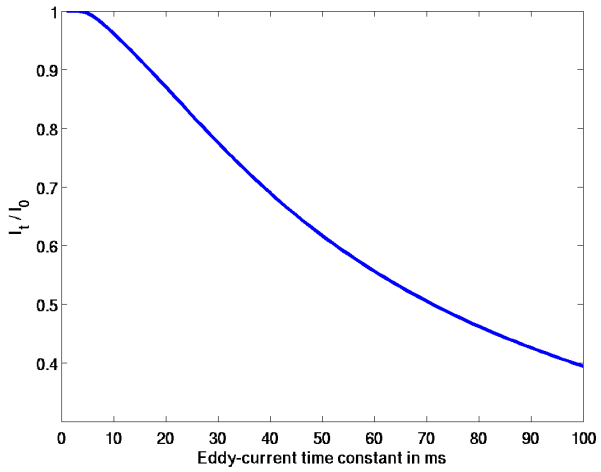

Figure 4.5: Residual eddy current, computed as the ratio between the eddy current right after all gradient pulses have been played out (I_t) and eddy current amplitude of a single gradient ramp (I_0), of diffusion-weighted spin echo sequence without eddy-current compensation for different eddy-current time constant.

compensated time constant is < 25 ms while modified TRSE gives the smallest increase in TE when compensated time constant is > 25 ms.

Compromising between the sensitivity to compensated time constant misadjustment and the increase in minimum TE, the modified TRSE strategy is chosen for eddy-current compensation in the present study.

4.4 3D Motion-Induced Phase Errors

Motion-induced phase errors in 3D DTI are more severe than in 2D DTI due to the additional phase errors in the z encoding direction and the possibly longer scan time, which can result in increased subject motion. Again, we rely on cardiac gating to eliminate pulsation-related motion and compensate for only rigid body motion. Extending Equation (2.39), which describes the effects of rigid body motion on a single-shot of data into the 3D case, we have

$$\tilde{I}^{(l)}(x,y,z) = \exp\left[j\Big(\Delta\varphi_e^{(l)} + 2\pi(\Delta k_x^{(l)}x + \Delta k_y^{(l)}y + \Delta k_z^{(l)}z)\Big)\right] I^{(l)}(x,y,z) \qquad (4.7)$$

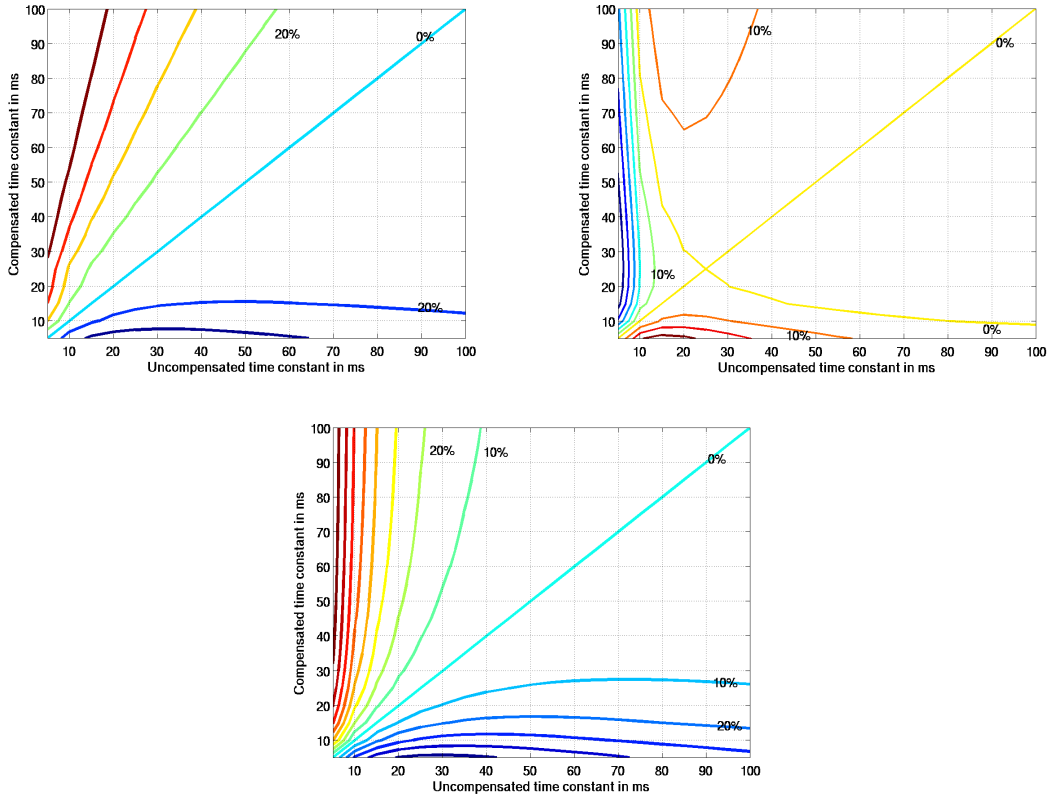

Figure 4.6: Contour plots showing residual eddy current from mismatches between the time constant of the actual eddy current of the scanner and the time constant that was compensated by the sequence: (a) original TRSE [50], (b) single-refocused eddy-current compensation [82] and (c) modified TRSE for two time constant compensation [83].

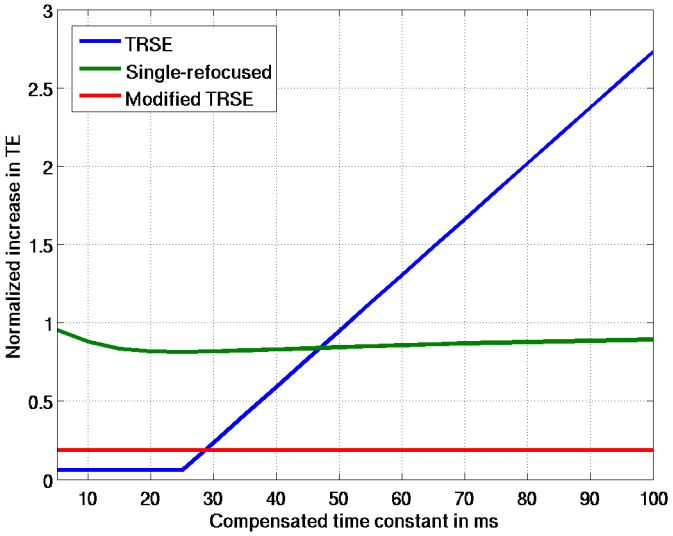

Figure 4.7: Required increase in minimum TE for eddy-current-compensated sequences. The normalized increase is normalized by the minimum TE of noncompensated sequences.

where the index (l) refers to shot l, $\tilde{I}^{(l)}(x,y,z)$ is the corrupted image, $I^{(l)}$ is the true image, and $\left(\Delta\varphi_e^{(l)} + 2\pi(\Delta k_x^{(l)}x + \Delta k_y^{(l)}y + \Delta k_z^{(l)}z)\right)$ is the linear phase error with offset $\Delta\varphi_e^{(l)}$ and slopes $2\pi\Delta k_x^{(l)}, 2\pi\Delta k_y^{(l)}$, and $2\pi\Delta k_z^{(l)}$ in the x, y, and z direction, respectively. In k-space domain, the errors become

$$\tilde{S}^{(l)} = \exp\left(j\Delta\varphi_e^{(l)}\right) S^{(l)}\left(k_x^{(l)} - \Delta k_x^{(l)}, k_y^{(l)} - \Delta k_y^{(l)}, k_z^{(l)-\Delta k_z^{(l)}}\right) \tag{4.8}$$

Parameters of the linear phase errors in Equation (4.7) can be estimated by linear fitting of the phase errors (similar to the 2D KICT method described in Chapter 3) or nonlinear fitting of the complex image values. Once the error parameters are known, the correction can be done following Equation (4.8). In the following section, we will discuss and compare the two phase error estimation methods.

4.4.1 Linear Fitting of the Phase Errors

This algorithm is an extension of the KICT algorithm to address the 3D DWI data. Similar to the KICT algorithm for 2D, the slopes and the constant offset of the linear phase errors

are estimated from the phase difference of the $b \neq 0$ navigator image and the $b = 0$ navigator image by performing three 1D linear fittings of the phase difference in x, y, and z direction. The correction is then done by shifting the affected k-space trajectory and multiplying the affected k-space data with the estimated constant phase offset. Correction is done for individual shots and individual z encoding lines. Figure 4.8 illustrates the estimation of the linear phase error parameters from the navigator data.

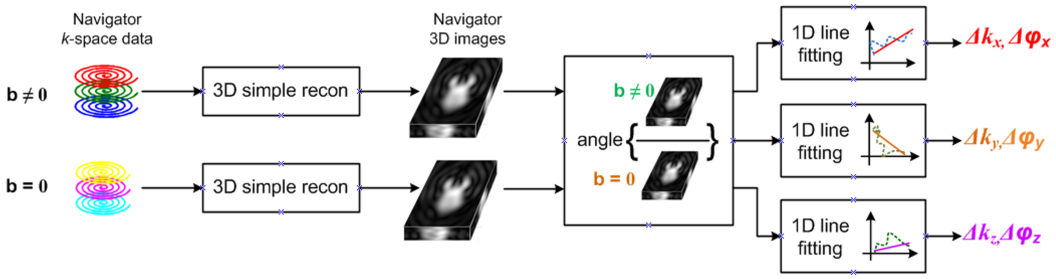

Figure 4.8: Rigid-body motion-induced phase error estimation from navigator data.

4.4.2 Nonlinear Fitting of the Complex Image Values

Assuming that nonlinear phase can be reduced negligibly using cardiac-triggering, and eddy-current effects are minimal with the employment of TRSE, the navigator images can be modeled as

$$\begin{aligned} I_0^{nav}(x,y,z) &= A_0^{nav}(x,y,z)\exp(j\phi_0(x,y,z)) \\ I_b^{nav}(x,y,z) &= A_b^{nav}(x,y,z)\exp\left[j(\phi_0(x,y,z)+c_0+c_1x+c_2y+c_3z)\right] \end{aligned} \tag{4.9}$$

With further assumption that the noise is white additive Gaussian, the maximum likelihood (ML) estimate for $\{c_0, c_1, c_2, c_3\}$ is obtained by minimizing the following cost function:

$$R(c_0,c_1,c_2,c_3) = \left\| I^{nav}(x,y,z) - A_b^{nav}\exp\left[j(\phi_0(x,y,z)+c_0+c_1x+c_2y+c_3z)\right]\right\|_F^2 \tag{4.10}$$

where $I^{nav}(x,y,z) = A_b^{nav}(x,y,z)\exp(j\phi(x,y,z))$ is the measured diffusion-weighted navigator image, and $\|\cdot\|_F$ is the Frobenius norm.

This formulation corresponds to a nonlinear least squares (NLLS) optimization problem, which does not generally have a closed-form solution. Furthermore, minimization of $R(c_0, c_1, c_2, c_3)$ is a nonconvex problem (with multiple local optima). However, with proper initialization, the global minimizer is achievable. The minimization is performed using a standard iterative Newton descent-based algorithm available in MATLAB (The MathWorks, Natick, MA).

A good initialization for the minimization of $R(c_0, c_1, c_2, c_3)$ can be obtained from the location and phase of the navigator k-space data point with maximum amplitude. The reason is that the k-space data point with maximum amplitude corresponds to the shifted k-space center. Therefore, the distance from the shifted k-space center to the point $k_x = k_y = k_z = 0$ gives an estimation of k-space shifts, and the phase of the shifted k-space center gives an estimation of the constant k-space phase offset. Initializations for c_0, c_1, c_2, c_3 are nothing but the estimated k-space shifts scaled by 2π. Initialization for c_0 is simply the estimated k-space phase offset.

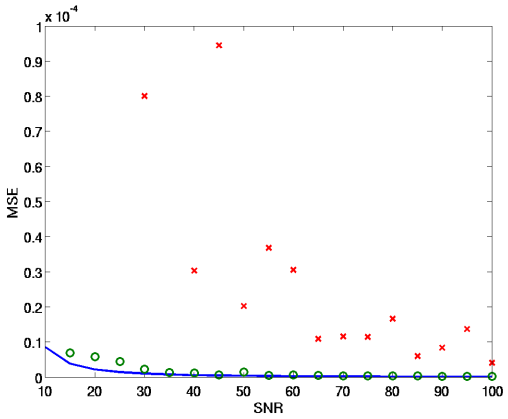

Figure 4.9: Comparison between theoretical bounds (CRLB) and empirical MSE for the phase error estimation. The solid line indicates the CRLB while the circles and crosses represent the empirical MSE from the estimation using linear fitting and NLLS fitting, respectively.

A simulation study was done to compare the performance of the two algorithms in the presence of noise. Figure 4.9 shows a comparison of the Cramer-Rao lower bound (CRLB) [98,99] and mean square error (MSE) of the simulation study for a k-space shift estimation. The

simulated k-space shifts are uniformly distributed in $\mathscr{U}(-5/FOV, 5/FOV)$. Complex Gaussian noise with a range of different variance was added to the images. The NLLS estimation is asymptotically efficient (i.e., unbiased and with MSE matching the CRLB when SNR is high). The linear fitting algorithm becomes more robust as the SNR increases.

Given the performance of the NLLS estimation of the phase error, the KICT algorithm for 3D (and for future 2D studies) will utilize this routine for obtaining the shot-by-shot k-space shifts and phase offsets.

4.5 Peripheral Gating

The proposed motion-induced phase correction algorithm can correct for phase variations among the different shots originating from rigid body motion. However, it cannot correct for phase variations among shots, and signal intensity drop-out within a single-shot, induced by tissue deformation. This is particularly problematic in areas with increased blood and CSF pulsation. Therefore, a multishot acquisition of the whole brain requires, in general, the use of cardiac gating. In a cardiac gated acquisition, k-space data from different shots and different z-encoding lines of a slab are acquired at similar points in a cardiac cycle and therefore experience either the same pulsation motions or are acquired during a quiescent period. Pulsation-induced phase errors then can be conveniently ignored since they are consistent among all shots. Furthermore, if the data acquisition is restricted to only quiescent duration of the cardiac cycle, signal loss can also be minimized [46, 87].

Previous studies have shown that different parts of the brain experience different amounts of pulsation [100]. With a multislab acquisition, we can assign slabs that are more sensitive to pulsation (slabs at the brain stem level) to the most quiescent parts of the cardiac cycle. Other slabs that are less sensitive to pulsation (upper part of the brain) can be acquired at any time. A similar gating strategy was proposed previously for 2D acquisitions [100]. Previous studies have also shown that the quiescent duration of a cardiac cycle in the level of the pons occurs immediately after the R peak and has duration of approximately 300 ms [28]. Some other studies have shown mid-brain cardiac gated images that are quite free of pulsation effects with the trigger delays of up to 500 ms [46]. In the present study,

the sequence time is 150 ms and data acquisition is done during the 450 ms interval right after the R peak (three slabs per R-R interval). With the employed interleaved six-slab acquisition, slices from the first two slabs covering the lower part of the brain are acquired during the first 150 ms of the cardiac cycle. Slices from the next two slabs covering the mid brain are acquired during the second 150 ms of the cardiac cycle. And slices from the last two slabs covering the upper part of the brain are acquired during the third 150 ms of the cardiac cycle. With this strategy, lower brain and mid-brain are acquired during the most quiescent periods of the cardiac cycle and therefore are less prone to pulsation.

4.6 Image Reconstruction

Since the trajectory used in the navigator data is a single-shot stack-of-spirals, navigator data reconstruction is fast and simple by taking 1D FFT along the stack direction (k_z direction) and gridding in (k_x, k_y) plane. The trajectory used for image data is also stack of spirals, but due to the need for high resolution data a multishot trajectory is used. However, the motion-induced phase correction introduces shifts to the trajectory for each shot and results in varied trajectory shifts for the overall image acquisition. Therefore, reconstruction of corrected image data requires either 3D gridding or iterative methods. Difficulties in computing the sample density of an arbitrary 3D trajectory hinder the usage of 3D gridding. The conjugate gradient algorithm with the use of nonuniform Fourier transform object [93,94] is used instead in order to solve the iterative 3D reconstruction problem without the need for sample density compensation. For parallel imaging reconstruction, sensitivity encoding (SENSE) [85] with reduction factor of both 1 and 2 was used in the *in vivo* data.

4.7 *In Vivo* Measurement

A diffusion-weighted spin-echo sequence with navigators (4.1) was implemented on a Siemens (Erlangen, Germany) TIM Trio 3 T system. Healthy volunteers were scanned with a 12-channel head coil for whole brain coverage in accordance with the Institutional Review Board of the University of Illinois at Urbana-Champaign. The imaging parameters were: FOV =

$24 \times 24 \times 14.4$ cm^3, voxel size $1.88 \times 1.88 \times 2$ mm^3. A trajectory composed of a stack of six-shot constant density spirals, corresponding to a total readout time of 11.28 ms, was used for image acquisition.

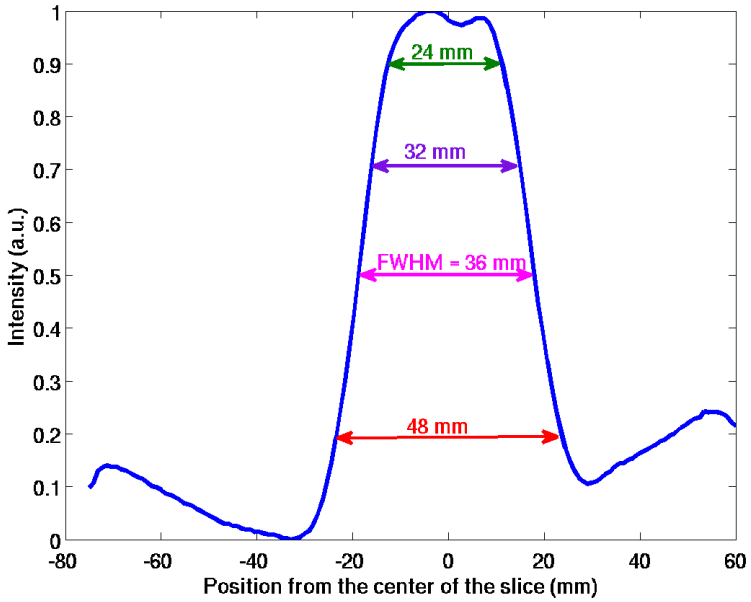

Figure 4.10: Slab selection profile and the oversampling, overlapping strategy for minimizing the boundary effects. The chosen parameters are: slab thickness of 32 mm, oversampling factor of 1.125, overlapping factor of 25%. The resulting signal intensity variation across the slab after truncation of the overlapping is $< 22\%$.

From the results of SNR analysis, the 3D imaging volume was divided into six slabs to obtain the optimum SNR efficiency. To cover the whole human brain with six slabs, 24-mm slabs are needed. Oversampling and overlapping of slabs are done to mitigate the slab boundary artifacts. Figure 4.10 shows the measured slab selection profile and the parameters of choice. The actual slab thickness (32 mm) was chosen so that the maximum signal intensity variation across the slab after truncation of the overlapping is $< 10\%$, resulting in an overlapping factor of 25%. Oversampling by a factor of 1.125 was chosen so that the full width half max (FWHM) of the slab selection profile is fully encoded. The resulting maximum aliasing intensity inside the 24-mm slabs is $< 20\%$.

A 3D navigator was realized by a stack of low resolution single-shot constant density

spirals. The 3D k-space coverage of the navigator determines the maximum k-space shifts that the navigator can detect. K-space shifts detected with a 2D self-navigated variable density spiral in three different human subjects have a maximum value of $5/FOV$. Therefore, a k-space data matrix size of $15 \times 15 \times 10$ is a reasonable choice.

Diffusion encoding was employed on six non-colinear directions. Diffusion preparation was either non-eddy-current-compensated or eddy-current-compensated using modified TRSE scheme [83]. Diffusion-weighting parameters for the noncompensated sequence were: $\delta =$ 24 ms, $\Delta = 35$ ms, and $G_{max} = 30$ mT/m, corresponding to a b-value of 1000 s/mm^2. Corresponding echo time for image data and navigator data were TE1 = 64 ms, and TE2 = 105 ms, respectively. When eddy-current compensation was enabled, due to the high insensitivity of the modified TRSE scheme to misadjustment (Figure 4.6(c)), the diffusion parameters were chosen to achieve the minimum possible TE and minimum total residual eddy current due to any misadjustment while maintaining the b-value. Matching the non-compensation scheme above, the parameters for the modified TRSE scheme were: $\delta_1 = 17$ ms, $\delta_2 = 9$ ms, $\delta_3 = 14$ ms, $\delta_4 = 12$ ms. The resulting TEs are: TE1 = 66 ms, TE2 = 107 ms.

Peripheral gating was used with a zero trigger delay to reduce the sensitivity of the acquisition to tissue motion caused by blood and CSF pulsation. The use of cardiac gating is important since the employed motion-induced phase error correction algorithm assumed rigid body motion and cardiac gating reduces considerably physiologically induced nonrigid body motion [47]. With the above mentioned sequence parameters, the sequence time T_{seq} was approximately 150 ms, which allows the acquisition of three slabs during the quiescent period ($\sim$ 500 ms) of an R-R interval.

Data were obtained both with and without parallel imaging (using a reduction factor of 2). When parallel imaging was enabled, $b = 0$ images were still fully encoded for extracting the sensitivity maps that were needed in the parallel imaging reconstruction using SENSE [85].

For comparison a 2D acquisition with the same resolution ($1.88 \times 1.88 \times 2$ mm^3) was carried out. The trajectory used was a 10-shot variable density spiral [86] to match the readout duration of the 3D case and enable self-navigation for motion-induced phase error correction [47]. To reduce the total scan time and to minimize the effect of the gross motion

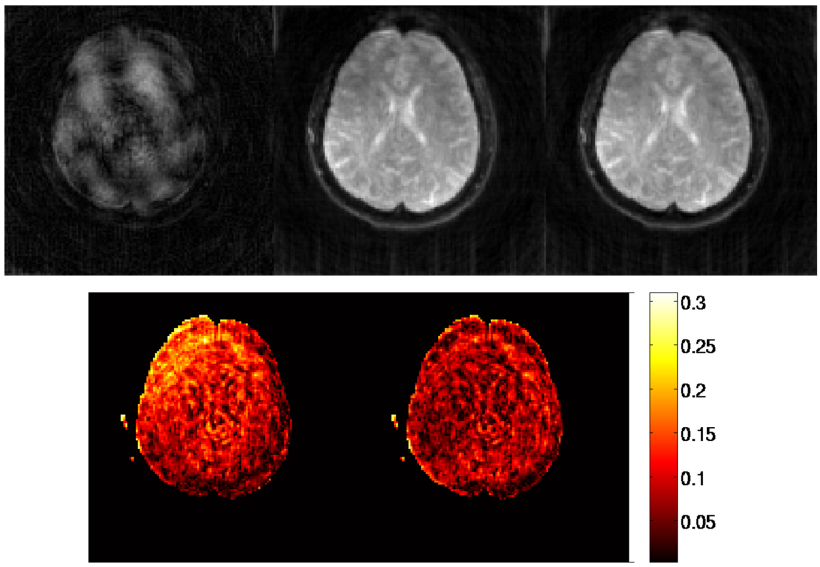

Figure 4.11: Performance of motion-induced phase error correction algorithms on simulation data: uncorrected (left panel (a)), corrected with phase error parameters estimated by linear fitting (middle panel (a)), and nonlinear fitting (right panel (a)). The corresponding normalized error of each algorithm is given in (b) with linear fitting on the left panel and nonlinear fitting on the right panel.

in the 2D acquisition, only 18 slices on the level of corpus callosum were acquired.

4.8 Results

4.8.1 Simulations

The performance of motion-induced phase error correction algorithms was examined using a 3D $b = 0$ image as a numerical phantom. The matrix size of the numerical phantom was $128 \times 128 \times 16$. Random, motion-induced phase errors were applied to individual shots and corresponded to constant phase offsets uniformly distributed in the interval $(-\pi, \pi)$ and k-space shifts uniformly distributed in the interval $(5/FOV, 5/FOV)$. Navigator data for motion-induced phase error estimation were simulated with a k-space matrix size of $15 \times 15 \times 10$.

Figure 4.11(a) shows reconstructed images with and without motion-induced phase error correction. The uncorrected image is highly corrupted by the errors. The corrected image

restores the simulated phantom. The normalized error shows the superiority of the nonlinear fitting error parameter estimation over the linear fitting (Figure 4.11(b)). Besides the possible incomplete phase error estimation and correction, the residual errors are also related to the locally undersampled k-space trajectory due to linear phase errors that result in k-space shifts that can leave localized regions of k-space inadequately sampled.

A simulation study was done to examine the dependence of the performance of the two error estimation algorithms on the size of the navigator. Mean square estimation errors of the k-space shifts and k-space phase-offset were computed for randomly generated linear phase. The offsets of the linear phases were uniformly distributed in the interval $(-\pi, \pi)$, corresponding to the constant phase offset in the interval $(-\pi, \pi)$. The slopes of the linear phases were uniformly distributed in the interval $(-10\pi/FOV, 10\pi/FOV)$, corresponding to k-space shifts in the interval $(-5/FOV, 5/FOV)$, the range of k-space shifts measured in *in vivo* data. The set of the examined navigator matrix sizes $(N_{nav_x}x, N_{nav_y}, N_{nav_z})$ is: [(5, 5, 5); (10, 10, 5); (10, 10, 10); (15, 15, 10); (15, 15, 16); (20, 20, 16); (40, 40, 16); (128, 128, 16)].

As shown in Figure 4.12, both algorithms start giving small estimation error when the navigator matrix size is at least $(N_{nav_x}, N_{nav_y}, N_{nav_z}) = (15, 15, 10)$. For a navigator trajectory composed of a stack of constant density spirals, with the matrix size of (15, 15, 10), the k-space FOV of the navigator is a cylinder with the height going from $k_z = -5/FOV$ to $k_z = 4/FOV$ and with a circle cross section of radius $7/FOV$. Therefore, any shifts in k_x, k_y, k_z that are bounded in the interval (-5/FOV, 5/FOV), and their combinations are detectable by this navigator, yielding small estimation errors. This navigator matrix size of (15, 15, 10) was used in our *in vivo* acquisition and gave reliable error estimation and correction results.

From Figure 4.12, nonlinear fitting performs better than linear fitting when the navigator size is small. However, linear fitting outperforms nonlinear fitting with large navigator matrix sizes. Notice that noise is not added into this simulation study.

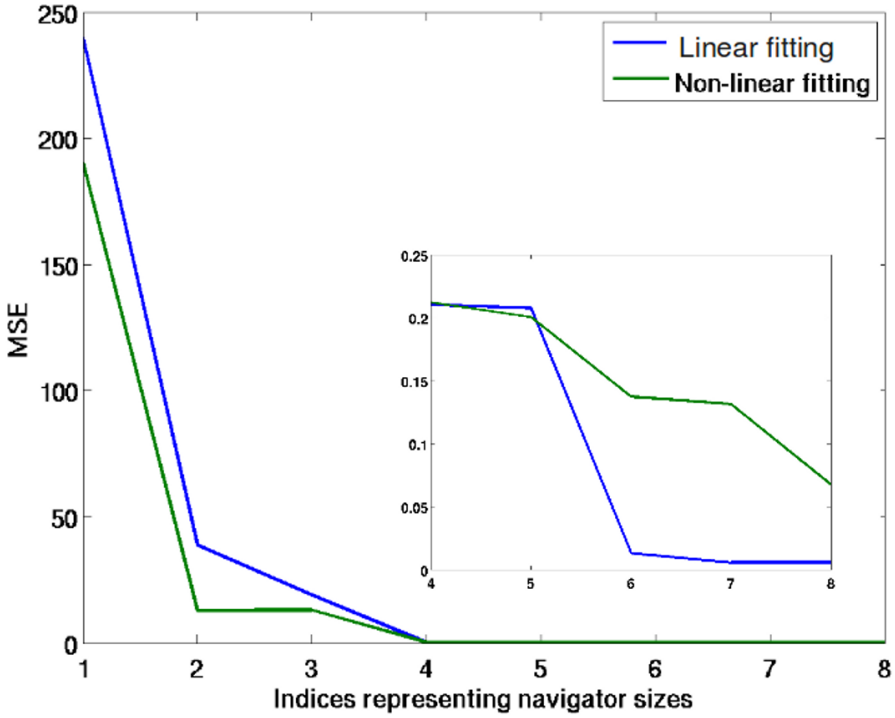

Figure 4.12: Performance of the navigator. The values on x axis are the indices of an array of 3D navigator matrix sizes (x, y, z): [(5, 5, 5); (10, 10, 5); (10, 10, 10); (15, 15, 10); (15, 15, 16); (20, 20, 16); (40, 40, 16); (128, 128, 16)]. Note that the image matrix size is $128 \times 128 \times 16$. Smaller figure is the expansion of the part of the plot from navigator size corresponding to indices from 4 to 8.

4.8.2 Phantom

A phantom study was done to test the effectiveness of the eddy-current compensation acquisition. To eliminate the effect of motion-induced phase error, an agar phantom was used. The protocol parameters for the eddy-current-compensated and noncompensated acquisitions are listed in Section 4.7.

Figure 4.13 shows the computed variance of image intensity across six different diffusion encoding directions using

$$V(r) = \frac{\sqrt{\sum_{n=1}^{N} (I_n(r) - \overline{I(r)})^2}}{\sqrt{N-1}\overline{I(r)}} \tag{4.11}$$

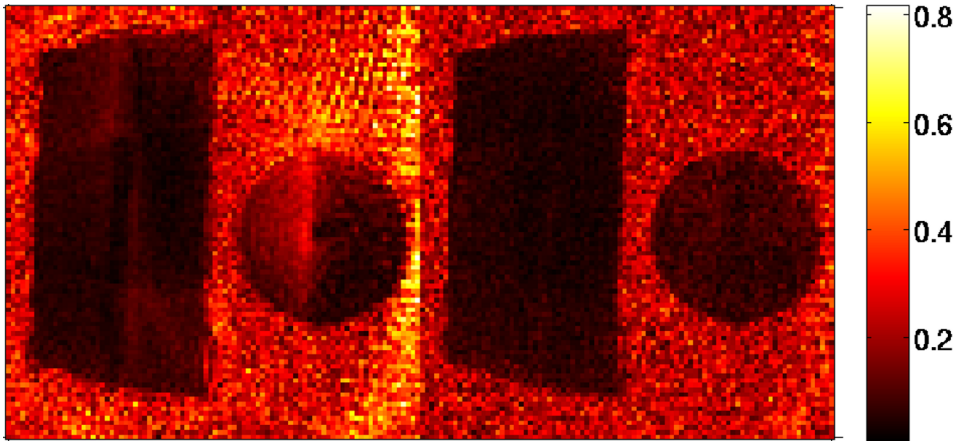

Figure 4.13: Normalized variance of the image intensity across six different diffusion encoding directions when noncompensated (left panel) and eddy-current-compensated (right panel) acquisitions are used.

where $I_n(r)$ is the individual diffusion-weighted image, and $\overline{I(r)} = \frac{\sum_{n=1}^{N} I_n(r)}{N}$ is the mean of all diffusion-weighted images.

Since the diffusion in the phantom is isotropic, the high variation in the variance of the images obtained with noncompensated acquisition indicates residual eddy currents. The variance is low and uniform in the images acquired with eddy-compensated sequence showing the effectiveness of the compensation strategy employed.

4.8.3 *In Vivo*

Representative images reconstructed with and without motion-induced phase error correction are shown in Figure 4.14. Even with padded head support and a cardiac-gated acquisition, significant artifacts and signal loss due to motion-induced phase errors were observed in uncorrected images (Figure 4.14(a)). These images lack adequate quality for examination of diffusion metrics. Three-dimensional KICT restored signal loss and removed motion-induced phase artifacts from the uncorrected images giving high-quality 3D high-resolution diffusion-weighted images (Figure 4.14(b, c)). Correction with phase error parameters estimated using nonlinear fitting (Figure 4.14(c)) is overall better than correction with phase error parameters

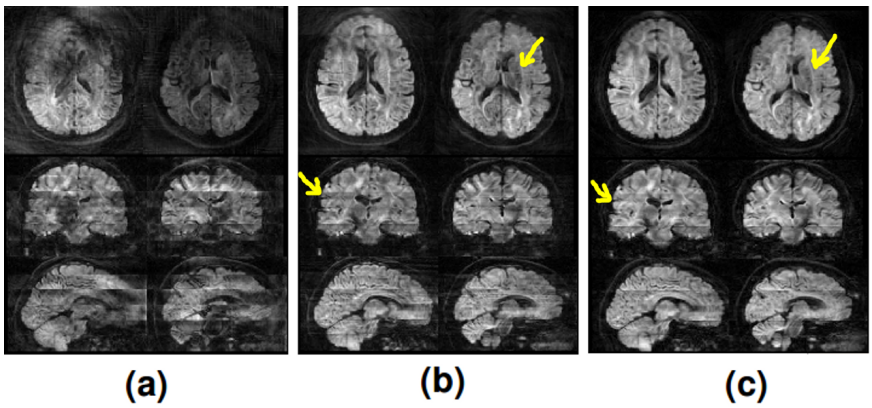

Figure 4.14: Diffusion-weighted images of two subjects: (a) uncorrected, (b) corrected with 3D KICT using linear fitting for error parameter estimation, (c) corrected with 3D KICT using nonlinear fitting for error parameter estimation. Different columns correspond to different subjects. Different rows correspond to different views (axial, coronal, sagittal) of the 3D images. $b = 1000$ s/mm^2 and voxel size = 1.88 x 1.88 x 2 mm^3. SENSE with reduction factor of 1 was used.

estimated using linear fitting (Figure 4.14(b)) as pointed out by the arrows. Some of the slab boundary artifacts are still visible but they are not severe and do not interfere significantly with the diffusion metrics. A larger overlapping factor between adjacent slabs can be used to further reduce the boundary artifacts but at a cost of increasing the total scan time. Because the boundary artifact is consistent through all of the images, its effects on the derived diffusion metrics were minimal (shown below in fractional anisotropy maps).

To compare 3D multislab and 2D acquisitions, we also acquired 18 2D slices on the level of corpus callosum with the same resolution and echo time as in the 3D multislab acquisition. The repetition time TR of the 2D acquisition cannot be matched to the TR of the 3D acquisition due to the restriction of maximum number of acquisitions per RR interval. Furthermore, for the 2D acquisitions, a 10-shot variable density spiral trajectory was used to take advantage of the self-navigated capability in optimizing motion-induced phase error correction. The readout durations of 2D and 3D acquisition are matched, yielding similar reactions to magnetic susceptibility. To give a quantitative assessment of the two acquisition schemes, we compute the SNR of the $b = 0$ images reconstructed from fully sampled data of

a single coil

$$SNR = \sqrt{\frac{4-\pi}{2}} \frac{\overline{I_{ROI_{in}}}}{\sigma_{ROI_{out}}} \tag{4.12}$$

where $\overline{I_{ROI_{in}}}$ is the average signal in a region of interest within the imaging object (ROI_{in}), and $\sigma_{ROI_{out}}$ is the standard deviation of the noise in a region of interest outside the imaging object (ROI_{out}) [88]. The factor is the correction factor for the change in the noise variance after the magnitude operation [88, 101, 102]. The reason is that noise in a zero-signal region is normally distributed around zero ($n \sim \mathcal{N}(0, \sigma^2)$); therefore, its magnitude has a Rayleigh distribution with parameter σ and hence the variance $\frac{4-\pi}{2}\sigma^2$. Without the correction factor, the SNR will be overestimated.

Table 4.1: SNR comparison between 2D and 3D multislab acquisition.

	Subject 1	Subject 2	Subject 3
3D multislab	94.14	109.57	92.94
2D	31.95	42.60	35.34
3D multislab/2D	2.94	2.57	2.63
Theoretical 3D multislab/2D	2.74	2.74	2.74

Using Equation (4.12), the computed SNRs for 2D and 3D multislab acquisition for three subjects are given in Table 4.1. The three-dimensional multislab acquisition gives a gain from 2.57 to 2.94 in SNR as compared to 2D acquisition. These measured SNR gains agree well with the theoretical SNR gain of a factor of 2.74. Notice that this theoretical gain is smaller than the theoretical gain given in Figure 4.2(b) by a factor of $\sqrt{10/6}$ since the 2D acquisitions use a 10-shot variable density spiral while 3D multislab acquisition uses a six-shot constant variable density spiral with similar readout durations.

Three-dimensional FA maps, and color-coded FA maps derived from the obtained diffusion-weighted images for two subjects are shown in Figure 4.15 and Figure 4.16. In color-coded FA maps, red encodes left/right, green encodes anterior/posterior, and blue encodes superior/inferior orientation for the primary eigenvector of the diffusion tensor. The obtained FA maps and color-coded FA maps show the superiority of the phase error parameter estimation

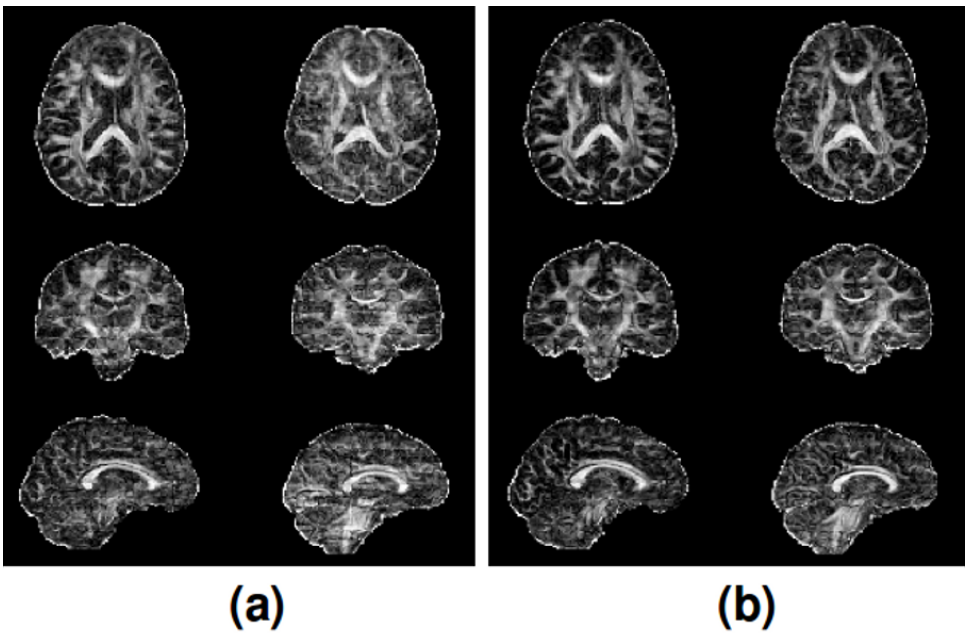

Figure 4.15: FA maps of two subjects obtained with DTI data corrected using parameters estimated with linear fitting (a) and nonlinear fitting (b). Each column corresponds to one subject. Each row corresponds to different view (axial, coronal, sagittal). $b = 1000$ s/mm^2 and voxel size = 1.88 x 1.88 x 2 mm^3. No parallel imaging was used.

using nonlinear fitting over linear-fitting, giving much cleaner FA maps and color-coded FA maps (Figure 4.15(b) and Figure 4.16(b)). FA maps at $1.88 \times 1.88 \times 2$ mm^3 resolution were successfully obtained. The corticospinal tract running superior-inferior between the cerebral cortex and the spinal cord is well resolved. Small fibers in the cerebellum are also visible. As stated earlier, the slab boundary artifacts, although visible in the diffusion-weighted image, have only minor effects in the derived FA maps.

For comparison, the FA maps and color-coded FA maps from the 2D data set are also shown in Figure 4.17. Because of the difficulty in aligning the 2D volume and the 3D volume, the slices shown in Figure 4.17 are only approximately at the same positions at those shown in Figure 4.15 and Figure 4.16. Hence the FA maps between the two figures are slightly different. Although the fibers are reasonably resolved in the 2D case, the 2D FA maps are noisier than those in the 3D case.

Parallel imaging was incorporated in our data acquisition and image reconstruction. The total scan time for six-direction DTI when using parallel imaging with a reduction factor

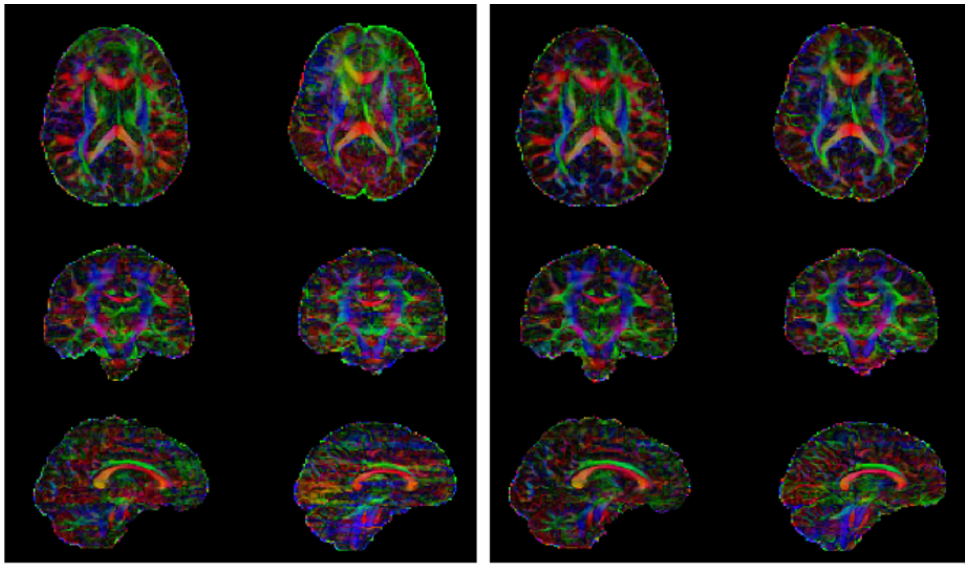

Figure 4.16: Color-coded FA maps of two subjects obtained with DTI data corrected using parameters estimated with linear fitting (a) and nonlinear fitting (b). Each column corresponds to one subject. Each row corresponds to different view (axial, coronal, sagittal). $b = 1000$ s/mm^2 and voxel size = 1.88 x 1.88 x 2 mm^3. No parallel imaging was used.

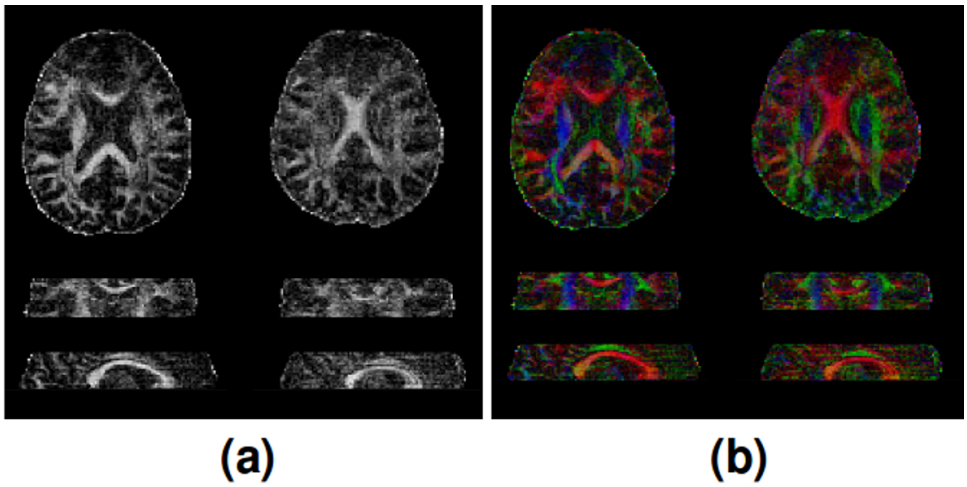

Figure 4.17: (a) 2D FA maps, (b) 2D color-coded FA maps of two subjects. Each column corresponds to one subject. Each row corresponds to different view (axial, coronal, sagittal). $b = 1000$ s/mm^2 and voxel size = 1.88 x 1.88 x 2 mm^3. No parallel imaging was used.

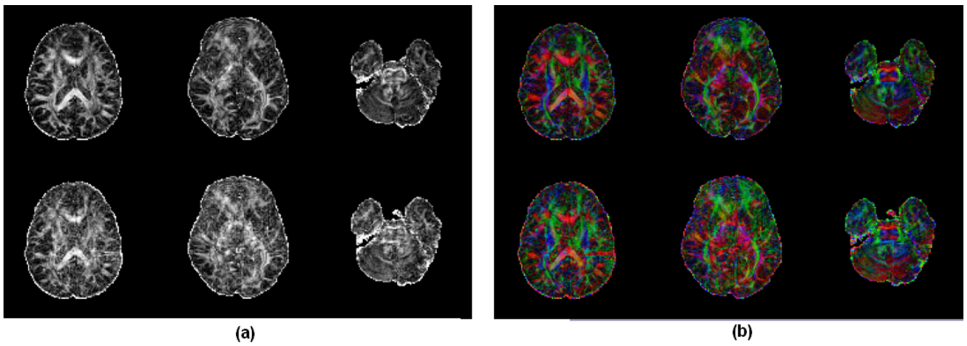

Figure 4.18: (a) FA maps, (b) color-coded FA maps of one subject. First row corresponds to SENSE with reduction factor of 1, second row corresponds to SENSE with reduction factor of 2. b = 1000 s/mm^2, voxel size = 1.88 x 1.88 x 2 mm^3.

of 2 was 14.4 minutes on subjects with an R-R interval of $\sim$ 1 s. Figure 4.18 shows the obtained FA maps and color-coded FA maps when SENSE with reduction factor of 1 and 2 was used. While FA maps of adequate quality were achieved with SENSE factor of 1, the quality of FA maps when SENSE factor of 2 was used was partially compromised due to the possible local undersampling in k-space resulting from both motion-induced phase errors and the reduction factor in parallel imaging.

4.9 Discussion

The need to detect small brain lesions and to reduce partial volume effects in the derivation of diffusion-metrics has made high resolution 3D diffusion-tensor imaging (DTI) a research focus in diffusion acquisition methodology. The most important benefit of 3D DTI over 2D DTI is the potential for achieving higher SNR at higher spatial resolutions and/or higher b-value. However, 3D DTI is limited by multiple challenges that must be addressed prior to its widespread implementation. These challenges include longer total acquisition time, higher sensitivity to more complicated motion-induced phase errors, and possibly more complicated image reconstruction algorithms.

The current study shows the feasibility of obtaining high resolution 3D whole brain DTI within reasonable scan time by employing an optimized multislab acquisition technique. The

presented method avoids the engagement of a complicated diffusion signal model as in DW-SSFP studies [68–70, 103–105] or the challenging phase stability requirements as in fast spin echo diffusion imaging study [71]. The multislab approach has been recently proposed in combination with different 3D DTI acquisition techniques [66, 67, 106, 107]. However, to the best of our knowledge, the current study is the first to provide a thorough analysis of the time and SNR tradeoffs of 3D multislab acquisition, and to efficiently combine interleaved multislab acquisition with cardiac-gating. The presented arguments are general and the proposed interleaved multislab acquisition with cardiac-gating can be applied to any type of diffusion prepared sequence.

Another general novel feature of the proposed method is the employed motion correction algorithm. Due to the long data readout times, 3D full brain DTI is usually acquired with multishot techniques. Therefore, it is crucial that a robust motion-induced phase error correction algorithm can be used to reconstruct the data. Multiple efficient algorithms exist for motion-induced phase error correction in 2D [36, 37, 41–45, 47]. However, extension of many of these algorithms to 3D is nontrivial and can result in impractical image reconstruction times [65]. Therefore, previous studies resort to either 2D correction [71], constant phase offset correction [105], or k-space center-based error estimation and correction [68]. The 3D motion-induced phase error correction algorithms proposed in the current study are truly 3D and relatively time-efficient. However, the total image reconstruction time is long due to the resulting truly 3D non-Cartesian trajectory. Without any parallelization, the total reconstruction time for a 128 x 128 x 96 volume is 40 minutes on a 2.66 GHz Intel Core 2 CPU. This reconstruction time is still significantly shorter than the 24 hours required for a 128 x 128 x 128 volume with 3D combined phase error correction (included as a sensitivity profile) and conjugate gradient reconstruction; and the 1-3 hours required for a 128 x 128 x 128 volume with 3D direct phase subtraction correction and hybrid gridding [65]. Due to the multislab and multidirection structure of the data, parallelization by a factor of $N_{slab} \times N_{direction}$ is trivial and can be implemented on a cluster or with GPUs, yielding significant speedups. For the data at hand, with parallelization, the total reconstruction time for a six-direction DTI could be potentially reduced to 6.6 minutes. Further optimization on parallelization of the reconstruction would be necessary prior to routine use.

Several potential advancements could further refine the proposed technique. These include compensation for locally undersampled k-space data, 3D navigator matrix size, correction susceptibility effects, and further improvement and analysis of slab boundary artifacts.

The occurrence of locally undersampled k-space data is the result of linear motion-induced phase errors and reduction factor in parallel imaging. From the obtained results, the effects of local undersampling are not severe when parallel imaging with reduction factor of 1 is used. For reduction factor greater than 1, higher tolerance to the local undersampling problem can be obtained by using a stack of variable density spiral trajectory with more oversampling in the center of k-space at the cost of more severe magnetic susceptibility artifacts due to the longer data acquisition readout durations.

With the current navigator matrix size of 15 x 15 x 10 and careful head restraint methods, the motion-induced phase error estimation and correction performs reliably on every set of *in vivo* data. However, when restraint methods are not possible (body imaging, imaging patients), larger navigator size might be necessary. Maximum navigator matrix size is limited by the echo time of the navigator. Since the motion-induced errors observed by different receiver coils are the same, parallel imaging can be used to increase the matrix size of the navigator without increasing its echo time.

Although off-resonance effects are not severe with the current set of imaging parameters (total readout duration of 11.28 ms), they have to be taken into account for a more robust acquisition, especially in the case of DTI acquisitions at higher resolution, or with higher oversampling trajectory. A separate field map acquisition or a low resolution spiral-in acquisition with modified echo time can be added in the refocusing part of the first spin echo in $b = 0$ acquisition to give a field map measurement for later correction. A similar technique with the latter was used in a multiecho acquisition in [108].

Slab boundary artifacts are still visible in some of our diffusion-weighted images. However, because these artifacts are in general highly distinct from possible disease-related anomalies, the obtained images may not lose their diagnostic value. Because of the consistency of the slab boundary artifacts, the derived diffusion metric maps do not suffer significantly. If a higher overlapping factor between adjacent slabs is used, the boundary artifacts can be further reduced. However, to cover the same volume, the total scan time will increase. Slab

boundary artifact can also be minimized by a more careful design of RF pulse with stricter constraints in the side lobes.

In conclusion, we successfully obtained whole brain 3D pulsed gradient spin echo DTI with the resolution of $1.88 \times 1.88 \times 2$ mm^3 and showed that a 3D multislab acquisition is the optimal strategy for high signal-to-noise high-resolution DTI. This technique will allow for improved visualization of detailed white matter structures with complex geometries.

CHAPTER 5

MAGNETIC SUSCEPTIBILITY CORRECTION FOR 3D DIFFUSION TENSOR IMAGING

5.1 Sampling Density of Diffusion-Weighted Imaging in the Presence of Motion-Induced Phase Errors

Rigid-body motion during the diffusion encoding period of a diffusion-weighted acquisition leads to shifts in k-space trajectory and phase offsets in the k-space data [36]. While the effects of phase offsets can be completely removed provided that a reasonably good estimation of the phase offsets is available, the effects of k-space shifts cannot be completely eliminated. The reason is that the shot-dependent motion-induced k-space shifts can cause a fully sampled multishot k-space to become locally undersampled, leading to aliasing.

Figure 5.1(a) shows the effects of motion-induced phase error on the sampling density compensation (the inverse of the sampling density) of a 2D constant density spiral k-space trajectory. The sampling density compensation is computed by performing a Voronoi decomposition on the k-space points and calculating the inverse of the area of the resulting polygons. Sampling density compensation of > 1 indicates undersampling. Under the effects of MiP, the resulting k-space can be locally undersampled. Therefore, even when the exact k-space shifts are known, the corrected image can still be corrupted (Figure 5.1(b)).

To overcome this local undersampling problem, either parallel imaging or a trajectory designed with oversampling (such as variable density spiral) is used. When total scan time is a limiting factor, as in the case of 3D spin-echo DTI, parallel imaging is commonly used to speed up the acquisition and a reduction factor of more than 1 is generally employed. Even with parallel imaging, high reduction factor together with motion-induced undersampling can still result in aliasing as shown in Figure 4.18.

An example of using an oversampled trajectory to minimize the undersampling problem is

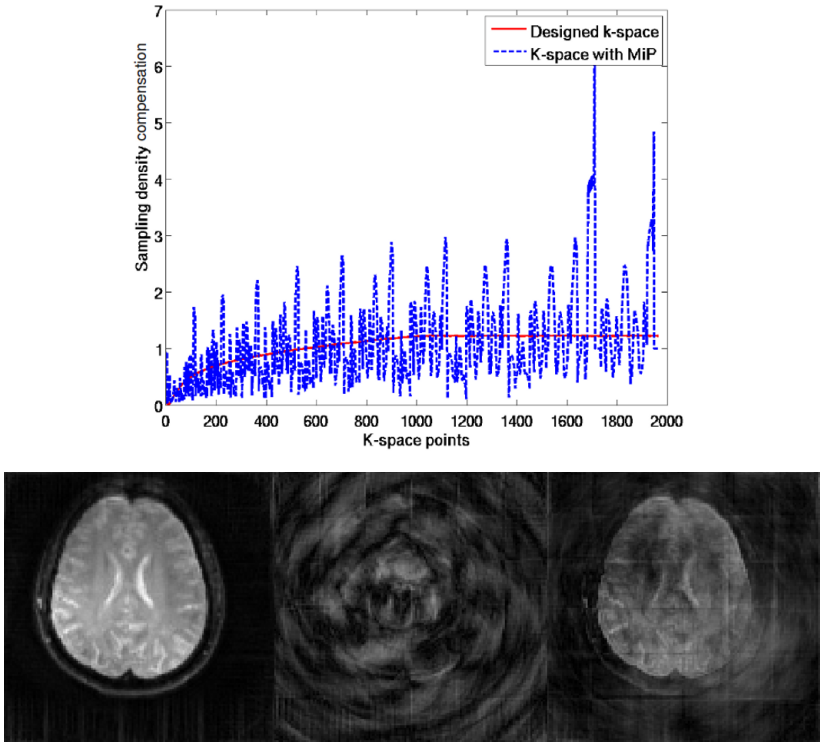

Figure 5.1: (a) Effect of motion-induced phase errors on the k-space sampling density. The solid red line indicates the sampling density compensation of the designed (2D constant density spiral) k-space trajectory. The dash blue line indicates the sampling density compensation of the k-space trajectory corrupted by motion-induced phase error. (b) Motion-induced local undersampling leads to aliasing in the corrected image even though the exact MiP is known. The left panel shows the original image, the middle panel shows the image corrupted by MiP, and the right panel shows the image corrected with the exact MiP parameters.

given in Figure 5.2. Similar MiP to that in Figure 5.1(b) was applied to the data simulated on a variable density spiral trajectory. The variable density spiral trajectory helps recover the residual aliasing. However, using an oversampled trajectory while maintaining the total scan time leads to longer readouts and hence more severe susceptibility artifacts. Therefore, in this chapter we aim to apply magnetic susceptibility correction to 3D DTI images acquired with variable density spiral trajectory to facilitate parallel imaging with reduction factor > 1 (and hence a reduction in total scan time) while maintaining limited magnetic susceptibility artifacts.

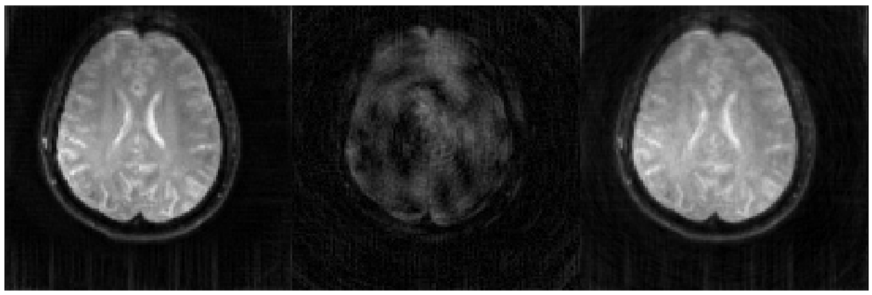

Figure 5.2: Variable density spiral can be used to reduce motion-induced local under-sampling. The left panel shows the original image, the middle panel shows the image corrupted by MiP, and the right panel shows the image corrected with the exact MiP.

5.2 Magnetic Susceptibility Correction for 3D DTI

As reviewed in Chapter 2, the receiver signal under magnetic susceptibility artifact can be expressed as

$$\begin{gathered} y(t_m) = \int f(\vec{r}) \exp\left(j\omega_s(\vec{r})t_m - j2\pi\vec{k}(t_m)\cdot\vec{r}\right)\mathrm{d}\vec{r} \\ m = 0, 1, \cdots, M-1 \end{gathered} \tag{5.1}$$

Assume that the object and field map can be parameterized using a set of basis functions so that

$$\begin{aligned} f(\vec{r}) &\approx \sum_{n=0}^{N-1} f_n \phi_f(\vec{r} - \vec{r_n}) \\ \omega_s(\vec{r}) &\approx \sum_{n=0}^{N-1} \omega_n \phi_\omega(\vec{r} - \vec{r_n}) \end{aligned} \tag{5.2}$$

Assuming $\phi_f(\vec{r}) = \phi_\omega(\vec{r}) = \phi\vec{r}$ and replacing Equation (5.2) into Equation (5.1), we have

$$\begin{gathered} y(t_m) \approx \Phi(k(\vec{t_m})) \sum_{n=0}^{N-1} f_n \exp\left(j\omega_n t_m - 2\pi k(\vec{t_m})\cdot\vec{r_n}\right) \\ m = 0, 1, \cdots, M-1 \end{gathered} \tag{5.3}$$

where $\Phi(\cdot)$ is the Fourier transform of the basis function $\phi(\cdot)$. With noise consideration and the parameterization, Equation (5.3) can be expressed in matrix form as

$$\mathbf{y} = \mathbf{A}\mathbf{f} + \epsilon \tag{5.4}$$

where $\mathbf{y} = [y(t_0)\ y(t_1)\ \cdots\ y(t_{M-1})]^T$ is the vector of the measured signal, $\mathbf{f} = [f_0\ f_1\ \cdots\ f_{N-1}]^T$ is the vector of the object's coefficients, ϵ is the vector of complex noise, and $\mathbf{A}$ is an $M \times N$ matrix with entries

$$a_{m,n} = \Phi(k(t_m)) \exp\left(j\omega_n t_m - j2\pi k(\vec{t_m}) \cdot \vec{r_n}\right) \tag{5.5}$$

Assuming that the noise is additive white Gaussian, an efficient estimation of $\mathbf{f}$ is given by minimizing the cost function

$$\Psi(\mathbf{f}) = \frac{1}{2}\|\mathbf{y} - \mathbf{A}\mathbf{f}\|^2 \tag{5.6}$$

The computation of $\mathbf{Af}$ for solving the minimization problem in Equation (5.6) is time-consuming due to the field inhomogeneity term and the non-Cartesian characteristic of the k-space trajectory. To speed up the reconstruction time, a combination of nonuniform fast Fourier transform (NUFFT) and time-segmented field inhomogeneity correction was applied [81, 93].

The iterative reconstruction algorithm using NUFFT and time-segmented field inhomogeneity correction proposed by Sutton et al. [81] can be summarized as follows. With the assumption that the phase accrual due to field inhomogeneity is approximately constant during a short time interval τ, the total acquisition time is partitioned into L time segments of width τ. The phase accrual is then computed as $L+1$ break points and interpolated between these break points for an approximation at intermediate time points. More specifically, $\exp(j\omega_n t)$ is approximated as

$$\exp(j\omega_n t) \approx \sum_{l=0}^{L} a_l(t) \exp(j\omega_n l\tau) \tag{5.7}$$

where $a_l(t)$ is the min-max interpolation coefficient of the l^{th} break point for the time point t. With this time segmentation, the discretized signal equation in Equation (5.3) becomes

$$\begin{gathered} y(t_m) \approx \Phi(k(\vec{t_m})) \sum_{l=0}^{L} a_l(t_m) \sum_{n=0}^{N-1} \left[f_n \exp(j\omega_n l\tau) \right] \exp\left(- j2\pi k(\vec{t_m}) \cdot \vec{r_n} \right) \\ m = 0, 1, \cdots, M-1 \end{gathered} \tag{5.8}$$

Therefore, the measured signal $y(t_m)$ is the weighted sum of the Fourier transform of $f_n \exp(j\omega_n l\tau)$ which can be computed quickly using NUFFT.

5.3 *In Vivo* Measurement

A diffusion-weighted spin-echo sequence with navigators as in Figure 4.1 was implemented on a Siemens (Erlangen, Germany) TIM Trio 3 T system. Healthy volunteers were scanned with a 12-channel head coil for whole brain coverage in accordance with the Institutional Review Board of the University of Illinois at Urbana-Champaign. The imaging parameters were: FOV = $24 \times 24 \times 14.4$ cm^3, voxel size $1.88 \times 1.88 \times 2$ mm^3. Two types of trajectory were used to assess the magnetic susceptibility correction, and the possibility of increasing the reduction factor in parallel imaging under the effect of MiP by increasing the sampling density of the k-space trajectory used. The first trajectory is a stack of six-shot constant density spirals, corresponding to a total readout time of 11.28 ms. The second trajectory used is a stack of six-shot variable density spirals with oversampling factor $\alpha = 4$ [86], corresponding to a total readout time of 20 ms.

The rest of the parameters are similar to those used in the previous chapter. Multislab acquisition with six slabs was used. The slab thickness was 32 mm, oversampling factor was 1.125, and overlapping factor was 25%. 3D navigator was realized by a stack of low resolution single-shot constant density spirals with k-space data matrix size of $15 \times 15 \times 10$. Diffusion encoding was employed on six non-colinear directions. Diffusion-weighting parameters were: $\delta = 24$ ms, $\Delta = 35$ ms, and $G_{max} = 30$ mT/m, corresponding to a b-value of 1000 s/mm^2, an echo time of 64 ms for imaging data, and an echo time of 105 ms for navigator data. Parallel imaging with reduction factor of 1 and 2 was employed. Peripheral gating was also used for eliminating the motion-induced phase error from pulsation.

5.4 Results

Figure 5.3 shows the 3D susceptibility correction results on $b = 0$ images and the field maps used in the correction. The number of time segments used in the reconstruction

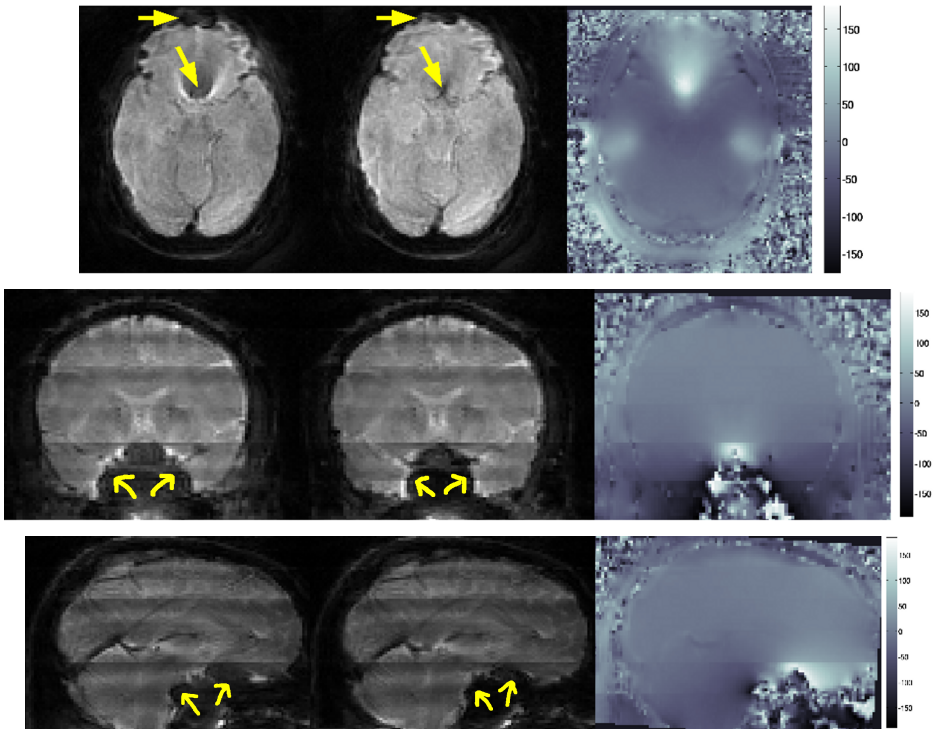

Figure 5.3: Susceptibility correction in 3D. In each of the sub-figures, the first panels correspond to uncorrected images acquired with variable density spiral trajectory (readout duration of ~ 20 ms), the second panels correspond to susceptibility corrected version of the first panel, and the third panels correspond to the accompanied field map in Hz.

was 7 and was chosen in consideration of both the field map amplitude and reconstruction time. Without correction, the images are heavily distorted (as shown by the yellow arrows in Figure 5.3(a), 5.3(b), 5.3(c) first panels) in the areas with high field map amplitude. The correction significantly reduces the distortion and reveals features that are lost in the uncorrected images.

The purpose of using an oversampled trajectory with longer readout duration in 3D DTI is to enable the employment of parallel imaging with reduction factor > 1 for acceleration. Figure 5.4 shows the achieved FA maps and color-coded FA maps with parallel imaging reduction factor of 1 (first column in each panel) and 2 (second column in each panel) on data acquired with constant density spiral trajectory (first row in each panel) and with variable density spiral trajectory (second row in each panel). High quality FA maps and color-coded FA maps were achieved for data acquired with both trajectory when the reduction factor is 1. However, when reduction factor of 2 was used, images acquired with constant density

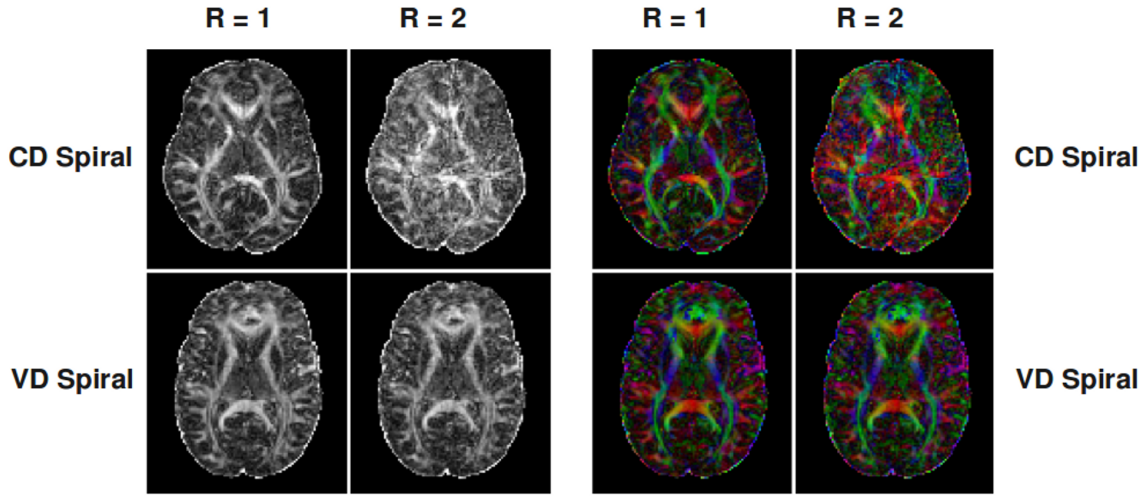

Figure 5.4: FA maps (left panel group) and color-coded FA maps (right panel group) with parallel imaging reduction factor of 1 (first column in each panel group) and reduction factor of 2 (second column in each panel group). First row of both groups are data acquired with a stack of constant density (CD) spiral trajectory. Second row of both groups are data acquired with a stack of variable density (VD) spiral trajectory.

spiral trajectory show residual aliasing artifact while those acquired with variable density spiral trajectory do not. Therefore, under MiP effects, higher sampling density trajectory is required for parallel imaging with similar maximum reduction factor as in the case of no MiP.

5.5 Discussion

Motion-induced phase errors occurring in multishot diffusion-weighted imaging lead to undersampled trajectory and therefore limit the maximum reduction factor used in parallel imaging. To enable the use of parallel imaging for reductions in total scan time, this chapter proposed to oversample the data using a higher density trajectory and correcting for the more severe magnetic susceptibility distortion resulting from a longer readout duration. *In vivo* data have shown the capability of the 3D magnetic susceptibility correction algorithm in restoring image quality. High-resolution, aliasing-free FA maps and color-coded FA maps were achieved with parallel imaging with reduction factor of 2 on data acquired with a four-

channel head coil, reducing the total acquisition time of a $1.88 \times 1.88 \times 2$ mm^3, six-direction, cardiac-gated, spin-echo DTI to 14.4 minutes on subjects with 1 s R-R interval.

The primary purpose of the study in this chapter is to achieve 3D DTI of the whole brain in the shortest time. Besides using parallel imaging for speeding up like the method proposed in this chapter, shorter total acquisition time can be achieved by reducing the total number of shots used in the multishot acquisition while maintaining the same sampling density at the cost of reasonable increases in the readout duration. Similar to the proposed method, magnetic susceptibility correction is required for obtaining artifact-limited images.

Reconstruction time is definitely a challenge for the current method. With seven time segments, the reconstruction time for one volume of the current acquisition is 10 hours on a 2.66 GHz Intel Core 2 CPU with 8 GB memory. However, due to the multislab, multidirection, and multisegment structure of the data, parallelization by a factor of $N_{slab} \times N_{direction} \times L$ is trivial and can be implemented on a cluster or with GPUs yielding significant speed-ups.

The field map used in the current correction is acquired from a separate scan, and therefore registration is needed and the total acquisition time is increased by 4 minutes. For a completely registered field map at no additional acquisition time, a low resolution spiral-in acquisition with modified echo time can be added in the refocusing part of the first spin echo in $b = 0$ acquisition to give a field map measurement for later correction; a similar technique was used in a multiecho acquisition by our group in [108].

In conclusion, speeding-up of the 3D DTI acquisitions using parallel imaging was made possible by the employment of a high sampling density trajectory together with a 3D magnetic susceptibility correction method. To the best of our knowledge, this study is the first study to achieve 3D DTI full brain *in vivo* at the resolution $1.88 \times 1.88 \times 2$ mm^3 within 15 minutes. The most recent achievement on 3D DTI with full brain coverage was the study by Jung et al. [68], in which a 6-direction 3D DTI at the resolution of 1.88 isotropic was obtained within 18 minutes using 3D radial sampling trajectory and diffusion-weighted SSFP acquisition.

CHAPTER 6

THREE-DIMENSIONAL SUBMILLIMETER DIFFUSION TENSOR IMAGING

Signal-to-noise ratio (SNR) is one but not the only factor that limits the achievable resolution of *in vivo* DTI and MRI in general. Due to T2 relaxation, field inhomogeneity, off-resonance effects, motion, and the need to keep a practical scan time, the readout duration and total acquisition time are limited, which in turn limits the resolution.

Up to now, we have developed an acquisition technique and accompanying post-processing algorithms for achieving $1.88\times1.88\times2\text{mm}^3$ 3D DTI with full brain coverage. Further increase to submillimeter resolution in full brain study is difficult because of the constraints in readout duration and realistic total scan time. However, in studies of fine neuronal architectures such as the human pons (approximately $40 \times 40 \times 30$ mm^3 in size), or the human hippocampus ($50 \times 8 \times 8$ mm^3 in size), submillimeter resolution is needed for sufficient delineation of the underlying structures.

If SNR is sufficient and only a specific localized anatomy is of interest, a reduced field-of-view (rFOV) approach is the strategy of choice for diffusion tensor imaging with submillimeter resolution since it enables a reasonable readout duration (limited artifacts) as well as a realistic *in vivo* acquisition time.

As reviewed in Chapter 2, many techniques have been introduced in previous studies for rFOV DTI, but most of them have been focused on 2D acquisitions. In the present chapter, a new technique combining rFOV with 3D DTI is developed to first exploit the SNR efficiency of 3D acquisitions and finally give submillimeter resolution DTI in localized structures without sacrificing the resolution in the z-encoding direction.

6.1 Three-Dimensional Reduced Field-of-View Acquisition

Reduced-field-of-view (rFOV) acquisition is necessary when imaging with submillimeter resolution to reduce sensitivity to various artifacts including but not limited to off-resonance, magnetic susceptibility, eddy currents, and $T2^*$ blurring while maintaining a reasonable total scan time. However, by limiting the field-of-view (FOV), the SNR of the resulting images is reduced. Therefore, unless there is sufficient SNR to trade for a smaller FOV, the benefits from the rFOV acquisition are compromised by the need to perform multiple averages.

Three-dimensional acquisition is, most of the time, a preferred strategy over two-dimensional acquisition for high resolution imaging with sufficient SNR. However, as discussed in Chapter 4 because of the interleaving capability of 2D acquisitions and a required minimum repetition time TR for T1 relaxation, 3D acquisitions usually result in longer scan time than 2D acquisitions. Therefore, in terms of SNR efficiency (the ratio between SNR and the square root of total scan time), 3D acquisition is not always superior to its 2D counterpart. Interestingly, for diffusion imaging, the need for cardiac-gating to mitigate the pulsation-induced phase error and signal loss significantly limits the 2D interleaving, closing the gap in the acquisition time difference between 2D and 3D and putting 3D acquisitions in an advantageous position.

As an illustration, Figure 6.1 shows the SNR efficiency comparison between 3D and 2D acquisitions for different numbers of slices when cardiac-gating is used. The calculation in Figure 6.1 uses Equation (4.4) in Chapter 4 with T1 and T2 for white matter at 3 T (1081 ms and 69 ms respectively). Due to the realization of rFOV, which requires either multiple regional saturation blocks or a long multidimensional RF pulses, the minimum sequence time is long enough to allow only two repetitions (two 2D interleavings) in the quiescent period ($\approx$ 500 ms) of each cardiac cycle. For 3D acquisition, the duration between two consecutive excitations of the volume (TR) is set to two cardiac cycles to allow sufficient time for T1 recovery. Without loss of generalization, the calculation also assumes that 3D is realized by performing Cartesian encoding in the third dimension and that 2D and 3D have the same in-plane encoding.

From Figure 6.1, the 3D acquisition is always more efficient than the 2D acquisition when

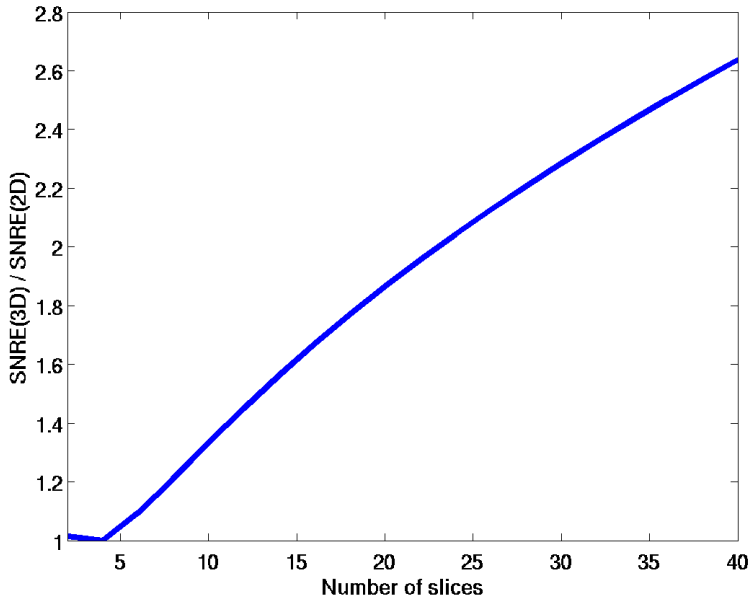

Figure 6.1: SNR efficiency comparison between 3D and 2D acquisitions. The plot shows the ratio between the SNR efficiency of 3D acquisition and the SNR efficiency of 2D acquisition. SNR efficiency is computed as the ratio between the SNR and the square root of the total acquisition time.

the total number of slices is larger than 4. For example at 20 slices, the SNR efficiency ratio between 3D and 2D is 1.865, meaning if the total scan time of 3D and 2D acquisitions is matched, 3D acquisition gives 1.865 times higher SNR than 2D acquisition. Therefore, as long as the total acquisition time per volume for 3D acquisition is not too long, 3D acquisition is definitely the method of choice for cardiac-gated DTI.

6.2 Imaging Localized Neuronal Structures

6.2.1 The Human Pons

The pons is one of the seven main parts of the central nervous system [109] with the function of conveying information about movement from the cerebral hemisphere to the cerebellum where force, range of movement and motor skill learning are modulated. The adult human pons constitutes a region of significant neuroradiologic interest and consists predominantly of

mylinated axons, nuclei and vasculature. DTI studies of this region can be extremely helpful for purposes of diagnosis, surgical planning, and intraoperative neuronavigation, for example, in patients with tumors or arteriovenous malformations. The compact histoarchitecture of the brain stem is characterized by a formidable network of basilar artery perforators, microvessels perfusing the intricate neuronal tracts, and draining veins. Because of the multiple tracts and cranial nerves located in the pons, the neurosurgeon would be greatly helped by a DTI method that could resolve these structures and their relationship to tumors or vascular malformations [28]. High-resolution DTI of the pons/brain stem has been done previously [28, 32, 64] with the smallest voxel size of $1.0 \times 1.0 \times 1.5$ mm^3. To the best of our knowledge, submillimeter voxel size has not been attempted *in vivo*

6.2.2 The Human Hippocampus

The human hippocampus is among the most well-studied structures in the brain because of its important functional role in memory processing and learning, its remarkable neuronal cell plasticity, and its involvement in epilepsy and neurodegenerative disease processes [110].

Microstructural organization of the hippocampus is becoming increasingly interesting as a physiological indicator in a variety of memory function studies related to mild cognitive impairment (MCI) and Alzheimer's [111, 112] and even in normal encoding of declarative memory [113]. Our interest in the hippocampus is motivated by the findings that the entorhino-hippocampal circuit, including the perforant pathway, is among the first temporal structures affected by neurofibrillary tangles and that the pathology in these structures correlates with both the onset and the degree of dementia as a person ages [114,115]. Therefore, the integrity of the entorhino-hippocampal circuit may be an important biomarker for Alzheimer's disease and other age-associated neurodegenerative disorders.

The hippocampus is a multilaminar structure ($50 \times 8 \times 8$ mm^3 in size) that is divided into the hippocampus proper (with three subdivisions CA1, CA2, and CA3), the dentate gyrus, subiculum, presubiculum, parasubiculum, and entorhinal cortex [116]. A schematic drawing and a color fiber-orientation map of a human hippocampus [117] is given in Figure 6.2.

Unlike the neocortex, connections that link the various parts of the hippocamus are unidi-

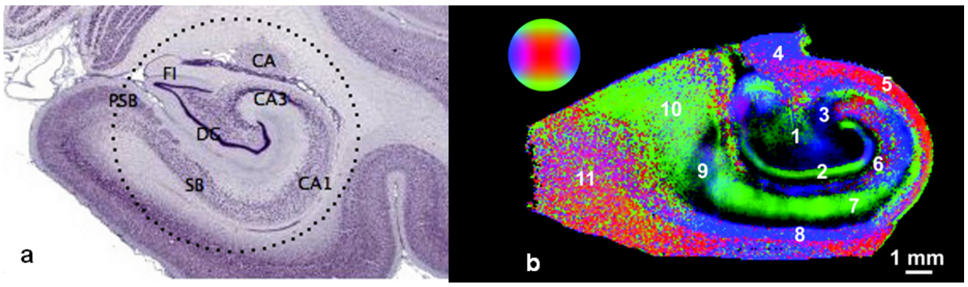

Figure 6.2: Human hippocampus: (a) schematic drawing (from Wikipedia), (b) color fiber orientation map from [117]: color intensity is proportional to the FA value, color value encodes directions (transverse: blue, vertical: green, through the image plane: red). The numbers encode the substructures of the hippocampus: 1, hilus (dentate gyrus); 2, molecular layer; 3, stratum lucidum; 4, fimbria; 5, alveus; 6, stratum lacunosum-moleculare; 7, stratum radiatum/pyramidale; 8, stratum oriens; 9, presubiculum; 10, subiculum; 11, white matter. Note: due to copyright issues, this figure might be eliminated from the final version of the dissertation.

rectional. The entorhinal cortex can be considered the first step in the intrinsic hippocampal circuit. Cells in the superficial layers of the entorhinal cortex give rise to axons that project to, among other destinations, the dentate gyrus through the perforant pathway. The principal cells of the dentate gyrus then give rise to axons called mossy fibers that connect with pyramidal cells of the CA3 field of the hippocampus proper. The CA3 pyramidal cells, in turn, are the source of the major input to the CA1. The CA1 then projects unidirectionally to the subiculum. Both the CA1 and the subiculum project to the entorhinal cortex, closing the hippocampal processing loop.

In the hippocampal circuit, the perforant pathway (PP) is an extremely important tract of neuronal fibers since it is the unique input to the hippocampus. Sensory information from multiple association areas throughout the brain is relayed at the entorhinal cortex (EC) and then transmitted by the PP to the hippocampus, from where it is distributed to intralimbic neuronal circuits [118–120]. It is widely assumed that during the course of Alzheimer's disease, the destruction of the PP constitutes a major pathophysiological event, resulting in a severe disconnection of limbic regions from sensory input to the brain [114, 118, 119]. However, until now only a few studies attempted to detect PP changes *in vivo* [111].

High resolution DTI offers an excellent tool for assessing the microstructural alterations in

nerve fibers and hence is a suitable method for imaging the hippocampus, more specifically the PP.

High-resolution DTI of the hippocampus has been done previously [31,117,121]. However, only an *ex vivo* study performed at high magnetic field used sub-millimeter resolution in all x, y, z directions ($60 \times 60 \times 300$ μm^3) [117]. For an *in vivo* acquisition, tradeoffs between resolution, SNR, and scan time have to be considered. Because the region of interest is just the hippocampus, a smaller FOV can be prescribed to reduce the total scan time. However, smaller FOV and higher resolution lead to lower SNR. Therefore, in 2D DTI studies the through-plane resolution is usually sacrificed to reduce the loss in SNR, leading to acquisitions with relatively thick slices (3-5 mm).

In the present project, we propose to combine 3D imaging with reduced FOV imaging to obtain submillimeter in-plane resolution DTI without sacrificing resolution in the slice direction and with similar acquisition time and SNR as those in our previous 2D work on high resolution DTI [28, 31].

6.3 *In Vivo* Measurements

6.3.1 Common Imaging Parameters

The combination of outer-volume suppression (OVS) and 3D stack of multishot variable density spiral was implemented in the current study for 3D reduced-field-of-view (rFOV) acquisition with the target resolution of $0.8 \times 0.8 \times 1$ mm^3.

OVS is chosen to realize rFOV imaging firstly because of its simple implementation. Secondly, the OVS technique allows us to maintain a short echo time (much shorter than using multidimensional RF pulse) since the saturation occurs during the preparation period. As compared to ZOOM, OVS is more compatible with multislab imaging, which is a necessary extension when large coverage in the third dimension is required (for example imaging of the spinal cord).

Four regional saturation bands of 110 mm thickness are used to suppress the signal from outside of the desired in-plane FOV as shown in Figure 6.3. We rely on the slab selective

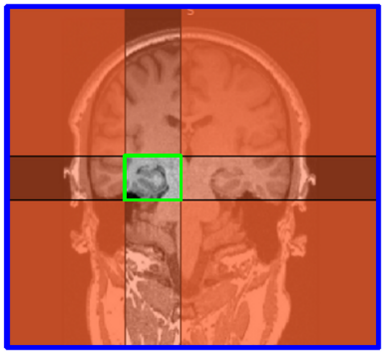

Figure 6.3: Reduced field-of-view realization with regional saturation. The green box represents the reduced field-of-view.

profile to suppress the signal from outside of the desired through-plane FOV.

For imaging localized structures that are close to the center of the receiver coils (for example the brain stem, the pons, or the spinal cord), parallel imaging is not effective in handling the undersampling problem due to low variability in sensitivity profiles. Multi-shot diffusion imaging, however, is prone to undersampling due to motion-induced phase errors. Therefore, a variable density spiral trajectory with oversampling factor $\alpha = 4$ [86] is used. The number of shots is chosen so that the resulting readout time is less than 20 ms for limiting off-resonance, magnetic susceptibility, and eddy current artifacts while giving the minimum possible total acquisition time. For a FOV of 40 mm, enough to cover the pons and the hippocampus, and in-plane spatial resolution of 0.8×0.8 mm^2, the minimum number of shots that keeps the readout time below 20 ms with sampling time of 5 μs is 6 and the minimum number of shots that keeps the readout time below 15 ms with sampling time of 5 μs is 10. Notice that the spiral trajectory is designed with a maximum gradient amplitude of 23 mT/m and a slew rate of 140 mT/m/ms for avoiding nerve stimulation.

Diffusion encoding parameters are $\delta = 22$ ms, $\Delta = 32$ ms, $G_{max} = 30$ mT/m corresponding to a b-value of 770 s/mm^2. Depending on the type of acquisition used (discussed next), the number of diffusion encoding directions is either 6 or 10. To prevent the pulsation-induced phase error and signal loss, cardiac-gating is used with zero trigger-delay.

A 3D navigator is acquired after every shot and every third dimension encoding line for motion-induced phase error estimation and correction. The resolution for the navigator is

$3.2 \times 3.2 \times 2$ mm^2 and is achieved with a stack of single-shot constant density spiral trajectory.

6.3.2 Speeding Up the Acquisition with Fast Spin-Echos (FSE)

Recall that for sufficient T1 recovery time, the TR for our 3D acquisition is 2 R-R intervals, resulting in a very inefficient acquisition. For an R-R interval of 1 s, the ratio of the data acquisition time to the total time spent is $\frac{20}{2000} = 0.01$. Multislab imaging with the capability of interleaving as proposed in Chapter 4 is a valid choice for improving the acquisition efficiency. However, for small spatial coverage and high resolution in the third dimension, the overhead time for resolving slab boundary artifacts outweighs the gain from interleaving capability. Instead, we propose to use fast spin echo imaging for improving the acquisition efficiency at a cost of a slight decrease in SNR per image.

Fast spin echo (FSE) is an imaging technique in which a series of refocusing pulses is applied after one excitation pulse for the acquisition of multiple k-space lines or shots per TR, hence reducing the total scan time. However, due to the imperfection of the refocusing pulses, magnetization components from different echo paths interfere destructively, leading to severe echo attenuation within the echo train. Due to the phase instability of transverse magnetization resulting from the diffusion preparation, the well-known Carr-Purcell-Meiboom-Gill (CPMG) method [122] for stabilizing the echo train of an FSE sequence does not resolve this instability in this case. Instead, quadratic phase cycling [123] and mixed-CPMG phase cycling [38] were proposed. However, the former method requires an extra preparation period of RF pulses [123] while the latter method can only refocus every four echoes, making themselves suitable only for FSE sequence with echo train length of > 4 [124]. In our current study, we limit the echo train length to 3 (including the navigator echo) in consideration of the resulting decrease in the already moderate SNR per image. Therefore, phase cycling is not a good choice for improving the magnitude of the echo train.

An alternative approach for stabilizing the magnitude of a spin-echo train is to reduce the deviation of the refocusing pulse flip angle from the nominal flip angle. The reason is that if the refocusing pulse is strictly 180^o, then the transverse magnetization will be completely refocused at the echo time regardless of the initial phase. Pell et al. in [125] have proposed to

use a refocusing slice that is wider than the excitation slice for more accurate measurement of T2. By using a wider refocusing pulse, the slice profile in the excitation region is improved, giving a refocusing pulse that is homogeneously close to 180^o.

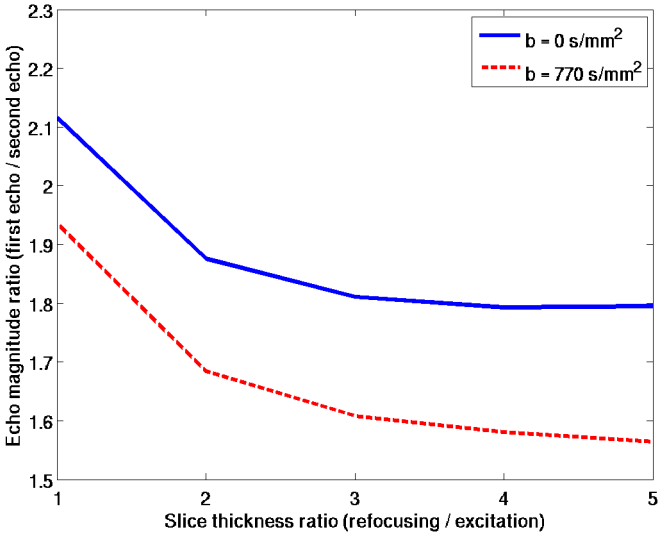

Figure 6.4: Plots of amplitude ratio of the first to the second echoes when the ratio of the selection thickness of the refocusing pulse to excitation pulse changes. The blue line corresponds to $b = 0$ data. The red dash line corresponds to $b = 770$ s/mm^2 data.

A phantom study was done to verify the effectiveness of the slice thickness enlargement method on improving the CPMG condition. Figure 6.4 plots the amplitude ratios of the first to the second echoes with different ratios of the selection thickness of the refocusing pulses to the excitation pulse. When the thickness ratio increases, the difference between the amplitude of the first and second echoes decreases, implying a better refocusing of the magnetization.

When the flip angles of the refocusing pulses deviate from their nominal value of 180^0, undesired spin echoes and stimulated echoes are generated, interfering destructively with the desired echoes. Therefore, in our implementation of the sequence, spoilers around the refocusing pulses are added to suppress the undesired echoes, reducing the interference and hence improving the amplitude of the later echoes in the echo train. In Figure 6.4, diffusion-weighted data have less discrepancy between the amplitude of the first and second echoes

because the large diffusion gradients more effectively cancel any free induction decay (FID) signal generated by the imperfection of the first refocusing pulse, therefore eliminating any echo that can be generated from the FID signal of the first refocusing pulse and reducing interference.

6.4 Image Reconstruction

Due to the imperfections of the regional saturation pulses, residual signals exist outside of the desired FOV that cannot be modeled if we choose to reconstruct only the reduced field of view. To incorporate the incompleteness of the regional saturation pulses into the system modeling, we propose to reconstruct the full FOV image at the cost of being ill-conditioned. Regularization using an energy penalty on the regions outside of the rFOV improves the condition of the reconstruction problem. The cost function of the proposed iterative reconstruction is

$$\Psi(x_{full}) = \|y - Ax_{full}\|^2 + \beta\|x_{full}(mask)\|^2 \tag{6.1}$$

where x_{full} is the image with the full FOV, y is the measured data, A is the encoding matrix, β is the penalty weight, and $mask$ is the mask of the outside of the rFOV of interest.

A simulation study was done to test the performance of the proposed reconstruction method. Figure 6.5 shows a comparison of the reconstruction results obtained with rFOV reconstruction, and full FOV reconstruction with different penalty weights for both complete and incomplete saturation cases. When the saturation is complete, rFOV reconstruction gives a high resolution image well matched with the numerical phantom. Full FOV reconstruction without penalty ($\beta = 0$) and with small penalty ($\beta = 2^4$) give a low resolution image due to early termination of the iterative algorithm. With the same number of iterations but higher penalty ($\beta = 2^8$), meaning more enforcement of the *a priori* knowlegde, the resulting image is of much higher quality. When the saturation is incomplete, rFOV reconstruction fails to give a reasonable image due to the model mismatch. With proper energy penalty, full FOV reconstruction generates a high resolution image with minor in-

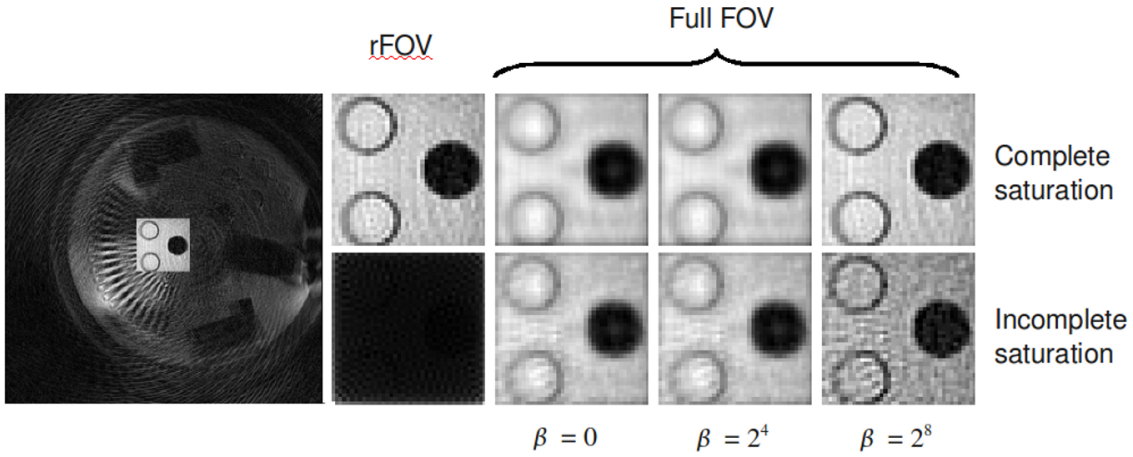

Figure 6.5: Comparison of different reconstruction schemes. The first large panel shows the numerical phantom used in the simulation when the saturation is incomplete. Subsequent panels show the reconstruction results with the parameters as labeled.

coherent aliasing. Therefore, for robust image reconstruction regardless of the saturation performance, full FOV reconstruction with proper energy penalty outside of the rFOV of interest is the method of choice.

6.5 Results

Figure 6.6 shows the obtained high resolution FA maps of the human pons using the single-echo, 3D, rFOV, six-direction DTI acquisition with stack of six-shot variable density spiral trajectory. The results prove the feasibility of *in vivo* submillimeter resolution DTI which includes the success of the acquisition protocol, the correctness of the motion-induced phase error correction algorithm, and the robustness of the reconstruction algorithm. The $0.8 \times 0.8 \times 1$ mm^3 resolution enables the delineation of the pons fiber bundles in all three views (coronal, sagittal, and axial). The total acquisition time is 28 minutes computed with an R-R interval of 1 s.

By carefully incorporating dual spin-echo acquisition with 3D rFOV, without changing the k-space trajectory used, the total acquisition time is reduced by a factor of 2 with a cost of a reduction of 1.2 times in SNR. The time saved through dual spin-echo acquisition can

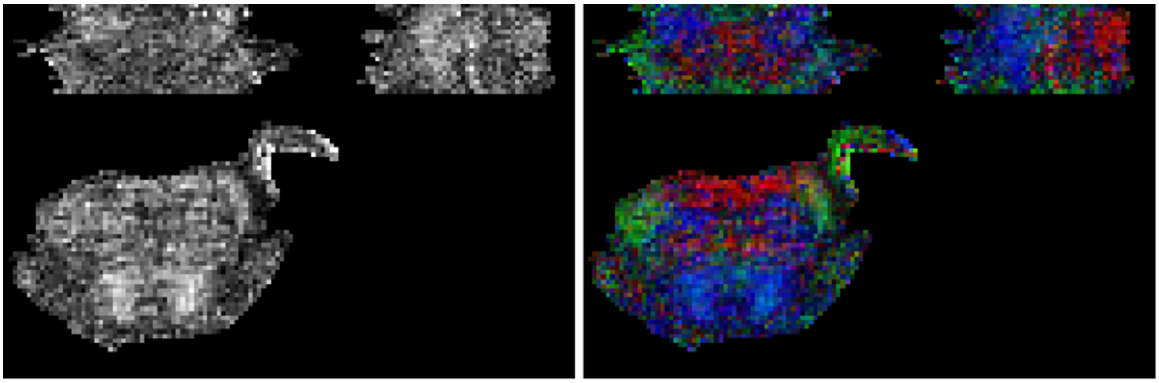

Figure 6.6: Fractional anisotropy (FA) maps of the human pons using single-echo rFOV acquisition at $0.8 \times 0.8 \times 1$ mm^3 resolution. In each panel, the top left image shows a coronal view, the top right image shows a sagittal view, and the bottom image shows an axial view. For the color-coded FA maps (right panel), green encodes anterior-posterior, blue encodes inferior-superior, and red encodes left-right.

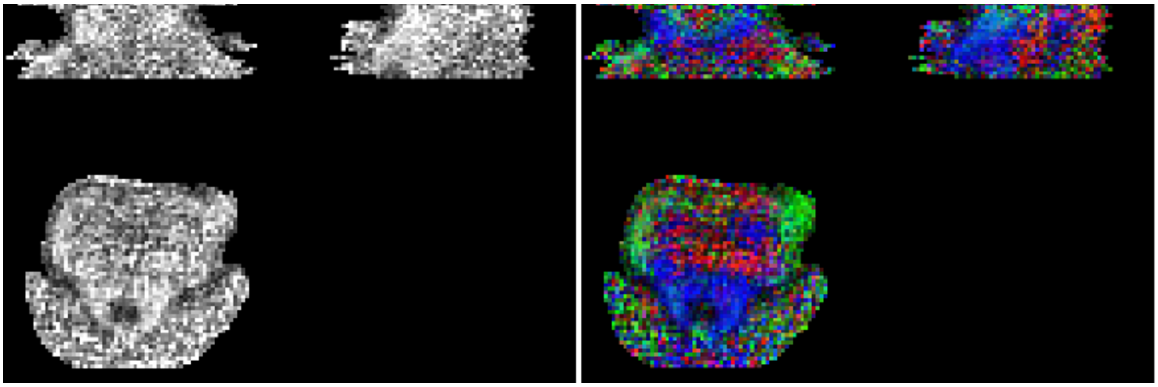

Figure 6.7: Fractional anisotropy (FA) maps of the human pons using dual-echo rFOV acquisition at $0.8 \times 0.8 \times 1$ mm^3 resolution. In each panel, the top left image shows a coronal view, the top right image shows a sagittal view, and the bottom image shows an axial view. For the color-coded FA maps (right panel), green encodes anterior-posterior, blue encodes inferior-superior, and red encodes left-right.

be used to acquire more diffusion-encoding direction, therefore improving the estimation of DTI metrics as shown in Figure 6.7.

Shown in Figure 6.7 are the FA maps of a 10-direction DTI obtained with a total scan time of 22 minutes (assuming R-R interval of 1 s) using dual spin-echo acquisition. The transverse fiber bundles are better delineated with higher FA values.

The proposed acquisition and post processing algorithms were also used to image the

Figure 6.8: Iso-diffusion-weighted image and fractional anisotropy (FA) maps of the human hippocampus using single-echo rFOV acquisition with a stack of six-shot variable density spiral trajectory at $0.8 \times 0.8 \times 1$ mm^3 resolution. In each panel, the top left image shows a coronal view, the top right image shows a sagittal view, and the bottom image shows an axial view. For the color-coded FA maps (right panel), green encodes anterior-posterior, blue encodes inferior-superior, and red encodes left-right.

human hippocampus. Figure 6.8 shows the resulting FA maps and color-coded FA maps of the left hippocampus of a volunteer from a single-echo, six-direction DTI data set acquired with a stack of six-shot variable density spiral trajectory. As compared to the FA maps of the pons, the FA maps of the hippocampus are much noisier due to the primarily grey matter composition of the hippocampus. Nevertheless, the multilayer structure of the hippocampus including fiber bundles running primarily in the left-right direction in the inner part of the hippocampus and running anterior-posterior in the outer part of the hippocampus can be resolved (Figure 6.8).

The time saved by using dual-echo acquisition can either be used to acquire more diffusion encoding directions (like the case of the pons) or to reduce the readout duration and hence reduce the magnetic susceptibility artifacts. Since the hippocampi are located close to air/tissue boundaries, field inhomogeneity is rather high. Reducing the readout duration helps improve the image quality, resulting in enhanced delineation of the hippocampus structure as shown in Figure 6.9.

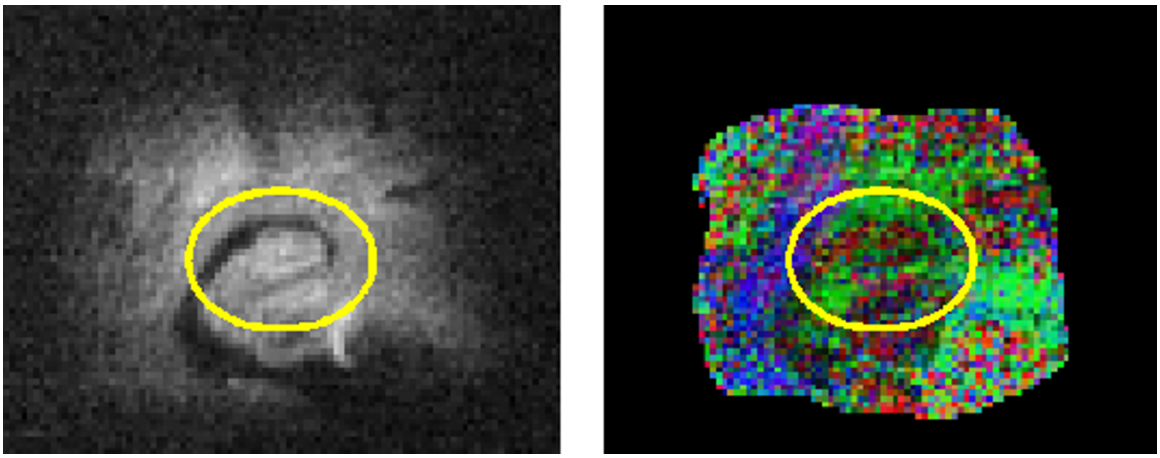

Figure 6.9: Iso-diffusion-weighted image (left) and color-coded fractional anisotropy (FA) map (right) of the human hippocampus (in coronal view) using dual-echo rFOV acquisition with a stack of 10-shot variable density spiral trajectory at $0.8 \times 0.8 \times 1$ mm^3 resolution. For the color-coded FA maps (right panel), green encodes anterior-posterior, blue encodes inferior-superior, and red encodes left-right.

6.6 Discussion

Submillimeter resolution is required for imaging small structures with complex neuronal architectures such as the human pons or the human hippocampus. Due to the requirement of sufficient SNR, limited artifacts and reasonable total scan time, submillimeter resolution DTI can only be achieved with 3D rFOV acquisition. Although the results obtained in the current study are still preliminary, they show the feasibility of the 3D rFOV technique.

Unlike most of the previously developed rFOV techniques that only focus on the implementation of the reduced field-of-view [32, 63, 74, 75], the technique developed in this chapter aims at optimizing the encoding strategy and implementing post-processing algorithms for achieving submillimeter resolution (0.64 mm^3) while maintaining reasonable SNR and reasonable scan time (22 minutes). Therefore, this technique is an important addition to the existing methods.

The techniques developed in this chapter have several limitations. Firstly, even though FSE acquisition with echo train length of 3 is currently used for speeding up the total acquisition, a quantitative analysis of the tradeoff between total acquisition time and the changes in SNR with different echo train length is needed for optimization of the acquisition. Secondly,

when FSE acquisition is used, the difference in the magnitude of the data from every other shot due to T2 decay and incomplete refocusing of magnetization has not been taken into account during reconstruction. Thirdly, the penalty weight β in the proposed reconstruction algorithm is chosen empirically based on visual examination of the resulting images. Therefore, a better choice of β can be made by considering the dependency of the spatial frequency response of the reconstruction algorithm with β. Fourthly, as can be seen from Figure 6.8, the obtained images suffer from severe blurring due to the high field inhomogeneity in the proximity of the hippocampus as well as the relatively long readout duration ($\approx$ 20 ms). Therefore, magnetic susceptibility correction and eddy current compensation are necessary especially when single-echo acquisition is used.

CHAPTER 7

SUMMARY AND FUTURE DIRECTIONS

7.1 Summary of the Contributions

High resolution 3D DTI is highly desired because of its ability to surpass the achievable imaging resolution with standard 2D acquisition techniques. This ability allows investigators to resolve fine-scale neuronal structures, which is of great importance in diagnosing neurodegenerative diseases and forming precise maps of brain connectivity. In this dissertation, we addressed the acquisition, artifact mitigation and correction strategies for achieving three-dimensional high-resolution diffusion tensor imaging.

The main contributions of this dissertation are as follows:

Robust 2D and 3D motion-induced phase error correction algorithm. The most common and severe artifact of multishot DTI is the motion-induced phase error artifact. The developed correction algorithm, named KICT, estimates the error in the image space and performs the correction in k-space . The assumption for the algorithm is rigid-body motion, which is enforced by incorporating cardiac-gating into the acquisition. The phase error estimation is unbiased and approaches the Cramer-Rao lower bound when SNR is sufficient. The correction is time-efficient and robust regardless of the k-space trajectory. The most important impact of KICT is that the algorithm enables 3D DTI.

Three-dimensional multislab DTI acquisition. Three-dimensional high-resolution DTI acquisitions are hindered by the difficulty in achieving subject-tolerable scan time. Without resorting to the complicated DW-SSFP acquisition, the proposed multislab technique in combination with parallel imaging and 3D field inhomogeneity correction enables *in vivo* 3D DTI at $1.88\times1.88\times2$ mm^3 resolution with full brain coverage in 14.4 minutes (computed with an R-R interval of 1 s). The most recent achievement on 3D DTI was at $1.88 \times 1.88 \times 2$ mm^3

resolution acquired with a total scan time of 19 minutes using DW-SSFP [68].

Three-dimensional reduced-field-of-view DTI acquisition. For delineating small and complex structures like the human pons or the hippocampus, 3D reduced-field-of-view submillimeter resolution DTI was developed. Speeding up the total acquisition was facilitated through the use of a fast spin echo acquisition with careful design for minimizing the non-CPMG effects. The image reconstruction algorithm was tuned to address the effects of imperfections in the implementation of the reduced-field-of-view acquisition, i.e. imperfections in the outer volume supression. *In vivo* high resolution DTI of the human pons and the human hippocampus at $0.8 \times 0.8 \times 1$ mm^3 (voxel size of 0.64 mm^3) were achieved within 22 minutes (computed with an R-R interval of 1 s). To the best of our knowledge, the voxel size in the current study is the smallest that has been achieved in *in vivo* DTI.

7.2 Future Directions

7.2.1 Technique Enhancement

3D multislab DTI. The largest overhead of the proposed acquisition technique lies in the slab oversampling and overlapping to reduce the slab boundary artifacts resulting from a poor slab selective profile. Much more efficient acquisition can be achieved by a proper design of the slab excitation and slab refocusing RF pulses, enabling the feasibility of obtaining higher resolution within a tolerable scan time or significantly reducing the total scan time at the same resolution.

The image reconstruction time, especially in the case with field inhomogeneity correction, is a challenge for 3D full brain DTI. However, with the proposed multislab acquisition, and time-segmented field inhomogeneity correction, reduction in image reconstruction time is possible through a parallel implementation of the processing of multiple diffusion-encoding directions, multiple slabs, and multiple time segments through the use of multicore CPUs, compute nodes with graphics processing units (GPUs) or computer clusters.

3D reduced-field-of-view DTI. Improved suppression of signal outside of the chosen field-of-view would improve the quality of the currently proposed acquisition technique. Alter-

natively, other options for imaging only a selected field of view could be examined. The options are the ZOOM technique or multidimensional RF pulses. However, as discussed earlier, the cost of ZOOM is limited compatibility with multislab acquisition. The cost of multidimensional RF pulse is lengthening of the echo time. The impact of the increased echo time will have to be assessed as a tradeoff of improved suppression of signal outside the region of interest.

Field inhomogeneity correction and eddy current compensation will be great additions to the current technique. The performance of post-acquisition correction methods can result in further optimization of the acquisition methods. For example, relatively short data acquisition readouts have been used in the current work to keep field inhomogeneity effects to a minimum. However, further protocol optimizations can result from an analysis of the image quality acquired with longer readouts and reconstructed with field-inhomogeneity-corrected algorithms.

7.2.2 Applications

Since the techniques developed in this dissertation are pushing the resolution of DTI, the applications of these techniques range from the development of early biomarkers of various diseases to improved delineation of the neuronal network connectivity in different anatomical regions (brain, spinal cord, muscle). Currently, we are pursuing two applications. The first application is related to the decline in motor control with age and the change in the diffusion properties of the corticospinal tract. The second application is verifying if the proposed techniques can be used as a tool for early diagnosis of hippocampal diseases by relating the obtained diffusion metrics on the entorhino-hippocampal circuits, including the perforant pathway, with the memory performance on different healthy and aging populations. We expect that higher resolution metrics will more specifically reflect the status of target neuronal pathways, resulting in metrics that have more specific relationships with behavioral decline.

REFERENCES

[1] E. O. Stejskal and J. E. Tanner, "Spin diffusion measurements: Spin echoes in the presence of a time-dependent field gradient," *J Chem Phys*, vol. 42, pp. 288–292, 1965.

[2] K. D. Merboldt, W. Hanicke, and J. Frahm, "Self-diffusion NMR imaging using stimulated echoes," *J Magn Reson*, vol. 64, pp. 479–486, 1985.

[3] D. G. Taylor and M. C. Bushell, "The spatial mapping of translational diffusion coefficients by the NMR imaging technique," *Phys Med Biol*, vol. 42, pp. 345–349, 1985.

[4] D. L. Bihan, E. Breton, D. Lallemand, P. Grenier, E. Cabanis, and M. Laval-Jeantet, "MR imaging of intravoxel incoherent motions: Application to diffusion and perfusion in neurologic disorders," *Radiology*, vol. 161, pp. 401–407, 1986.

[5] D. L. Bihan, J.-F. Mangin, C. Poupon, C. A. Clark, S. Pappata, N. Molko, and H. Chabriat, "Diffusion tensor imaging: Concepts and applications," *J Magn Reson Imaging*, vol. 13, pp. 534–546, 2001.

[6] D. G. Norris, T. Niendorf, and D. Leibfritz, "Healthy and infarcted brain tissues studied at short diffusion times: The origins of apparent restriction and the reduction in apparent diffusion coefficient," *NMR Biomed*, vol. 7, pp. 304–310, 1994.

[7] J. Pfeuffer, W. Dreher, E. Sykova, and D. Leibfritz, "Water signal attenuation in diffusion-weighted ^{1}H NMR experiments during cerebral ischemia: Influence of intracellular restrictions, extracellular tortousity, and exchange," *Magn Reson Imaging*, vol. 16, pp. 1023–1032, 1998.

[8] T. Moritani, S. Ekholm, and P.-L. Westesson, *Diffusion-Weighted MR Imaging of the Brain*. Germany: Springer, 2005.

[9] J. J. Neil et al., "Normal brain in human newborns: Apparent diffusion coefficient and diffusion anisotropy measured by using diffusion tensor MR imaging," *Radiology*, vol. 209, pp. 57–66, 1998.

[10] T. Q. Li, Z. G. Chen, and T. Hindmarsh, "Diffusion-weighted MR imaging of acute cerebral ischemia," *Acta Radiol*, vol. 39, pp. 460–473, 1998.

[11] C. Baratti, A. S. Barnett, and C. Pierpaoli, "Comparative MR imaging study of brain maturation in kittens with T1, T2, and the trace of the diffusion tensor," *Radiology*, vol. 210, pp. 133–142, 1999.

[12] D. J. Werring, C. A. Clark, G. J. Barker, A. J. Thompson, and D. H. Miller, "Diffusion tensor imaging of lesions and normal-appearing white matter in multiple sclerosis," *Neurology*, vol. 52, pp. 1626–1632, 1999.

[13] A. L. Tievsky, T. Ptak, and J. Farkas, "Investigation of apparent diffusion coefficient and diffusion tensor anisotropy in acute and chronic multiple sclerosis lesions," *AJNR*, vol. 20, pp. 1491–1499, 1999.

[14] T. Iwasawa et al., "Diffusion-weighted imaging of the human optic nerve: A new approach to evaluate optic neuristis in multiple sclerosis," *Magn Reson Med*, vol. 38, pp. 484–491, 1997.

[15] M. A. Horsfield, H. B. Larsson, D. K. Jones, and A. Gass, "Diffusion magnetic resonance imaging in multiple sclerosis," *J Neuro Neurosurg Psychiatry*, vol. 64 (suppl 1), pp. S80–84, 1998.

[16] H. Ay et al., "Posterior leukoencephalopathy without severe hypertension: Utility of diffusion-weighted MRI," *Neurology*, vol. 51, pp. 1369–1376, 1998.

[17] H. Hanyu et al., "Increased water diffusion in cerebral white matter in Alzheimer's disease," *Gerontology*, vol. 43, pp. 343–351, 1997.

[18] H. Hanyu et al., "Diffusion-weighted MR imaging of the hippocampus and temporal white matter in Alzheimer's disease," *J Neurol Sci*, vol. 156, pp. 195–200, 1998.

[19] S. W. David, N. A. Dennis, N. G. Buchler, L. E. White, D. J. Madden, and R. Cabeza, "Assessing the effects of age on long white matter tracts using diffusion tensor tractography," *Neuroimaging*, vol. 46, pp. 530–541, 2009.

[20] D. L. Bihan, C. Poupon, A. Amadon, and F. Lethimonnier, "Artifacts and pitfalls in diffusion MRI," *J Magn Reson Imaging*, vol. 24, pp. 478–488, 2006.

[21] R. Bammer, "Basic principles of diffusion-weighted imaging," *Eur J Radiol*, vol. 45, pp. 169–184, 2003.

[22] P. J. Basser and D. K. Jones, "Diffusion-tensor MRI: Theory, experimental design and data analysis - A technical review," *NMR Biomed*, vol. 15, pp. 456–467, 2002.

[23] A. L. Alexander, K. M. Hasan, M. Lazar, J. S. Tsuruda, and D. L. Parker, "Analysis of partial volume effects in diffusion-tensor MRI," *Magn Reson Med*, vol. 45, pp. 770–780, 2001.

[24] D. S. Tuch, R. M. Weisskoff, J. W. Belliveau, and V. J. Wedeen, "High angular resolution diffusion imaging of the human brain," in *7th Annual Meeting of ISMRM*, Philadelphia, PA, 1999, p. 321.

[25] J. C. Falconer and P. A. Narayana, "Cerebral spinal fluid-suppressed high-resolution diffusion imaging of human brain," *Magn Reson Med*, vol. 37, pp. 119–123, 1997.

[26] J. G. Hirsch, M. Bock, M. Essig, and L. R. Schad, "Comparison of diffusion anisotropy measurements in combination with the FLAIR technique," *Magn Reson Med*, vol. 17, pp. 705–716, 1999.

[27] N. G. Zacharopoulos and P. A. Narayana, "Selective measurement of white matter and gray matter diffusion trace values in normal human brain," *Med Phys*, vol. 25, pp. 2237–2241, 1998.

[28] D. C. Karampinos, A. T. Van, W. C. Olivero, J. G. Georgiadis, and B. P. Sutton, "High-resolution diffusion tensor imaging of the human pons with a reduced-FOV multi-shot variable density spiral acquisition at 3 T," *Magn Reson Med*, vol. 62, pp. 1007–1016, 2009.

[29] H. Oouchi et al., "Diffusion anisotropy measurement of brain white matter is affected by voxel size: Underestimation occur in areas with crossing fibers," *Am J Neuroradiol*, vol. 28, pp. 1102–1106, 2007.

[30] L. M. Nagae-Poetscher, H. Jiang, S. Wakana, X. Golay, P. C. M. van Zijl, and S. Mori, "High-resolution diffusion tensor imaging of the brainstem at 3 T," *Am J Neuroradiol*, vol. 25, pp. 1325–1330, 2004.

[31] D. C. Karampinos, A. T. Van, B. D. Gonsalves, J. G. Georgiadis, and B. P. Sutton, "Resolving white matter structures of human hippocampus in vivo with high resolution DTI at 3 T," in *17th Annual Meeting of ISMRM*, Honolulu, HI, 2009, p. 3498.

[32] J. Finsterbusch, "High-resolution diffusion tensor imaging with inner field-of-view EPI," *J Magn Reson Imaging*, vol. 29, pp. 987–993, 2009.

[33] R. J. Ordidge, J. A. Helpern, Z. Quing, R. A. Knight, and V. Nagesh, "Correction of motional artifacts in diffusion-weighted MR images using navigator echoes," *Magn Reson Med*, vol. 12, pp. 455–460, 1994.

[34] K. Butts, A. D. Crespigny, J. M. Pauly, and M. E. Moseley, "Diffusion-weighted interleaved echo-planar imaging with a pair of orthogonal navigator echoes," *Magn Reson Med*, vol. 35, pp. 763–770, 1996.

[35] A. D. Crespigny, M. P. Marks, D. R. Enzmann, and M. E. Moseley, "Navigated diffusion imaging of normal and ischemic human brain," *Magn Reson Med*, vol. 33, pp. 720–728, 1995.

[36] A. W. Anderson and J. C. Gore, "Analysis and correction of motion artifacts in diffusion weighted imaging," *Magn Reson Med*, vol. 32, pp. 379–387, 1994.

[37] K. L. Miller and J. M. Pauly, "Nonlinear phase correction for navigated diffusion imaging," *Magn Reson Med*, vol. 47, pp. 343–353, 2003.

[38] J. G. Pipe, V. G. Farthing, and K. P. Forbes, "Multishot diffusion-weighted FSE using PROPELLER MRI," *Magn Reson Med*, vol. 47, pp. 42–52, 2004.

[39] C. Liu, R. Bammer, and M. E. Moseley, "High resolution multishot SENSE DTI using self-navigated interleaved spirals (SNAILS)," presented at the 13th Annual Meeting of ISMRM, Miami Beach, FL, May 2005.

[40] D. Atkinson, J. V. Hajnal, D. J. Larkman, P. G. Batchelor, and D. L. G. Hill, "Multiple coils for regridding multiple shot EPI diffusion data," presented at the 13th Annual Meeting of ISMRM, Miami Beach, FL, May 2005.

[41] C. Liu, R. Bammer, D.-H. Kim, and M. E. Moseley, "Self-navigated interleaved spiral (SNAILS): Application to high-resolution diffusion tensor imaging," *Magn Reson Med*, vol. 52, pp. 1388–1396, 2004.

[42] D. Atkinson, D. A. Porter, D. L. G. Hill, F. Calamante, and A. Connelly, "Sampling and reconstruction effects due to motion in diffusion-weighted interleaved echo planar imaging," *Magn Reson Med*, vol. 44, pp. 101–109, 2000.

[43] C. Liu, M. E. Moseley, and R. Bammer, "Simultaneous phase correction and SENSE reconstruction for navigated multi-shot DWI with non Cartesian k-space sampling," *Magn Reson Med*, vol. 54, pp. 1412–1422, 2005.

[44] D. Atkinson, S. Counsell, J. Hajanl, P. Batchelor, D. Hill, and D. Larkman, "Nonlinear phase correction of navigated multi-coil diffusion images," *Magn Reson Med*, vol. 56, pp. 1135–1139, 2006.

[45] T.-Q. Li, D.-H. Kim, and M. E. Moseley, "High-resolution diffusion-weighted imaging with interleaved variable-density spiral acquisition," *J Magn Reson Imaging*, vol. 21, pp. 468–475, 2005.

[46] S. Skare and J. L. R. Andersson, "On the effects of gating in diffusion imaging of the brain using single shot EPI," *Magn Reson Imaging*, vol. 19, pp. 1125–1128, 2001.

[47] A. T. Van, D. C. Karampinos, J. G. Georgiadis, and B. P. Sutton, "K-space and image-space combination for motion-induced phase-error correction in self-navigated multicoil multishot DWI," *IEEE Trans Med Imag*, vol. 28, pp. 1770–1780, 2009.

[48] P. Jezzard, A. S. Barnett, and C. Pierpaoli, "Characterization of and correction for eddy current artifacts in echo planar diffusion imaging," *Magn Reson Med*, vol. 39, pp. 801–812, 1998.

[49] N. G. Papadakis, K. M. Martin, J. D. Pickard, L. D. Hall, T. A. Carpenter, and C. L. Huang, "Gradient preemphasis calibration in diffusion-weighted echo-planar imaging," *Magn Reson Med*, vol. 44, pp. 616–624, 2000.

[50] T. G. Reese, O. Heid, R. M. Weisskoff, and V. J. Wedeen, "Reduction of eddy-current-induced distortion in diffusion MRI using a twice-refocused spin-echo," *Magn Reson Med*, vol. 49, pp. 177–182, 2003.

[51] G. Steidle and F. Schick, "Echoplanar diffusion tensor imaging of the lower leg musculature using eddy current nulled stimulated echo preparation," *Magn Reson Med*, vol. 55, pp. 541–548, 2006.

[52] A. L. Alexander, J. S. Tsuruda, and D. L. Parker, "Elimination of eddy current artifacts in diffusion-weighted echo-planar images: The use of bipolar gradients," *Magn Reson Med*, vol. 38, pp. 1016–1021, 1997.

[53] N. G. Papadakis, T. Smponias, J. Berwick, and J. E. Mayhew, "K-space correction of eddy-current-induced distortions in diffusion-weighted echo-planar imaging," *Magn Reson Med*, vol. 53, pp. 1103–1111, 2005.

[54] G. K. Rohde, A. S. Barnett, P. J. Basser, S. Marenco, and C. Pierpaoli, "Comprehensive approach for correction of motion and distortion in diffusion-weighted MRI," *Magn Reson Med*, vol. 51, pp. 103–114, 2004.

[55] M. A. Bernstein, K. F. King, and X. J. Zhoe, *Handbook of MRI Pulse Sequences*. Burlington, MA: Elsevier Academic Press, 2004.

[56] H. C. Torrey, "Bloch equations with diffusion terms," *Phys Rev*, vol. 104, pp. 563–565, 1956.

[57] D. L. Bihan, *Diffusion and Perfusion Magnetic Resonance Imaging: Applications to Functional MRI*. New York, NY: Raven Press, 1995.

[58] P. J. Basser, J. Mattiello, and D. L. Bihan, "MR diffusion tensor spectroscopy and imaging," *Biophys J*, vol. 66, pp. 259–267, 1994.

[59] P. J. Basser, S. Pajevic, C. Pierpaoli, J. Duda, and A. Aldroubi, "In vivo fiber tractography using DT-MRI data," *Magn Reson Med*, vol. 44, pp. 625–632, 2000.

[60] M. Kim, I. Ronen, K. Ugurbil, and D.-S. Kim, "Spatial resolution dependence on DTI tractography in human occipito-callosal region," *Neuroimage*, vol. 32, pp. 1243–1249, 2006.

[61] S. Fujiwara, M. Sasaki, Y. Kanbara, T. Inoue, R. Hirooka, and A. Ogawa, "Feasibility of 1.6-mm isotropic voxel diffusion tensor tractographi in depicting limbic fibers," *Neuroradiology*, vol. 50, pp. 131–136, 2008.

[62] S. Mori and P. C. M. van Zijl, "Fiber tracking: Principles and strategy-A technical review," *NMR Biomed*, vol. 15, pp. 468–480, 2002.

[63] E. U. Saritas, C. H. Cunningham, J. H. Lee, E. T. Han, and D. G. Nishimura, "DWI of the spinal cord with reduced FOV single-shot EPI," *Magn Reson Med*, vol. 60, pp. 468–473, 2008.

[64] J. E. Sarlls and C. Pierpaoli, "High-resolution diffusion tensor imaging at 3 T with radial FSE," in *16th Annual Meeting of ISMRM*, Toronto, Canada, 2008, p. 758.

[65] J. Zhang, C. Liu, and M. Moseley, "3D self-navigated interleaved spiral (3D-SNAILS) for DWI," in *15th Annual Meeting of ISMRM*, Berlin, Germany, 2007, p. 9.

[66] A. T. Van, D. C. Karampinos, and B. P. Sutton, "High resolution 3d multi-slab multi-shot spin echo diffusion-weighted imaging," in *18th Annual Meeting of ISMRM*, Stockholm, Sweden, 2010, p. 1618.

[67] M. Engstrom, A. Nordell, M. Martensson, B. Nordell, R. Bammer, and S. Skare, "Isotropic resolution in diffusion weighted imaging using 3d multi-slab, multi-echo echo planar imaging," in *18th Annual Meeting of ISMRM*, Stockholm, Sweden, 2010, p. 1619.

[68] Y. Jung et al., "3D diffusion tensor MRI with isotropic resolution using a steady-state radial acquisition," *J Magn Reson Imaging*, vol. 29, pp. 1175–1184, 2009.

[69] E. K. Jeong, S. E. Kim, and D. L. Parker, "High-resolution diffusion-weighted 3D MRI, using diffusion-weighted driven-equilibrium (DW-DE) and multishot segmented 3D-SSFP without navigator echoes," *Magn Reson Med*, vol. 50, pp. 821–829, 2003.

[70] J. A. McNab, S. Jbabdi, S. C. Deoni, G. Douaud, T. E. Behrens, and K. L. Miller, "High resolution diffusion-weighted imaging in fixed human brain using diffusion-weighted steady state free precession," *Neuroimage*, vol. 46, pp. 775–785, 2009.

[71] L. R. Frank, Y. Jung, S. Inati, J. M. Tyszka, and E. C. Wong, "High efficiency, low distortion 3D diffusion tensor imaging with variable density spiral fast spin echoes (3D DW VDS RARE)," *Neuroimage*, vol. 49, pp. 1510–1523, 2010.

[72] D. L. Bihan, "Intravoxel incoherent motion imaging using steady-state free precession," *Magn Reson Med*, vol. 7, pp. 346–351, 1988.

[73] R. B. Buxton, "The diffusion sensitivity of fast steady-state free precession imaging," *Magn Reson Med*, vol. 29, pp. 235–243, 1993.

[74] C. A. M. Wheeler-Kingshott et al., "ADC mapping of the human optic nerve: Increased resolution, coverage and reliability with CSF-suppressed ZOOM-EPI," *Magn Reson Med*, vol. 47, pp. 24–31, 2002.

[75] B. J. Wilm, J. Svensson, A. Henning, K. P. Pruessmann, P. Boesiger, and S. S. Kollias, "Reduced field-of-view MRI using outer volume suppression for spinal cord diffusion imaging," *Magn Reson Med*, vol. 57, pp. 625–630, 2007.

[76] H. Goldstein, *Classical Mechanics*. Reading, PA: Addison-Wesley, 1980.

[77] K. Sekihara, M. Kuroda, and H. Kohno, "Image restoration from non-uniform magnetic field influence for direct fourier NMR imaging," *Phys Med Biol*, vol. 29, pp. 15–24, 1984.

[78] A. Maeda, K. Sano, and T. Yokoyama, "Reconstruction by weighted correlation for MRI with time varying gradient," *IEEE Trans Med Imag*, vol. 7, pp. 26–31, 1988.

[79] D. C. Noll, C. H. Meyer, J. M. Pauly, D. G. Nishimura, and A. Macovski, "A homogeneity correction method for magnetic resonance imaging with time-varying gradients," *IEEE Trans Med Imag*, vol. 10, pp. 629–637, 1991.

[80] D. C. Noll, J. M. Pauly, C. H. Meyer, D. G. Nishimura, and A. Macovski, "Deblurring for non-2D Fourier transform magnetic resonance imaging," *Magn Reson Med*, vol. 25, pp. 319–333, 1992.

[81] B. P. Sutton, D. C. Noll, and J. A. Fessler, "Fast, iterative image reconstruction for MRI in the presence of field inhomogeneities," *IEEE Trans Med Imag*, vol. 22, pp. 178–188, 2003.

[82] J. Finsterbusch, "Eddy-current compensated diffusion weighted with a single refocusing RF pulse," *Magn Reson Med*, vol. 61, pp. 748–754, 2009.

[83] J. Finsterbusch, "Double-spin-echo diffusion weighting with a modified eddy current adjustment," *Magn Reson Imaging*, vol. 28, pp. 434–440, 2010.

[84] R. Bammer et al., "Diffusion tensor imaging using single-shot SENSE-EPI," *Magn Reson Med*, vol. 48, pp. 128–136, 2002.

[85] K. P. Pruessman, M. Weiger, M. B. Scheidegger, and P. Boesiger, "SENSE: Sensitivity encoding for fast MRI," *Magn Reson Med*, vol. 42, pp. 952–962, 1999.

[86] D.-H. Kim, E. Adalsteinsson, and D. M. Spielman, "Simple analytic variable density spiral design," *Magn Reson Med*, vol. 50, pp. 214–219, 2003.

[87] S. Brockstedt et al., "Triggering in quantitative diffusion imaging with single-shot EPI," *Acta Radiol*, vol. 40, pp. 263–269, 1999.

[88] S. Reeder et al., "Practical approaches to the evaluation of signal-to-noise ratio performance with parallel imaging: Application with cardiac imaging and a 32-channel cardiac coil," *Magn Reson Med*, vol. 54, pp. 748–754, 2005.

[89] S. M. Smith et al., "Advances in functional and structural MR image analysis and implementation as FSL," *NeuroImage*, vol. 23, pp. 208–219, 2004.

[90] T. E. J. Behrens et al., "Characterization and propagation of uncertainty in diffusion-weighted MR imaging," *Magn Reson Med*, vol. 50, pp. 1077–1088, 2003.

[91] T. E. J. Behrens et al., "Non-invasive mapping of connections between human thalamus and cortex using diffusion imaging," *Nature Neuroscience*, vol. 6, pp. 750–757, 2003.

[92] T. E. J. Behrens, H. Johansen-Berg, S. Jbabdi, M. F. S. Rushworth, and M. W. Woolrich, "Probabilistic diffusion tractography with multiple fibre orientations. What can we gain?" *NeuroImage*, vol. 23, pp. 144–155, 2007.

[93] J. A. Fessler and B. P. Sutton, "Nonuniform fast Fourier transform using min-max interpolation," *IEEE Trans Signal Process*, vol. 51, pp. 560–574, 2003.

[94] J. A. Fessler, "Penalized weighted least-squares image reconstruction for positron emission tomography," *IEEE Trans Med Imag*, vol. 13, pp. 290–300, 1994.

[95] G. H. Glover, "Simple analytic spiral k-space algorithm," *Magn Reson Med*, vol. 42, pp. 412–415, 1999.

[96] G. J. Stanisz et al., "T1, t2 relaxation and magnetization transfer in tissue at 3T," *Magn Reson Med*, vol. 54, pp. 507–512, 2005.

[97] K. Liu, Y. Xu, and M. Loncar, "Reduced slab boundary artifact in multi-slab 3D fast spin-echo imaging," *Magn Reson Med*, vol. 44, pp. 269–276, 2000.

[98] L. L. Scharf and L. T. McWhorter, "Geometry of the Cramér-Rao bound," in *Proc. IEEE Sixth SP Workshop on Statistical Signal and Array Processing*, Victoria, BC, Canada, 1992, pp. 5–8.

[99] D. Hernando, J. P. Haldar, B. P. Sutton, J. Ma, P. Kellman, and Z.-P. Liang, "Joint estimation of water/fat images and field inhomogeneity map," *Magn Reson Med*, vol. 59, pp. 571–580, 2008.

[100] R. G. Nunes, P. Jezzard, and S. Clare, "Investigations on the efficiency of cardiac-gated methods for the acquisition of diffusion-weighted images," *J Magn Reson*, vol. 177, pp. 102–110, 2005.

[101] R. M. Henkelman, "Measurement of signal intensities in the presence of noise in MR images," *Med Phys*, vol. 12, pp. 232–233, 1985.

[102] W. Edelstein, P. Bottomley, and L. Pfeifer, "A signal-to-noise calibration procedure for NMR imaging system," *Med Phys*, vol. 11, pp. 180–185, 1984.

[103] X. Golay, H. Jiang, P. C. M. van Zijl, and S. Mori, "High-resolution isotropic 3D diffusion tensor imaging of the human brain," *Magn Reson Med*, vol. 47, pp. 837–843, 2002.

[104] E. K. Jeong, S. E. Kim, E. G. Kholmovski, and D. L. Parker, "High-resolution DTI of a localized volume using 3D single-shot diffusion-weighted stimulated echo-planar imaging (3D ss-DWSTEPI)," *Magn Reson Med*, vol. 56, pp. 1173–1181, 2006.

[105] J. Zhang, C. Liu, and M. Moseley, "Steady-state free precession (SSFP) diffusion imaging using 3D rotating spirals (3DRS)," in *17th Annual Meeting of ISMRM*, Honolulu, HI, 2009, p. 168.

[106] E. Aboussouan and J. Pipe, "3D PROPELLER-based diffusion weighted imaging," in *17th Annual Meeting of ISMRM*, Honolulu, HI, 2009, p. 2632.

[107] E. Aboussouan and J. Pipe, "3D PROPELLER-based diffusion weighted imaging with improved robustness to motion," in *18th Annual Meeting of ISMRM*, Stockholm, Sweden, 2010, p. 1615.

[108] B. P. Sutton and A. T. Van, "Multicontrast 3D structural imaging to improve automatic brain extraction and segmentation," in *18th Annual Meeting of ISMRM*, Stockholm, Sweden, 2010, p. 2332.

[109] E. R. Kandel, J. H. Schwartz, and T. M. Jessell, *Principles of Neural Science*. New York, NY: McGraw-Hill, 2000.

[110] B. P. Thomas et al., "High-resolution 7 T MRI of the human hippocampus in vivo," *J Magn Reson Imaging*, vol. 28, pp. 1266–1272, 2008.

[111] P. Kalus et al., "Examining the gateway to the limbic system with diffusion tensor imaging: The perforant pathway in dementia," *NeuroImage*, vol. 30, pp. 713–720, 2006.

[112] T. R. Stoub, L. de Toledo-Morrell, G. T. Stebbins, S. Leurgans, D. A. Bennett, and R. C. Shah, "Hippocampal disconnection contributes to memory dysfunction in individuals at risk for Alzheimer's disease," *Proceedings of the National Academy of Sciences of the United States of America*, vol. 103, pp. 10 041–10 045, 2006.

[113] A. Bakker, C. B. Kirwan, M. Miller, and C. E. Stark, "Pattern separation in the human hippocampal CA3 and dentate gyrus," *Science*, vol. 319, pp. 1640–1642, 2008.

[114] D. R. Thal et al., "Alzheimer-related taupathology in the perforant path target zone and in the hippocampal stratum oriens and radiatum correlates with onset and degree of dementia," *Exp Neurol*, vol. 163, pp. 98–110, 2000.

[115] H. Braak, I. Alafuzoff, T. Arzberger, H. Kretzschmar, and K. D. Tredici, "Staging of Alzheimer disease-associated neurofibrillary pathology using paraffin sections and immunocytochemistry," *Acta Neuropathol*, vol. 112, pp. 389–404, 2006.

[116] P. Andersen, R. Morris, D. Amaral, T. Bliss, and J. O'Keefe, *The Hippocampus Book*. New York, NY: Oxford University Press, 2007.

[117] T. M. Shepherd, E. Ozarslan, A. T. Yachnis, M. A. King, and S. J. Blackband, "Diffusion tensor microscopy indicates the cytoarchitectural basis for diffusion anisotropy in the human hippocampus," *AJNR*, vol. 28, pp. 958–964, 2007.

[118] B. T. Hyman, G. W. V. Hoesen, A. R. Damasio, and C. L. Barnes, "Alzheimer's disease: Cell-specific pathology isolates the hippocampal formation," *Science*, vol. 225, pp. 1168–1170, 1984.

[119] H. Braak and E. Braak, "On areas of transition between allocortex and temporal isocortex in the human brain. Normal morphology and lamina-specific pathology in Alzheimer's disease," *Acta Neuropathol*, vol. 68, pp. 325–332, 1985.

[120] M. P. Witter, F. G. Wouterlood, P. A. Naber, and T. van Haeften, "Anatomical organization of the parahippocampal-hippocampal network," *Ann NY Acad Sci*, vol. 911, pp. 1–24, 2000.

[121] D. A. Porter, D. Atkinson, R. Scott, and C. A. Clark, "High-resolution diffusion tensor imaging reveals sub-structure within human hippocampus in vivo," in *16th Annual Meeting of ISMRM*, Toronto, Canada, 2008, p. 3362.

[122] S. Meiboom and D. Gill, "Modified spin-echo method for measuring nuclear relaxation time," *Rev Sci Instrum*, vol. 29, pp. 688–691, 1958.

[123] P. L. Roux, "Non-CPMG fast spin echo with full signal," *J Magn Reson*, vol. 155, pp. 278–292, 2002.

[124] J. E. Sarlls and C. Pierpaoli, "Diffusion-weighted radial fast spin-echo for high-resolution diffusion tensor imaging at 3 t," *Magn Reson Med*, vol. 60, pp. 270–276, 2008.

[125] G. S. Pell, R. S. Briellmann, A. B. Waites, D. F. Abbott, D. P. Lewis, and G. D. Jackson, "Optimized clinical T2 relaxometry with a standard CPMG sequence," *J Magn Reson Imaging*, vol. 23, pp. 248–252, 2006.